



Title	A study on the relationship between synoptic field and precipitation/runoff with dynamical downscaling
Author(s)	玉置, 雄大
Citation	北海道大学. 博士(理学) 甲第13570号
Issue Date	2019-03-25
DOI	10.14943/doctoral.k13570
Doc URL	http://hdl.handle.net/2115/77048
Type	theses (doctoral)
File Information	Yuta_Tamaki.pdf



[Instructions for use](#)

Doctoral Dissertation

**A study on the relationship between synoptic field and
precipitation/runoff with dynamical downscaling**

力学的ダウンスケーリングを用いた総観場と降水・流出の
関係に関する研究

Yuta Tamaki

玉置雄大

Division of Earth and Planetary Dynamics, Department of Natural History Sciences,

Graduate School of Science, Hokkaido University

北海道大学大学院理学院自然史科学専攻

地球惑星ダイナミクス講座

2019 年 3 月

Abstract

We applied the sampling downscaling (SmDS), one of the efficient dynamical downscaling (DDS) method, to summertime precipitation over Hokkaido as a case study and estimated the error in SmDS based on a statistical theory. And we quantitatively evaluate the rainfall duration bias and the response of runoff and water-depth to the rainfall duration bias.

The high spatiotemporal resolution data produced by the DDS are mainly used in climate change adaptation researches. In particular, rainfall amount and rainfall duration are important factors for estimating river runoff. DDS has generally two problems; one is that the DDS needs much computational cost for the high resolution simulation, the other is that the DDS has rainfall bias, which are resulted from the unrealistic topography and insufficient physical parameterizations, including cloud physics, convective parameterization in regional climate model (RCM) and general circulation model (GCM). Some previous studies have developed the economical DDS method in computational cost. Thus, the bias correction of frequency of rainfall amount, quantile mapping, has been developed. However there are a few case studies for application of the economical DDS and its estimation error has not been theoretically evaluated. On the other hand the bias correction of rainfall duration bias still has not been developed and furthermore no study has not evaluated the rainfall duration bias.

The sampling downscaling (SmDS) in which a regional atmospheric model is integrated for sampled periods was performed for summertime Hokkaido. Selected are top two and bottom two years of the general circulation model projection onto the first mode of a singular value decomposition analysis, and for this mode, heavy precipitation in southern Hokkaido is correlated with the moisture flux convergence in the synoptic

field. The SmDS result integrated for the four years successfully reproduces the dynamical downscaling result for 30 years, in terms of climatological precipitation and the 99-percentile value of daily precipitation. This indicates that SmDS can be applied to the environment where local precipitation is mostly controlled by synoptic climate patterns. A further statistical consideration in this study supports the notion. It is also demonstrated that SmDS selects a group of years where extreme events likely occur another group of years where they rarely occur.

The DDS was conducted over Japan by using a regional atmospheric model with reanalysis data to investigate the rainfall duration bias over Kyushu, Japan, in July and August from 2006 to 2015. The model results showed that DDS had a positive rainfall duration bias over Kyushu and a dry bias over almost all of Kyushu, results which were emphasized for extreme rainfall events. Investigated was the rainfall duration bias for heavy rainfall days, accompanied by synoptic-scale forcing, in which daily precipitation exceeded 30 mm day^{-1} and covered over 20% of the Kyushu area. Heavy rainfall days were sampled from observed rainfall data based on rain-gauge and radar observations. A set of daily climatic variables of horizontal wind and equivalent potential temperature at 850 hPa and sea-level pressure, around southwestern Japan, corresponding to the sampled dates, were selected to conduct a self-organizing map (SOM) and *K*-means method. The SOM and *K*-means method objectively classified three synoptic patterns related to heavy rainfall over Kyushu: strong monsoon, weak monsoon, and typhoon patterns. Rainfall duration had a positive bias in western Kyushu for the strong monsoon pattern and a positive bias in southern and east-coast Kyushu for the typhoon pattern, whereas there was little rainfall duration bias in the weak monsoon pattern. The bias for the typhoon pattern was related to rainfall events with a strong rainfall peak. The results imply that

bias correction for rainfall duration would be required for accurately estimating river runoff in a catchment area besides the precipitation amount.

Motivated from the problem of a rainfall duration bias typically in dynamical downscaling, its possible effect of the rainfall duration bias to hydrology was evaluated for heavy rainfall events over Kyushu, Japan, in summer. For the typical heavy-rainfall periods, a tank model for several target rivers ran to analyze runoff and water-depth sensitivity to hyetograph, by artificially extending the rainfall duration to 8 hours or 16 hours with keeping the total rainfall amount. The results showed that a spike peak of runoff was suppressed by a prolonged weak rainfall as typically found in downscaling outputs. The rising timings of runoff and water depth in the tank model became earlier. The decrease in the contribution of surface and subsurface runoff was pronounced in the heavy rainfall events accompanied with a persistent Baiu rainband. Our results suggest that the rainfall duration bias of DDS is a non-negligible factor for predicting river runoff and flood risk in climate change adaptation.

日本語要旨

本研究では力学的ダウンスケーリング(DDS)の計算効率化手法の一つであるサンプリングダウンスケーリング(SmDS)を夏季北海道に事例に適用し、SmDSの誤差を統計理論を用いて評価し、さらに降水継続時間バイアスの定量化と降水継続時間のバイアスに対する流出、水位応答の定量的評価を行った。

降水データを用いた気候変動適応研究には時空間解像度の細かい DDS の出力が主に用いられる。特に、降水量と降水継続時間は河川流出予測にとって重要な要素である。DDS には高解像度化するほど計算コストが膨大となること、そして全球モデル、領域モデルの物理的パラメタリゼーションや、地形に由来するモデルバイアスを含むという二つの問題がある。先行研究では DDS の計算コストを効率化する手法が開発されており、降水バイアスの問題に対しては降水量の頻度バイアスを補正する手法、クオントイルマッピングが開発されている。しかしながら、効率化手法の適用事例は少なく、理論的に誤差を評価した研究はない。一方で降水バイアスの問題については降水継続時間のバイアスは評価されてこなかった。

サンプルされた年のみを領域モデルで積分するサンプリングダウンスケーリング(SmDS)を夏季北海道に適用した。全球モデル出力を北海道南側での強い降水が総観場での水蒸気フラックス収束と相関を持つ第一特異モードに射影し、その射影の上位 2 年と下位 2 年を選んだ。4 年積分した SmDS の結果は降水量の気候値および日降水量の 99 パーセンタイル値において 30 年積分した力学的ダウンスケーリングの結果をほぼ正確に再現した。これは、局所的な降水が総観規模の気象状況に支配される状況では SmDS が適用できうることを示唆している。本研究ではさらにこのような考えを裏付ける統計的考察を行った。また、SmDS は極端降水が多い年と少ない年を選択していることも明らかとなった。

2006-2015 年の 7,8 月において九州における降水継続時間のバイアスを評価するために、領域気候モデルを用いて再解析データを境界条件に DDS を行った。その結果 DDS は九州全体で正の継続時間バイアスを持ち、九州のほとんどの領域で降水量のバイアスが過小であった。このバイアスの特徴は極端降水イベントにおいてさらに顕著であった。さらに、九州陸域において日降水量 $\geq 30\text{mm day}^{-1}$ かつ被覆率が 20%以上を満たす日の、総観規模の強制に伴う強降水日において降水継続時間のバイアスを評価した。強降水日は雨量計とレーダー観測に基づく観測データから抽出した。自己組織化マップ(SOM)と K -平均法を実行するために、4つの気象場の変数として 850hP 水平風、相当温位、海面校正気圧を選択した。SOM と K -平均法は強いモンスーン型、弱いモンスーン型、台風型の3つの大雨に関連する気象場を客観的に分類した。降水継続時間の正のバイアスは強いモンスーン型では九州西部に、台風型では九州東部に見られた。一方で弱いモンスーン時には降水継続時間のバイアスは小さかった。台風型での降水継続時間のバイアスは大きな降水ピークを持つ降水イベントに関連していた。この結果は河川流出の正確な推定のためには、降水量のバイアス補正に加えて、降水継続時間のバイアス補正も必要であることを示唆している。

DDS の継続時間バイアスの問題意識から、夏季九州において降水継続時間バイアスに対する水文学的応答を評価した。典型的な豪雨事例を対象に総降水量を保存し、降水継続時間を 8 時間、16 時間引き伸ばしたハイエトグラフに対する流出と水位の感度をいくつかの河川を対象にタンクモデルを用いて評価した。その結果、DDS で典型的に見られた降水量の小さい長雨によって流出の鋭いピークは抑制された。また、流出と水位の上昇のタイミングは早まる結果となった。表面流とサブ表面流出の減少は梅雨前線に伴う強降雨イベントで顕著であった。本研究の結果は、河川流出、洪水リスクに関する気候変動適応研究を実施する上

で，降水継続時間バイアスが無視できない要素であることを示唆する．

Table of contents

Abstract	iii
日本語要旨	vi
Chapter 1. General Introduction	1
Chapter 2. Sampling downscaling in summertime precipitation over Hokkaido	4
2.1. Introduction	4
2.2. Data and models	6
<i>a. Observed data</i>	6
2.3. General concept of SmDS	8
<i>a. Procedure</i>	8
<i>b. Error estimation theory</i>	8
2.4. Results	13
<i>a. SmDS setup</i>	13
<i>b. Comparison with conventional DDS</i>	14
<i>c. Interpretation of results</i>	15
2.5. Conclusions and discussion	16
Chapter 3. Heavy rainfall duration bias in dynamical downscaling and its related synoptic patterns in summertime Asian monsoon	30
3.1. Introduction	30
3.2. Data and method	33
<i>a. Observations</i>	33
<i>b. RAM experiments</i>	34
<i>c. Classification of synoptic patterns related to heavy rainfall</i>	35
<i>d. Definition of a rainfall event</i>	36
3.3. Results	37
<i>a. RAM simulations</i>	37
<i>b. Synoptic patterns related to heavy rainfall days</i>	38
<i>c. Rainfall duration bias related to heavy rainfall days</i>	40
3.4. Discussion	41
<i>a. Transition cases</i>	41
<i>b. Sensitivity tests</i>	42
<i>c. Model biases</i>	44
3.5. Conclusions	46
Chapter 4. Possible hydrological effect of rainfall duration bias in dynamical downscaling ...	71
4.1 Introduction	71

4.2 Data and method	73
4.3 Results	74
<i>a. Event with the Baiu rainband and hydrology at Shimouke dam</i>	74
<i>b. Event with the typhoon approach and hydrology at Urita dam</i>	76
4.4 Discussion	77
4.5 Conclusions	78
Chapter 5. General summary	92
Acknowledgements	93
References	94

Chapter 1. General Introduction

Heavy rainfall causes natural disasters, including flooding and inundation, landslides, erosion, and hightides. Many observation studies have reported recent increase in heavy rainfall (cf. DeGaetano 2009; Bartholy and Pngracz 2007; Fujibe et al. 2006). It is anticipated that a wetter climate caused by global warming would result in a greater chance of heavy rainfall (Donat et al. 2016). Therefore, a series of adaptation policies should be compiled to prepare for possible hazards due to more frequent heavy rainfall, and thus a high-resolution dataset for the precipitation is highly required. Dynamical downscaling (DDS; Giorgi 1990) has been a widely used to fill the scale gap between the climate model projection and social demand.

DDS provides physically consistent data, but the DDS results strongly depend on the choice of regional climate model (RCM) and lateral boundary condition. Therefore, the multi-GCMs by multi-RCMs experiment is needed to identify model uncertainty in the regional climatic field. This ensemble experiment, however, needs much computational cost. Recently, the sampling downscaling (SmDS) method proposed by Kuno and Inatsu (2015) was proposed to conduct DDS for a few typical years that the synoptic pattern controls local precipitation. The SmDS method is one of the techniques with mixing DDS with statistical downscaling (SDS), extending previous works (Frey-Buness et al. 1995; Pinto et al. 2014; Yamada et al. 2014). However the SmDS is still applied to only one case, thus it is not fully explored that whether the SmDS can be applied to another season or region and how effectively the SmDS reduces the computational costs for DDS. Moreover, in order to demonstrate the relevance of such kind of DDS-SDS methods, we need a statistical consideration as well as a pile of case

studies with DDS-SDS mixture methods.

DDS also has rainfall bias that results from the unrealistic topography and physical parameterizations, including cloud physics, convective parameterization in RCM and GCM as the lateral boundary condition (Ehret et al. 2012; Wang et al. 2004), of which bias influences the runoff prediction. However, the traditional bias correction for rainfall such as frequency bias correction of rainfall amount (quantile mapping; Piani et al. 2010) and bias correction of mean consecutive rainfall days (Nyeko-Ogiramoi et al. 2012) does not correct the spatio-temporal characteristics of rainfall that is important factor to determine the runoff (Kim and Kim 2018; Ogden and Julien 1993). In addition, no one has yet stated how the rainfall from DDS contains the rainfall duration bias.

There are three purposes for this thesis. The first purpose is to apply SmDS to summertime precipitation over Hokkaido as another case study and to estimate the error in SmDS based on statistical theory. We compare SmDS for four years with DDS with 30 years in terms of the daily-mean precipitation, the standard deviation, and the 99-percentile value of daily precipitation. The second purpose is to evaluate the rainfall duration bias of DDS forced with reanalysis data in summertime over Kyushu. Li et al. (2018) proposed a bias correction method of rainfall based on quantile mapping according to synoptic patterns related to heavy rainfall. Their studies imply that rainfall bias is related to synoptic patterns and it is natural that rainfall duration bias is also related to its synoptic patterns. We apply the self-organizing map (SOM) to detect the typical synoptic patterns related to heavy rainfall days in Kyushu and link the patterns with rainfall duration biases. The third purpose is to evaluate the sensitivity of runoff to rainfall duration in typical synoptic patterns related to heavy rainfall with tank-model (Sugawara 1972).

The rest of this thesis is organized as follows. Chapter 2 describes the application of SmDS to summertime precipitation over Hokkaido and the error estimation theory based on Tamaki et al. (2016). In Chapter 3, the heavy rainfall duration bias is investigated based on Tamaki et al. (2018). In Chapter 4, the runoff response to the rainfall duration is investigated with tank model simulation. Chapter 5 describes the general summary.

Chapter 2. Sampling downscaling in summertime precipitation over Hokkaido

2.1. Introduction

The dynamical downscaling (DDS) is a widely-used technique to estimate high-resolution data that are physically consistent with prescribed low-resolution data such as reanalysis data and general circulation model (GCM) outputs, by using a regional atmospheric model (RAM) for a limited domain. In the DDS, a RAM is integrated typically with $O(10\text{ km})$ horizontal resolution nested into a GCM with $O(100\text{ km})$ horizontal resolution and can considerably resolve the geographical features such as mountains and coastlines. Hence, by using the RAM, one can realistically simulate local phenomena such as orographic rainfall (Frei et al. 2003) and snow-albedo feedback (Leung et al. 2004), and estimate a regional climate change including a land effect characterized locally (Sato and Kimura 2005). However, a RAM integration in DDS mostly has much computational costs in order to satisfy the Courant–Friedrichs–Lewy condition. Moreover, if the DDS result largely depends on the GCM imposed as the RAM boundary condition (Plummer et al. 2006; Fowler et al. 2007; Piani et al. 2010), we would spend still more costs for multi-GCM experiments in order to evaluate uncertainty in a local climate change.

Conversely, the statistical downscaling (SDS) is another downscaling method, based on an observed statistical relationship between a regional variable and a global circulation pattern (*e.g.*, von Storch 1995; Hay et al. 2002; Imada et al. 2012). The SDS may evaluate a regional climate depending on the observation density, and it takes a little

computations. However, because the empirical relationship in the present climate is not always applied to the future climate, the reliability of SDS results strongly depends on the stability of statistics (Wilby et al. 2004).

Recently, Kuno and Inatsu (2014) proposed the sampling downscaling (SmDS), in which the DDS is performed for a few years based on the statistical relation between a synoptic climate pattern and a local precipitation amount. On the basis of a robust observed linkage between winter Asian monsoon and regional snowfall in Hokkaido, they showed that SmDS actually provided a similar result to conventional DDS. The SmDS is one of the techniques with mixing DDS with SDS, extending previous works; Frey–Buness et al. (1995) obtained a regional climate feature based on DDS for a few large-scale weather types that were *a priori* classified. Pinto et al. (2014) attempted to select the representative days for DDS based on the probability density function (PDF) of 2 m air temperatures; Yamada et al. (2014) established a statistical equation which approximately follows the Clausius–Clapeyron relationship equation between 99-percentile value of sub-hourly precipitation and near surface temperature. Using the near surface temperature given by DDS, they successfully estimated the 99-percentile value of sub-hourly precipitation in Sapporo for future climate. However, in order to demonstrate the relevance of the DDS–SDS mixture, we need statistical consideration as well as a pile of case studies in which a particular DDS–SDS mixture method is applied to different domains and seasons. For example, summertime rainfall in Hokkaido is possibly related to local-scale phenomena such as topographic rainfall, cumulus cloud convection, and small-scale rainband. Hence, a study extending Kuno and Inatsu (2014) to boreal summer deserves our attention to ascertain the applicability of SmDS.

The purpose of this study is (1) to apply SmDS to summertime precipitation over

Hokkaido as another case study from Kuno and Inatsu (2014) and (2) to estimate the error in SmDS with statistical consideration. For the first purpose, we compare SmDS for four years with DDS for 30 years (hereafter full DDS) in terms of the daily-mean precipitation, the standard deviation of June–July–August (JJA) mean precipitation, and the 99-percentile value of daily precipitation. The 99-percentile value of daily precipitation is calculated during the JJA days for all years used. For the second purpose, we theoretically consider the error of the mean and the 99-percentile value estimated in SmDS.

This paper is organized as follows. Datasets and models we used are described in Section 2.2. A general overview of SmDS with error estimation consideration is stated in Section 2.3. In Section 2.4, the result of SmDS for four selected years is compared with the result of DDS for 30 years, in terms of the climatological precipitation and the 99-percentile value of daily precipitation in Hokkaido in summer. Section 2.5 summarizes this paper.

2.2. Data and models

a. Observed data

We used a set of observed datasets for SmDS. Precipitation dataset is APHRO_JP V1207 (Yatagai et al. 2012). The horizontal resolution is $0.05^\circ \times 0.05^\circ$. We used a 6-hourly reanalysis dataset, JRA-25/JCDAS (Onogi et al. 2007), for the moisture flux convergence vertically integrated from surface pressure to 100 hPa. The horizontal resolution of the reanalysis data is $1.25^\circ \times 1.25^\circ$. The analysis period is JJAs from 1981 to 2010.

b. GCMs

We performed DDS experiments with multiple atmosphere-ocean GCMs in Coupled Model Inter-comparison Project phase 3 (CMIP3) as the boundary condition. GCMs we used are the Model for Interdisciplinary Research on Climate version 3.2 (hereafter MIROC) developed by the University of Tokyo (Hasumi and Emori 2004); the fifth generation atmospheric GCM in Max Plank Institute for meteorology (hereafter MPI; Roeckner et al. 2003); and Community Climate System Model version 3 in the National Center for Atmospheric Research (hereafter NCAR; Collins et al. 2006). These three GCMs can reproduce the present climate over Japan in summer (Inatsu et al. 2015). Following Kuno and Inatsu (2014), we selected the last decade of the 20th-century experiment called 20C3M in CMIP3 as the current climate.

c. RAM

The RAM that we used is the Japan Meteorological Agency/Meteorological Research Institute non-hydrostatic model (JMA/MRI-NHM) [see Saito et al (2006) for more details]. The model domain covers 132°E–152°E and 38°N–50°N (Fig. 2.1) of which center is Hokkaido Island (Fig. 2.2). The horizontal grid space is set to 10 km. The RAM was integrated for 10 years with each GCM as the boundary condition of 1991–2000 for MIROC and MPI, and 1990–1999 for NCAR and then we obtained 30 year output in total for the current climate condition. The sea surface temperatures provided by the ocean component of each GCM were prescribed as the ocean-surface boundary condition of the RAM.

2.3. General concept of SmDS

a. Procedure

We will give the procedure of SmDS in a nutshell (Fig. 2.3). See Kuno and Inatsu (2014) for more details. First, we took the singular value decomposition (SVD) analysis between moisture flux convergence around Hokkaido (120°E–160°E by 30°N–60°N) and precipitation over Hokkaido (139°E–146°E by 41°N–46°N; Fig. 2.1) based on JJA-mean data from 1981 to 2010. Since the SVD analysis provides the highly-covariate spatial patterns between the two, we obtained a heterogeneous spatial pattern for the first mode of moisture flux convergence around Japan referred to as $\mathbf{g}_1(\mathbf{x})$, where \mathbf{x} is the position vector.

Next, we projected GCM's moisture flux convergence anomaly, $\tilde{\mathbf{G}}(\mathbf{x}, \tilde{t})$, onto the first SVD mode, $\mathbf{g}_1(\mathbf{x})$, where \tilde{t} denotes a sequential union of the GCM periods. The projected time-series $s(\tilde{t})$ was used as an index to select years for SmDS. Finally, we conducted the DDS for years with top two and bottom two of $s(\tilde{t})$. In this paper, as has already mentioned above, we conducted the DDS for 30 years in total and then the statistics for all years were compared with the statistics for selected years.

b. Error estimation theory

We here consider the error in SmDS estimates of statistical precipitation amount. First, though the sample number is practically finite, we regard it as population Ω with N samples as

$$\Omega = \bigcup_{k=1}^N \omega_k, \quad (1)$$

where a sample ω_j is the j -th year with the amount of daily data being n as

$$\omega_j = \{p_{j,1}, p_{j,2}, \dots, p_{j,n}\}, \quad (2)$$

where n is the number of days in a single sample. Regional variable P and global variable Q are set as probabilistic variables on the population Ω . A set of the sample mean of P expressed as

$$\Sigma_P = \{\bar{P}_1, \bar{P}_2, \dots, \bar{P}_N\}, \quad (3)$$

is assumed to follow the normal distribution with its mean μ_P and its variance σ_P^2 , where the overbar means the average over a sample. It is remarked that the central limit theorem warrants Gaussianity of sample-mean distribution even if the original data does not follow the normal distribution. A set of the sample mean of Q similarly expressed as

$$\Sigma_Q = \{\bar{Q}_1, \bar{Q}_2, \dots, \bar{Q}_N\}, \quad (4)$$

is assumed to follow the standard normal distribution. Unless Σ_Q is standardized, the Z transformation is to be taken. Further, given that the linear regression equation between Σ_Q and Σ_P , the residual variance E^2 is calculated as $E^2 = (1 - r^2)\sigma_P^2$, where r is a correlation coefficient between global and regional variables. Selecting $2M$ samples from Σ_Q , the estimation error variance is given as

$$\frac{E^2}{2M} = \frac{(1 - r^2)\sigma_P^2}{2M}. \quad (5)$$

This is the estimation error of mean in SmDS. The estimation error variance is a function of the number of selecting years, the correlation coefficient between Σ_Q and Σ_P , and the inter-sample variance σ_P^2 . Therefore, more selecting years and higher correlation between global and regional variables make the smaller estimation error variance in SmDS. Even if the samples are randomly selected, its estimation error follows Eq. (5). However, as mentioned below, if we selected the samples such that the mean of Σ_Q is zero, the bias of the mean would be zero.

Next, we will consider the bias of both mean and 99-percentile value in SmDS.

In SmDS, we select top M and bottom M years in the statistical estimation for the regional variable. Now we renumber the element of Σ_Q in its decreasing order as

$$\Sigma_{\tilde{Q}} = \{\overline{Q_{I(1)}}, \overline{Q_{I(2)}}, \dots, \overline{Q_{I(N)}}\}, \quad (6)$$

where

$$\begin{pmatrix} 1 & 2 & \dots & N \\ I(1) & I(2) & \dots & I(N) \end{pmatrix}, \quad (7)$$

is an element of n -dimensional symmetric group. Following this permutation rule, the element of Σ_P is renumbered as

$$\Sigma_{\tilde{P}} = \{\overline{P_{I(1)}}, \overline{P_{I(2)}}, \dots, \overline{P_{I(N)}}\}. \quad (8)$$

We define two sample groups as

$$\Omega_+ = \bigcup_{k=1}^M \omega_{I(k)}, \text{ and } \Omega_- = \bigcup_{k=N-M+1}^N \omega_{I(k)}, \quad (9)$$

corresponding to selecting top M and bottom M years from $\Sigma_{\tilde{Q}}$ in SmDS. The mean of P over Ω_+ and Ω_- are respectively expressed as

$$\mu_P \pm \alpha \sigma_P, \quad (10)$$

where α is the mean of the upper M/N of the normal distribution expressed as

$$\alpha = \frac{\int_{\beta}^{\infty} x N(0,1)(x) dx}{\int_{\beta}^{\infty} N(0,1)(x) dx} = \frac{N}{\sqrt{2\pi}M} \exp\left(-\frac{\beta^2}{2}\right), \quad (11)$$

noting that

$$\int_{\beta}^{\infty} N(0,1)(x) dx = \frac{M}{N}. \quad (12)$$

Hence, the expected value of sample group $\tilde{\Omega} = \Omega_+ \cup \Omega_-$ is μ_P , so that the mean of SmDS estimates is unbiased.

We next assume that the daily precipitation for the j -th sample follows log-normal distribution of

$$f_j(x; A_j, B_j) = \frac{1}{\sqrt{2\pi}B_j x} \exp \left[-\frac{(\ln x - A_j)^2}{2B_j^2} \right]. \quad (13)$$

Moreover if the (square root of) intra-sample variance, $\sigma_{0,j}$, is proportional to the j -th mean as

$$\sigma_{0,j} = v\bar{P}_j, \quad (14)$$

then the parameters of A_j and B_j in Eq. (13) are estimated as

$$A_j = \ln \frac{\bar{P}_j}{\sqrt{v^2 + 1}} \text{ and } B_j = \sqrt{\ln(v^2 + 1)}. \quad (15)$$

Here v is a proportional coefficient that is assumed to be constant. In the full DDS estimation, the ε -percentile value of X_ε is to be found such that

$$\frac{\varepsilon}{100} = \frac{1}{2N} \sum_{j=1}^N \operatorname{erfc} \left(-\frac{\ln \frac{X_\varepsilon \sqrt{v^2 + 1}}{\bar{P}_j}}{\sqrt{2 \ln(v^2 + 1)}} \right). \quad (16)$$

A Monte-Carlo simulation for sampling from the normal distribution of \bar{P}_j with the inter-sample mean of μ_p and the inter-sample standard deviation of σ_p at a fixed v provides the ε -percentile value X_ε from Eq. (16). The parameter v is approximately equal to 2 in daily precipitation in Hokkaido (not shown). Figure 2.4a shows the 99-percentile estimation value in the (μ_p, σ_p) space. The 99-percentile value is smaller for smaller mean and standard deviation. In the realistic range for daily precipitation in Hokkaido (the PDF shown in Fig. 2.4b), the 99-percentile value ranges between 20 and 100 mm day⁻¹.

Conversely, in the SmDS estimation, the ε -percentile value is \widehat{X}_ε is such that

$$\begin{aligned} \frac{\varepsilon}{100} = \frac{1}{4M} \sum_{j=1}^M \operatorname{erfc} \left(- \frac{\ln \frac{\widehat{X}_\varepsilon \sqrt{v^2 + 1}}{P_{I(j)}}}{\sqrt{2 \ln(v^2 + 1)}} \right) \\ + \frac{1}{4M} \sum_{j=1}^M \operatorname{erfc} \left(- \frac{\ln \frac{\widehat{X}_\varepsilon \sqrt{v^2 + 1}}{P_{I(N-j+1)}}}{\sqrt{2 \ln(v^2 + 1)}} \right). \end{aligned} \quad (17)$$

Similarly in Fig. 2.4a, a Monte-Carlo simulation for the selected samples satisfied with $|\bar{P}_j - \mu_p| > \beta \sigma_p$ provides the estimation of ε -percentile value in SmDS by Eq. (17). Figure 2.4b shows the ratio of SmDS to full DDS estimations for 99-percentile value for the given parameter of $2M/N = 2/15$. In the domain where the inter-sample standard deviation is smaller than the average, the SmDS can estimate the 99-percentile value correctly. Elsewhere, the SmDS tends to overestimate the 99-percentile value compared with the full DDS estimation. Thinking of the realistic (μ_p, σ_p) in daily precipitation in Hokkaido, the difference of the 99-percentile estimation by SmDS and full DDS is quite small.

A Monte-Carlo simulation for the selected samples satisfied with $\bar{P}_j > \mu_p + \beta \sigma_p$ or $\bar{P}_j < \mu_p - \beta \sigma_p$ provides the first or last term of right-hand-side of Eq. (17) (Fig. 2.4c). The first-term estimates the 99-percentile value almost twice larger than the SmDS. The 99-percentile value with only the last-term in Eq. (17) is near zero in the domain where the inter-sample standard deviation is smaller than the average; elsewhere it is larger for the large mean value. This encourages that the technique of SmDS originally proposed in Kuno and Inatsu (2014) can select two important groups with a few years where heavy precipitation frequently occurs and with another few years where heavy precipitation rarely occurs.

2.4. Results

a. SmDS setup

Figure 2.5a shows the observed daily-mean precipitation over Hokkaido in JJA. The precipitation amount is $\sim 6 \text{ mm day}^{-1}$ in Hidaka and Iburi subprefectures and is less than 4 mm day^{-1} in northern Hokkaido (See also Fig. 2.2a). This contrast is caused by mountain ranges in central Hokkaido called Hidaka Mountains (Fig. 2.2b) that blocks a warm, moist air mass from the southwest due to the summertime Asian monsoon (*cf.* Inatsu et al 2015). The standard deviation of JJA-mean precipitation shows less than 2 mm day^{-1} in almost all Hokkaido except for the part of the Hidaka and Iburi subprefectures (Fig. 2.5b). The 99-percentile value of daily precipitation (Fig. 2.5c) shows more than 80 mm day^{-1} in Hidaka and Iburi subprefectures and less than 40 mm day^{-1} in Abashiri subprefecture. A large amount of monthly precipitation is attributed to daily heavy precipitation, which is consistent with the assumption that the daily precipitation roughly follows the log-normal distribution (Section 2.3b).

Following the instruction of SmDS illustrated in Fig. 2.3, we performed the SVD analysis for an interannual variation of precipitation over Hokkaido and that of moisture flux convergence around Japan. We then obtained a set of heterogeneous maps for the first SVD mode with the squared covariance fraction being 68.7%. This mode means that an anomalously large precipitation in southern Hokkaido is related to anomalously large moisture flux convergence around northern Japan (Figs. 2.6a, b). The correlation coefficient between their time-series is 0.87 (Fig. 2.6c) and the first mode explains 43.8% of the variance in local precipitation fluctuation over Hokkaido (Fig. 2.6a). This is the evidence that moisture transported toward Hokkaido strongly controls precipitation in southern Hokkaido.

As the next step of SmDS (Fig. 2.3), we calculated the sampling index [denoted by $s(\tilde{t})$ in section 2.3a], by projecting GCMs' moisture flux convergence anomaly onto the first SVD mode (Fig. 2.7). It is noted that the projection has a non-zero average for each model, because the GCM anomaly is defined as the departure from the observed daily-mean precipitation (Fig. 2.5a). Based on the projection, we picked up 1991 and 1992 in MPI as top two, and 1995 and 1996 in MIROC as bottom two.

b. Comparison with conventional DDS

Following Kuno and Inatsu (2014), we compared the SmDS result for four sampled summers with the full DDS result for 30 summers. The daily-mean precipitation in both results is quite similar (Figs. 2.8a, b); it is more than 12 mm day^{-1} in Hidaka and Kamikawa subprefectures and less than 4 mm day^{-1} in Abashiri subprefecture. The spatial correlation coefficient between SmDS and full DDS is 0.96, while the precipitation amount is reduced by 10% uniformly over Hokkaido. The standard deviation of JJA-mean precipitation for full DDS shows more than 4 mm day^{-1} in Hidaka subprefecture and less than 2 mm day^{-1} in northeastern Hokkaido (Fig. 2.8c). The SmDS result of standard deviation of JJA-mean precipitation is underestimated in Hidaka subprefecture (Figs. 2.8c, d). The 99-percentile value of daily precipitation in both results is also similar (Figs. 2.8e, f); it is more than 80 mm day^{-1} in Hidaka subprefecture and less than 60 mm day^{-1} in northeastern Hokkaido. The spatial correlation coefficient is 0.85, while the 99-percentile value is a bit smaller around Hidaka subprefecture and is a bit larger in Abashiri subprefecture in SmDS. Hence, SmDS can also reproduce the precipitation pattern and its characteristics of the extreme events over Hokkaido in summer, which is consistent with Kuno and Inatsu (2014) for wintertime Hokkaido. Our analysis for summertime

Hokkaido thus supports the notion that SmDS can be applicable to the situation that a synoptic-scale pattern mostly controls local precipitation.

c. Interpretation of results

Recalling a statistical consideration in Section 2.3b, the mean estimate of SmDS is unbiased with an estimation error of

$$\sqrt{\frac{(1 - r^2)}{2M}} \sigma_p, \quad (18)$$

where the sample number $2M = 4$ in this paper. The inter-sample variance σ_p^2 gives a similar spatial pattern to the intra-sample variance σ_0^2 (Figures not shown) but the amount of σ_p^2 is much less than σ_0^2 . Figure 2.9a shows the correlation coefficient between statistical and DDS estimations for precipitation over Hokkaido, noting that the statistical estimation here means the projection of GCM time-series onto the first SVD mode (Fig. 2.6b). The correlation coefficient is more than 0.6 in Oshima and Ishikari subprefectures and central mountains in Hokkaido, and it is less than 0.4 in Hidaka and Shiribeshi subprefectures and northern Hokkaido. A low correlation means a weak control by a synoptic situation at least represented by the first SVD mode.

Figure 2.9b shows the estimation error given by Eq. (18). It shows more than 6 mm day⁻¹ in Hidaka subprefecture and less than 2 mm day⁻¹ northeastern Hokkaido. The spatial distribution mostly depends on the inter-sample standard deviation σ_p (Fig. 2.8c). Figure 2.9c shows the relative error of daily-mean precipitation (%) calculated by

$$\frac{\text{SmDS} - \text{full DDS}}{\text{full DDS}} \times 100. \quad (19)$$

The relative error falls within $\pm 10\%$ in Oshima and Ishikari subprefectures and eastern Hokkaido. However, the SmDS result underestimates the precipitation for full DDS

more than 30% in Hidaka subprefecture. This might be possibly attributed to the difficulty of reproducing the stratiform type of rain that was prominently observed in the western side of Hidaka mountain range (Sugimoto et al. 2013). The spatial pattern of relative error is consistent to the spatial pattern of the estimation error (Figs. 2.9b, c).

Figure 2.10a shows the ratio of SmDS to full DDS for the 99-percentile value of daily precipitation. The error range of the ratio ranges within $\pm 20\%$ except for Hidaka, Oshima and Abashiri subprefectures and the central mountains in Hokkaido. Although Section 2.3b suggested that SmDS tends to overestimate the 99-percentile value by 10%–40% (Fig. 2.4b), the SmDS underestimates the 99-percentile value more than 20% in Hidaka subprefecture. It is probably because the daily-mean precipitation in SmDS underestimates the daily-mean precipitation in full DDS more than 30% (Figs. 2.8a, b). Figures 2.10b, c show the 99-percentile value for top two and bottom two years of SmDS respectively. In almost all areas the 99-percentile value for top two years of SmDS shows much larger than that for bottom two years of SmDS. The 99-percentile value ranges showed in both maps are consistent to the ranges estimated in the error theory (Fig. 2.4c). In this study we can conclude that SmDS extracts a set of optimal years where the heavy precipitation likely occurs and another set of years where the heavy precipitation rarely occurs.

2.5. Conclusions and discussion

We have applied SmDS developed by Kuno and Inatsu (2014) to summertime precipitation over Hokkaido. By using the SVD analysis, we extracted a spatial pattern of a global variable, which mostly controls the precipitation over southern Hokkaido. Both of the spatial distributions for the mean and 99-percentile value in SmDS were similar to

those of the DDS for 30 years. This indicates that SmDS can be applied to the place where the synoptic field strongly controls the local precipitation.

The error theory for the mean and 99-percentile value in SmDS was established in this study. In SmDS estimation, the mean should be unbiased and the 99-percentile value tends to be overestimated compared with that in full DDS. Moreover, it turned out that the estimation error of the mean in SmDS depended on the correlation coefficient between global and regional variables, the number of samples, and the standard deviation of JJA-mean precipitation. Since the standard deviation of JJA-mean precipitation strongly contributes to the estimation error, the estimation error is large even if the correlation between the global and regional climate field is high. This adds a new sight for a necessary condition for the original discussion by Kuno and Inatsu (2014).

Basically, since the SmDS method is based on a statistical method, it is quite difficult to specify the reason for the difference from the full DDS statistics in a particular season in a physical sense. The SmDS only shows possible error range at the significant level of 2α within

$$\pm t_{\alpha}(2M) \sqrt{\frac{(1-r^2)}{2M}} \sigma_p, \quad (20)$$

from Eq.(18), where $t_{\alpha}(2M)$ is a *student's t-value* with the degree of freedom of $2M$. In the case of $\alpha = 0.025$, the difference between full DDS and SmDS for daily-mean precipitation falls within this range in all areas in Hokkaido for both summer and winter cases (See also Kuno and Inatsu 2014).

As mentioned in Section 2.1 and Inatsu et al. (2015), the DDS result is strongly influenced by the GCM boundary condition. Compared to the DDS result with the observed data, we found that the model climatology overestimated both the daily-mean

precipitation and 99-percentile value (Figs. 2.5, 2.8). It is likely that this overestimation is because of the bias of GCM. In climate modeling community, the ensemble mean is often used for DDS experiment (*e.g.*, Kendon et al. 2010; Donat et al. 2011; Inatsu et al. 2015) because the ensemble mean possibly provides the most optimal estimation than any other individual model mean (Pierce et al. 2009). However the DDS experiment using multi-GCM requires much more computational costs. The important thing in this problem is how to select a few subsets of GCM-RAM pairs and climate scenarios. Some studies have recently attempted to establish the method which reduces the ensemble members (*e.g.*, Pennell and Reichler 2011; Evans et al. 2013). There is a possibility that the criterion of GCM selection can be established by using the SmDS method. For instance, Kuno and Inatsu (2014) discussed that the average of the projection in each model discrete year, $\overline{s(\tilde{t})}$, is regarded as the GCM bias. If we selected a set of GCMs so that $\overline{s(\tilde{t})}$ is zero, we could reduce the GCM bias in terms of the SVD mode. Since there is a room for discussing about this, we will report it elsewhere.

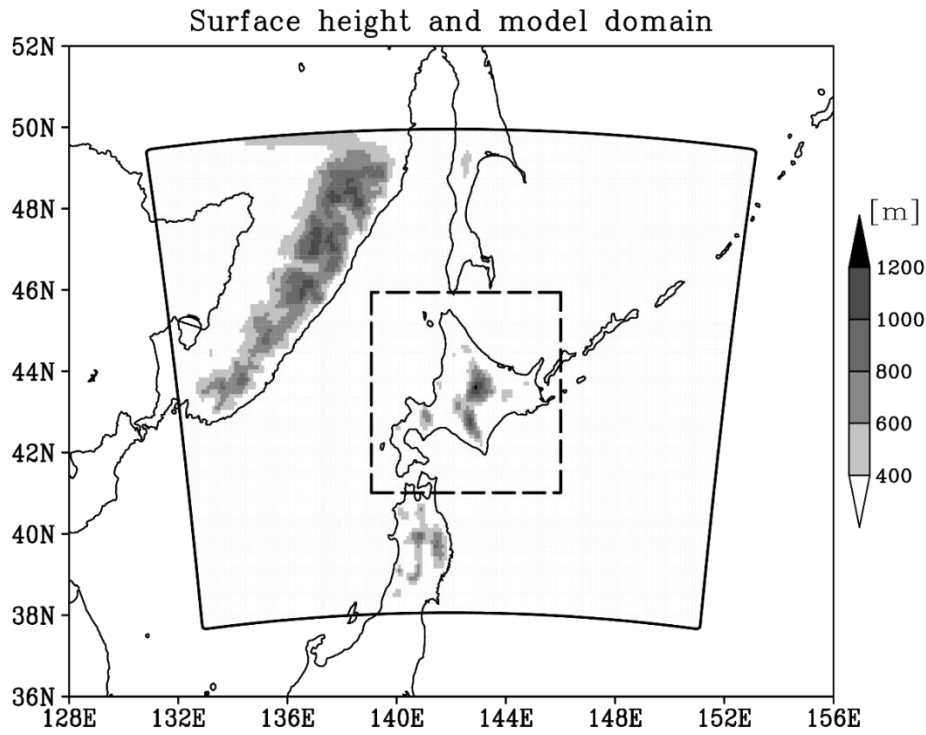


Figure. 2.1. The surface height (m) from the sea level as the bottom boundary condition for the regional atmospheric model (RAM). The shading level is shown in the reference in the right. The outer solid line indicates the lateral boundary of the RAM. The horizontal resolution is 10 km with grid number 161×133 and there are 40 vertical levels. The inner dotted line is the domain used in singular value decomposition (SVD) analysis.

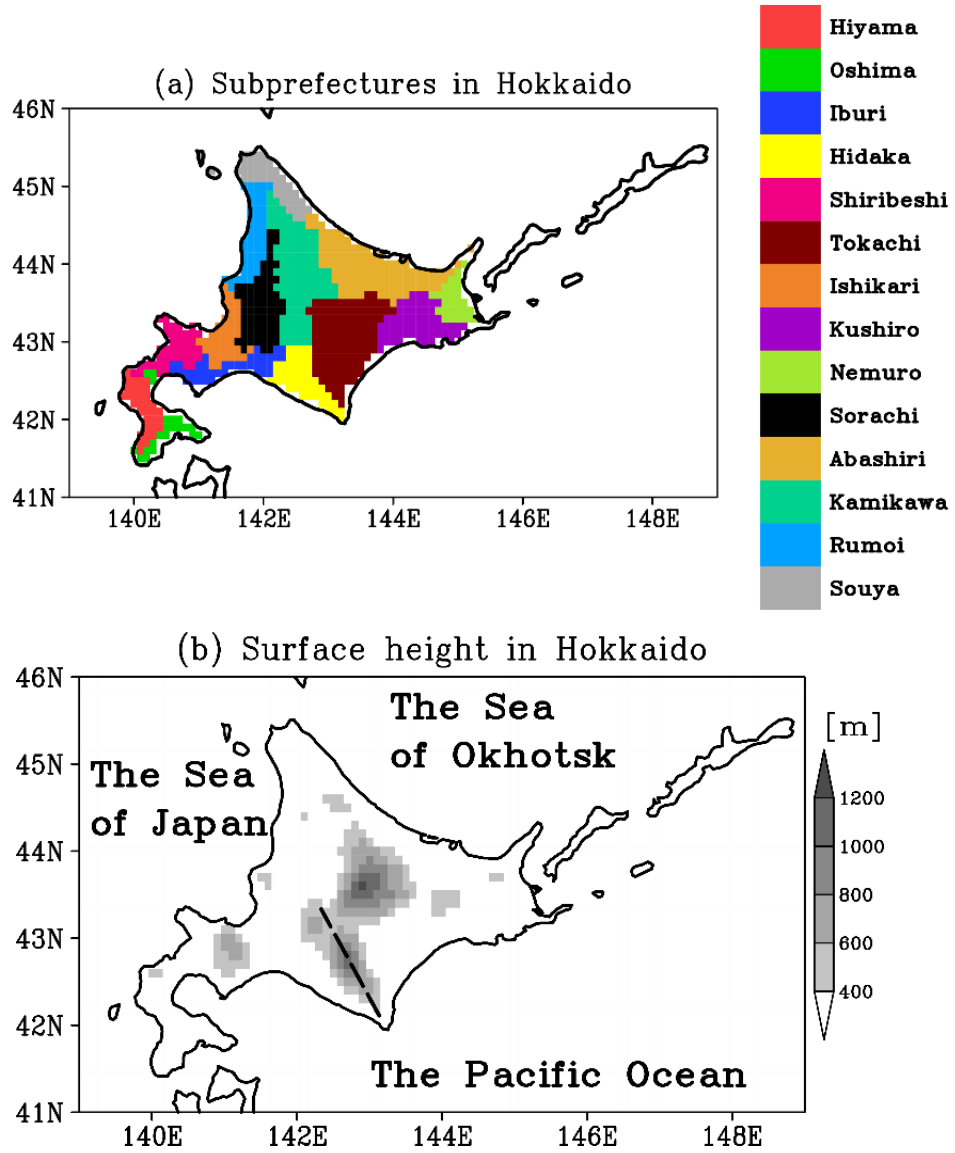


Figure. 2.2. Fourteen subprefectures in Hokkaido with their names shown in the color reference. (b) The surface height (m) in Hokkaido as the bottom boundary condition for the RAM. The shading level is shown in the reference in the right. The dashed line shows the location of Hidaka Mountains.

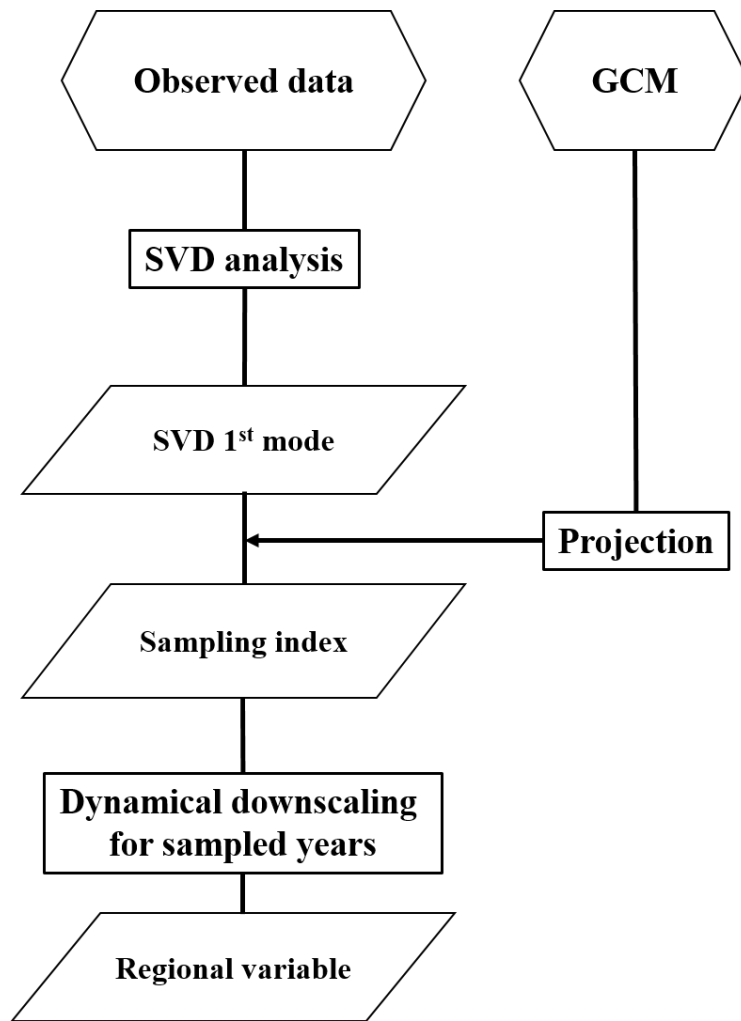


Figure. 2.3. Procedure of sampling downscaling.

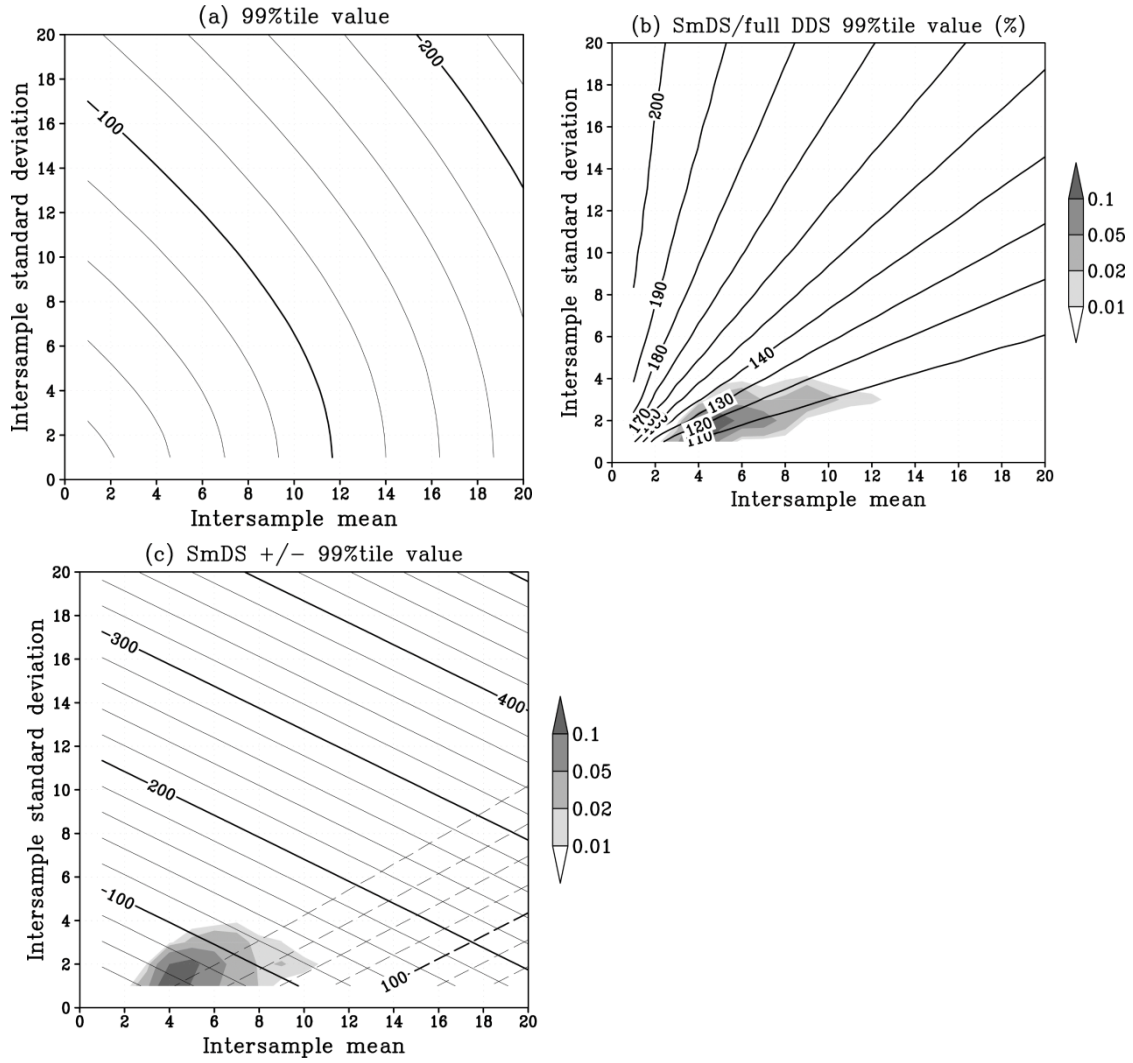


Figure. 2.4. (a) The 99-percentile value [Eq. (16)] by using a Monte-Carlo estimation with the mean μ_p in the horizontal axis and the standard deviation of σ_p in the vertical axis. The contour interval is 20 mm day⁻¹. (b) The ratio of sampling downscaling (SmDS) to full dynamical downscaling (full DDS) estimations for the 99-percentile value with contour interval 10%. The shading denotes the probability density function (PDF) of the mean and standard deviation of June-July-August (JJA) mean precipitation in full DDS simulation in Hokkaido as per the reference in the right. (c) The (solid lines) first and (dashed) last terms of the right-hand-side of Eq. (17) in SmDS estimation for the 99-percentile value. The shading denotes the PDF of the mean and standard deviation of JJA-

mean precipitation in SmDS simulation as per the reference in the right.

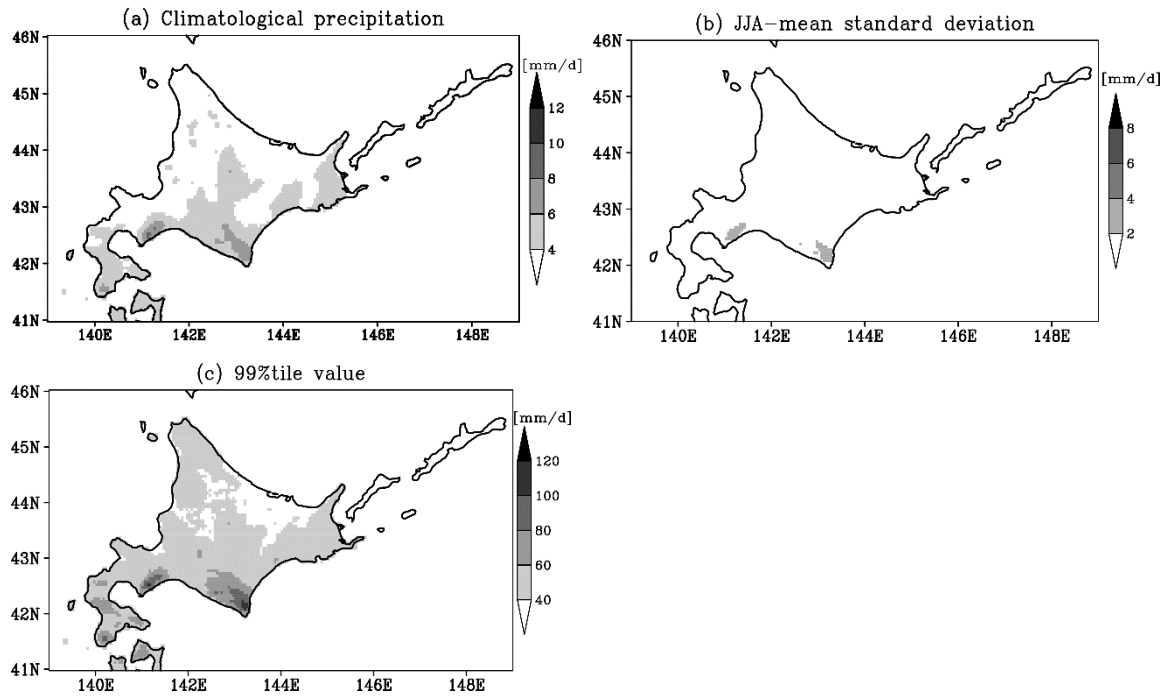


Figure. 2.5. (a) The daily-mean precipitation in JJA months (mm day^{-1}) based on APHRO_JP V1207 from 1981 to 2010 (Yatagai et al. 2012). The shading level is as per the reference in the right. (b) The standard deviation of JJA-mean precipitation (mm day^{-1}). (c) The 99-percentile value of daily precipitation (mm day^{-1}).

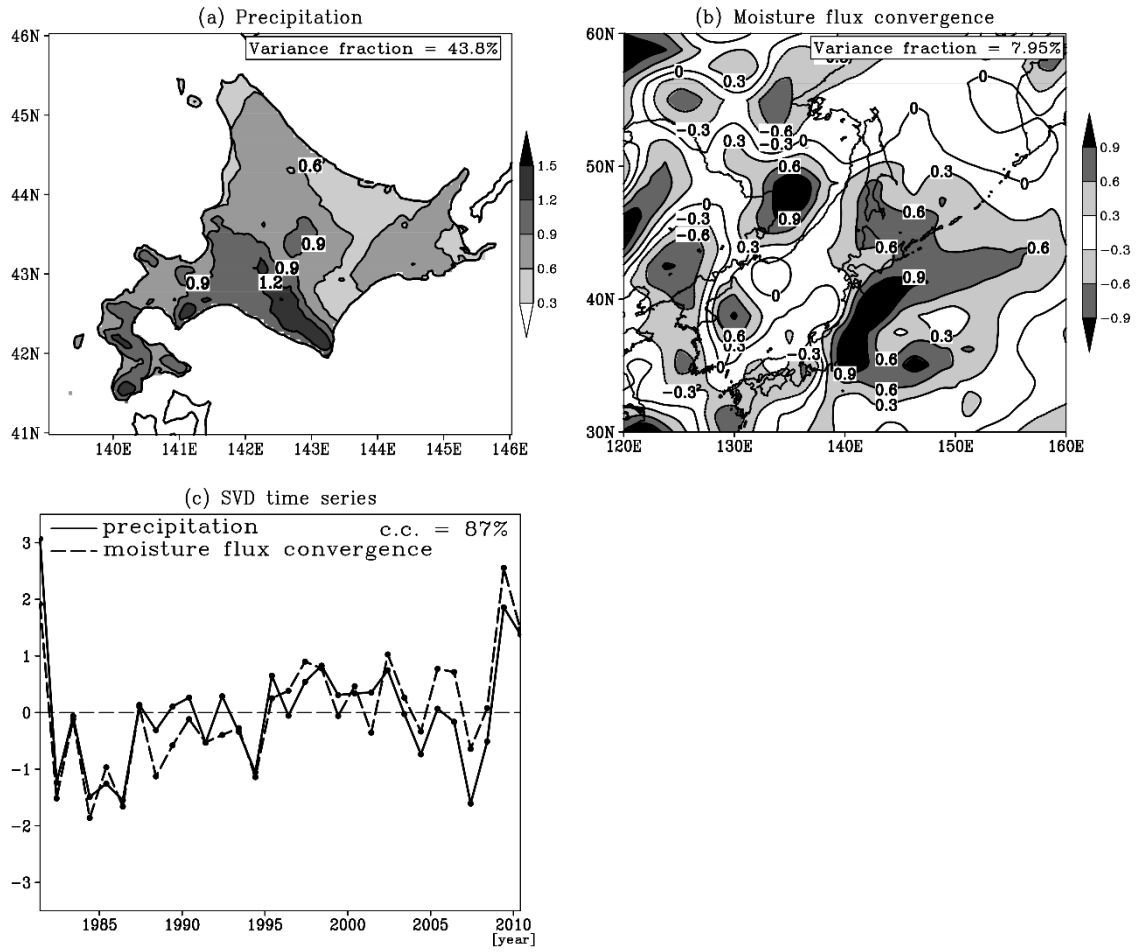


Figure. 2.6. Heterogeneous regression maps of (a) precipitation and (b) vertically integrated moisture flux convergence for the first SVD mode based on the interannual variability in JJAs from 1981 to 2010. The precipitation is based on AHORO_JP V1207, and the moisture flux convergence is based on JRA-25/JCDAS. The contour interval is 0.3 mm day^{-1} with the shading denoted in the right of each panel. (c) The time-series of (solid) precipitation and (dashed) moisture flux convergence for the first SVD mode.

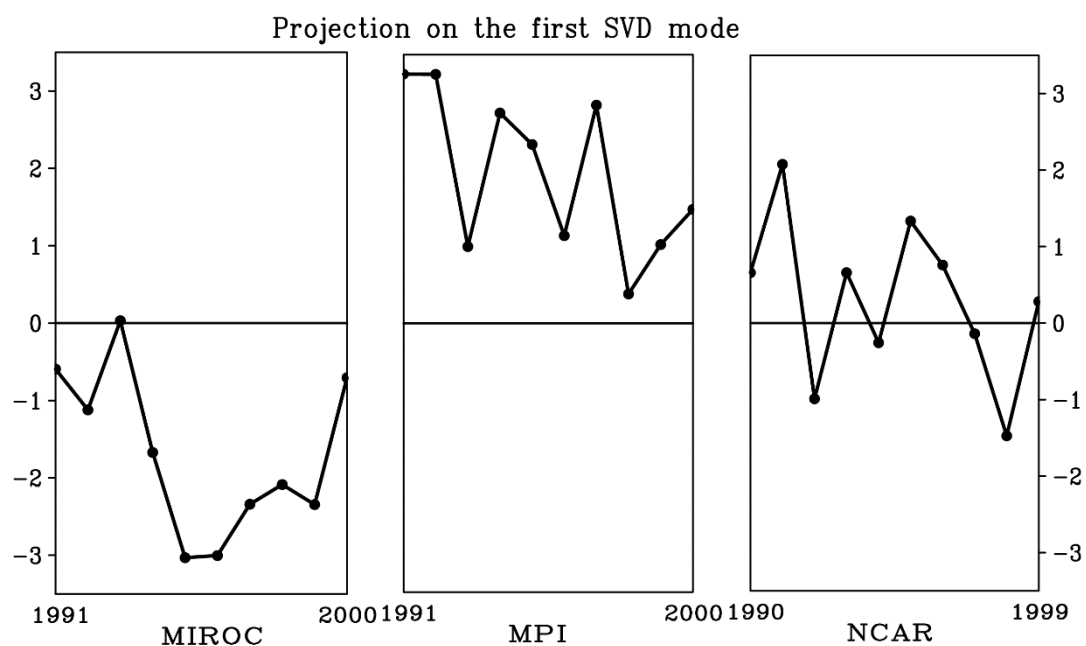


Figure. 2.7. Time-series of projection onto the heterogeneous regression map for the first SVD mode (Fig. 2.6b) under current climate experiments. Projection for MIROC, MPI, and NCAR general circulation models are plotted in left, center, and right subpanels, respectively.

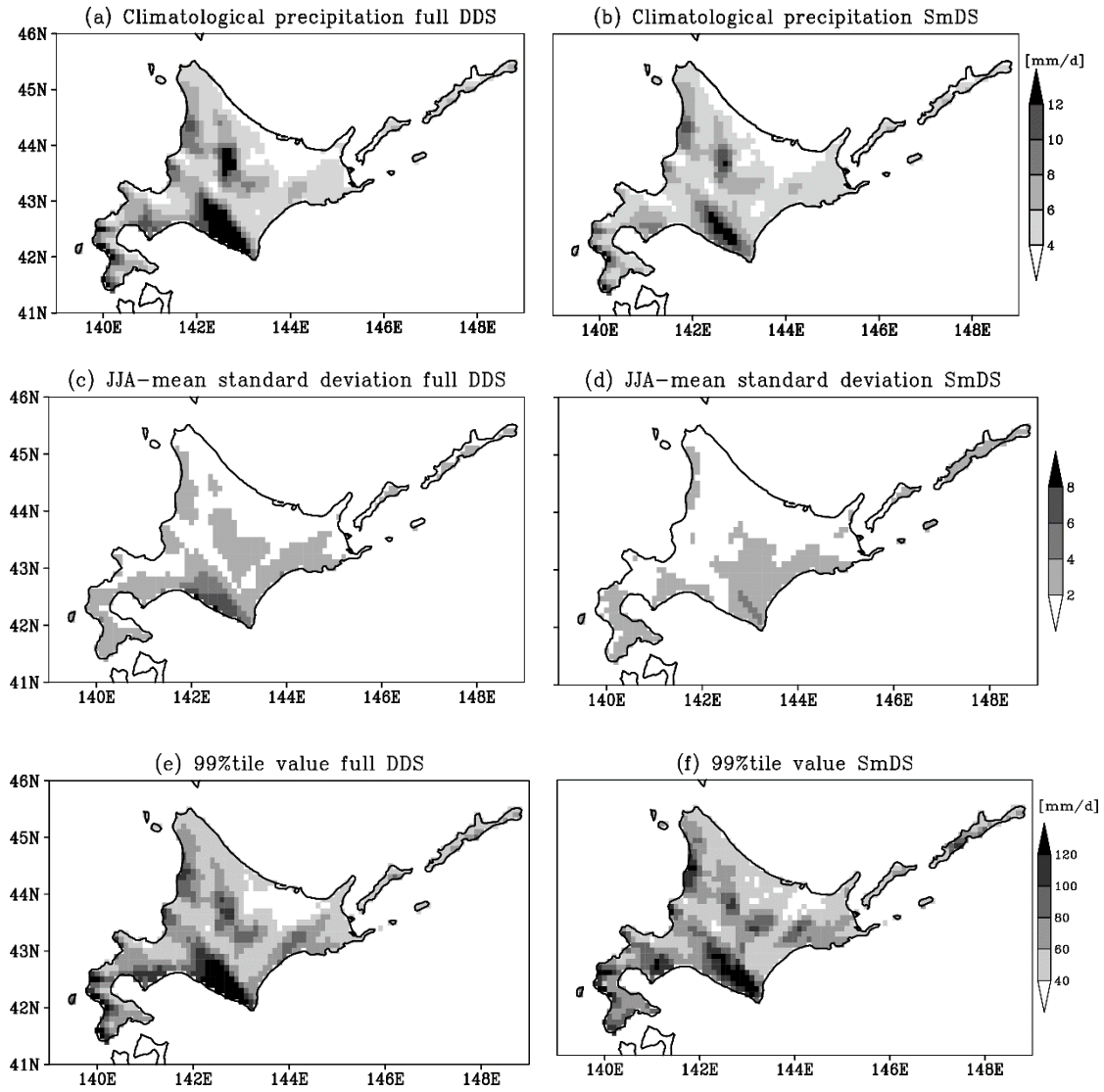


Figure. 2.8. (a, b) The daily-mean precipitation (mm day^{-1}) for (a) the full DDS and (b) the SmDS, with the shading as the reference in the right. (c, d) The standard deviation of JJA-mean precipitation (mm day^{-1}) for (c) the full DDS and (d) the SmDS. (e, f) The 99-percentile value (mm day^{-1}) of daily precipitation for (e) the full DDS and (f) the SmDS.

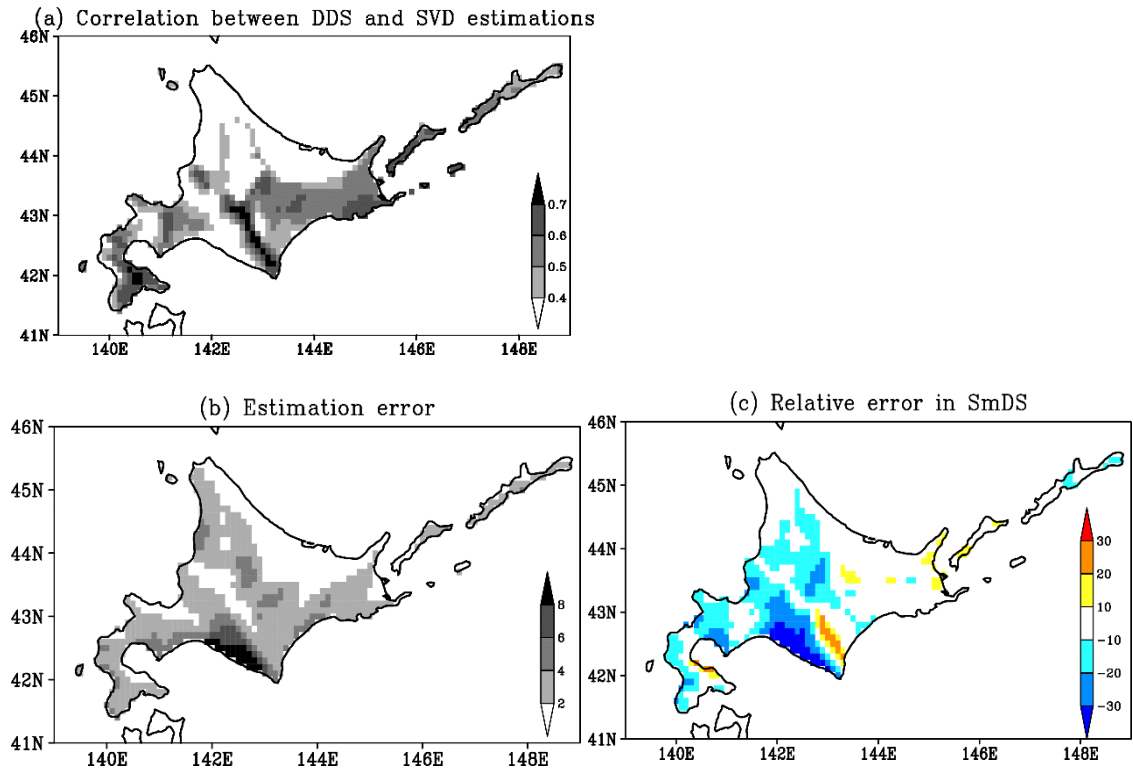


Figure. 2.9. (a) The correlation coefficient between dynamical and statistical estimations.

(b) The estimation error expressed as $\sqrt{\frac{(1-r^2)}{4}} \sigma_p$. (c) The relative error of SmDS (%)

in the daily-mean precipitation.

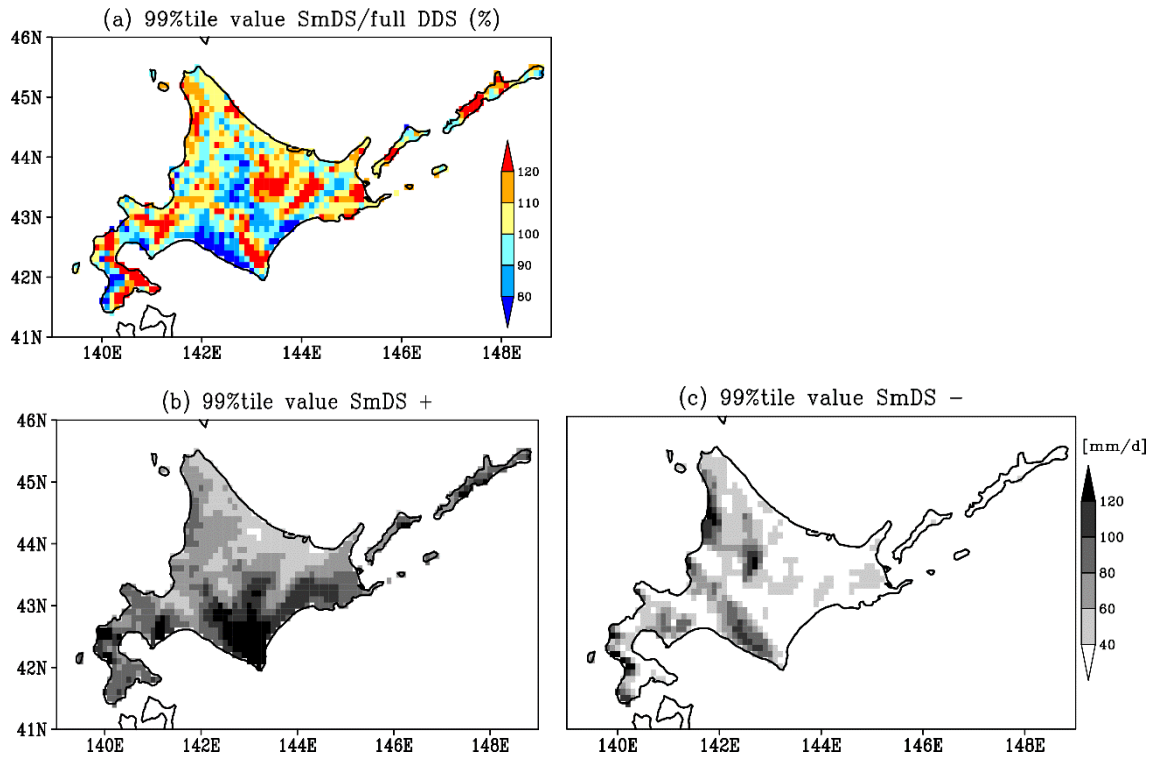


Figure. 2.10. (a) The ratio of SmDS to full DDS for the 99-percentile value of daily precipitation (%) as per the reference in the right. (b, c) The 99-percentile value of daily precipitation (mm day^{-1}) for (b) top 2 and (c) bottom 2 years for SmDS. The shading reference is in the right.

Chapter 3. Heavy rainfall duration bias in dynamical downscaling and its related synoptic patterns in summertime Asian monsoon

3.1. Introduction

Sudden heavy rainfall causes natural disasters, including flooding and inundation, landslides, erosion, and high tides. There has been a great concern about observational studies that showed a recent increase in heavy precipitation over North America (DeGaetano 2009; Pryor et al. 2009), Europe (Bartholy and Pongrácz 2007; Maraun et al. 2008; Zolina et al. 2009), and Asia (Fujibe et al. 2006; Rajeevan et al. 2008). It is anticipated that a wetter climate caused by global warming would result in a greater chance of heavy rainfall (Donat et al. 2016). A series of adaptation policies should be compiled to prepare for possible hazards due to more frequent heavy rainfall, and thus a high-resolution dataset for the precipitation change is highly required. Recently, dynamical downscaling (DDS; Giorgi 1990) has been used to fill the gap between the coarse resolution of the global climate model projection and the provincial scale of social demand. The DDS has the advantage of physical consistency over a model domain, but it contains model bias due to the unrealistic topography and physical parameterizations including cloud physics, convective parameterization, boundary layer schemes in both general circulation model (GCM) and regional climate model (RCM; (Ehret et al. 2012; Wang et al. 2004)). Therefore, we need to correct the model bias before estimating future changes from the DDS results.

The bias correction for daily and monthly precipitation amount has typically been made. Shifting and scaling (Leander and Buishand 2007; Prudhomme et al. 2002; Shabalova et al. 2003) and quantile mapping (Ines and Hansen 2006; Jakob Themeßl et al. 2011; Piani et al. 2010a) are two major methods of bias correction to daily or monthly precipitation amount. The former method scales model precipitation amount to match its climatology with observations (Shabalova et al. 2003). This method is not always suitable for heavy rainfall, however, because the estimate is highly sensitive to the scaling factor (Berg et al. 2012; Leander and Buishand 2007). The latter method adjusts the precipitation amount to maintain consistency in a cumulative distribution function between the model and observations. The quantile mapping tends to smooth the local-scale variability (Maraun 2013). It should be remarked here that there is no way to make correction if regional atmospheric model (RAM) simulates no rainfall.

When the bias correction is applied to the DDS output such as temperature or precipitation amount in future climate, the correction coefficient in quantile mapping or shifting and scaling is obtained from the climatic variable in the bias correction based on the current climate simulation. This method implicitly assumes that the model bias is time invariant. However, this stationary assumption is questionable (Christensen et al. 2008; Maraun 2012; Maraun et al. 2010). Li et al. (2018) proposed a bias correction method according to synoptic patterns related to heavy precipitation amount. They detected heavy rainfall events based on the rain-gauge data and classified the synoptic patterns related to heavy rainfall events using a self-organizing map (SOM; Kohonen 1982) with an input parameter of sea-level pressure (SLP). They then applied quantile mapping to daily precipitation with respect to the corresponding synoptic pattern. Their bias correction approach for precipitation amount may provide a possible way to overcome this stationary

assumption problem in bias correction.

On the other hand, there is only one study that attempted the correction method for rainfall duration bias. Nyeko-Ogiramoi et al. (2012) defined the length of consecutive wet days as a wet-spell and corrected the mean of wet-spell, by extending additional wet days using a kernel density estimation method (Lall et al. 1996) and replacing the end of wet days of a wet-spell with dry days. For example, if the rainfall duration changed in a catchment area consisting of a main stream and its branch rivers, the structure of hydrograph in each sub-catchment area would be changed depending on the different spatial scale and runoff coefficient of each sub-catchment area. At the downstream toe of the main stream, the timing and amount of direct runoff peak can therefore be affected by hydrographs for sub-catchments. Maraun (2013) pointed out that the temporal variation of bias-corrected precipitation amount by a quantile mapping was determined for every grid box. He also pointed out that, if these precipitation data were to be used in hydrological modeling, the flood risk would be overestimated in narrow, rapidly-responding catchments. For the above reason, the bias correction of rainfall duration is important for accurately estimating the direct runoff and flood risk in a catchment area. However, no one has yet explicitly stated how a DDS result contains the precipitation duration bias.

This study aims to provide an explicit description on the rainfall duration bias of a RAM forced with reanalysis data. The knowledge obtained in this paper is useful in that the atmospheric forcing drives a hydrological model to evaluate direct runoff in a catchment, which is often crucial for estimating flood risk. We focus on summertime heavy precipitation over Kyushu, one of the four main islands of Japan as mapped in Fig. 3.1. Recalling Li et al. (2018), it is natural that a rainfall event has the model bias of the

rainfall duration involving its related synoptic pattern. Summertime precipitation in Kyushu is generally controlled by the low-level moisture intrusion related to the Asian monsoon and typhoon passages. We apply SOM to detect typical synoptic patterns related to heavy rainfall days in Kyushu and link the patterns with rainfall duration biases. This paper is organized as follows: Section 3.2 describes the data and method. Section 3.3 clearly describes the precipitation duration bias in the DDS experiments and performs the SOM analysis to reveal the relationship between heavy rainfall days and surrounding atmospheric environment. Sections 3.4 and 3.5 provide discussion and conclusions.

3.2. Data and method

a. Observations

The rainfall observation data is the Radar/Rain gauge-Analyzed Precipitation (RA), based on 46 C-band radars operated by the Japan Meteorological Agency (JMA), the Ministry of Land, Infrastructure, Transport and Tourism (MLIT) and approximately 10,000 rain gauges of the JMA, MLIT and local governments [see Nagata (2011) for details], which have been intensively used as the verification data in many publications without additional quality controls (*cf.* Oki and Sumi 1994; Iida et al. 2006). The horizontal resolution of RA is 1 km and the analysis period is July and August from 2006 to 2015. The RA provides 1-h accumulated precipitation amount (mm) with the minimum unit of 0.4 mm h^{-1} . We regard the 1-h accumulated precipitation amount of RA as precipitation intensity (mm h^{-1}). This study focuses on Kyushu, with 38,869 RA grid points over the land originally. For comparison RA to model results, we also use the

original RA data with a sub-sample, of which the horizontal resolution is approximately 15 km as fine as the RAM used in this study (Section 3.2b). Hereafter, the sub-sampled RA is referred to as RA-S, with 181 grid points over Kyushu. We also use, as the lateral boundary condition for dynamical downscaling, three-dimensional geopotential height, horizontal wind vector, air temperature, and specific humidity, and sea surface temperature and SLP (sea level pressure) from 6-h JRA-55 reanalysis data (Kobayashi et al. 2015) originally with the resolution of TL319L60. In the SOM analysis, we use JRA-55 with 1.25° latitude/longitude grid data (Kobayashi et al. 2015).

b. RAM experiments

We used the JMA/Meteorological Research Institute non-hydrostatic model (NHM) [See Saito et al. (2006) for more details]. The horizontal resolution is 15 km with the Lambert conformal projection and there are 23 vertical levels with the terrain following coordinate system. The model domain covers the area around Japan (Fig. 3.1a). Several physical processes are implemented in the NHM, including a microphysics scheme (Ikawa and Saito 1991), moisture diffusion (Saito and Ishida 2005), a land surface and boundary layer processes (Kumagai 2004a, 2004b), and vertical diffusion (Fujibe et al. 1999). The Kain–Fritsch scheme (Kain and Fritsch 1993) is switched on to compensate for the amount of convective precipitation in the insufficient-resolution model. The NHM is integrated from June 28 to August 31 of each year from 2006 to 2015 with lateral and bottom boundary conditions given by JRA-55 original data. We exclude the period from June 28 to June 30 as the model spin-up.

c. Classification of synoptic patterns related to heavy rainfall

To classify the synoptic patterns, we use SOM and the K-means method. SOM can provide a two-dimensional map with keeping the nonlinear information. After the SOM process, we conduct K-means and obtain the synoptic patterns. This combination method of SOM and K-means has been used other studies for objectively classifying synoptic patterns (Nguyen-Le et al. 2017; Nishiyama et al. 2007; Ohba et al. 2016; Ohba et al. 2015). Our method basically follows Nguyen-Le et al. (2017) and is slightly different from Nishiyama et al. (2007), who did not apply the combined empirical orthogonal function (CEOF) analysis before SOM method.

Using daily precipitation from the RA data, we sample days on which the number of grid boxes with daily precipitation of each grid surpassing 30 mm day^{-1} exceeds 20% of the total number of grid boxes over Kyushu. We regard these detected days as “heavy rainfall days”. The area of 20% of Kyushu is set to focus on the precipitation system forced by large-scale forcing. It is noted that, if a rainfall system such as a typhoon passed midnight and if these two consecutive days satisfy the definition of a heavy rainfall day, we counted two heavy rainfall days. There are 127 heavy rainfall days in the analysis period. The dependency on area coverage of 20% on our results is discussed in Section 3.4b. For the selected dates, we prepare a set of daily mean dataset for the following climatic variables from JRA-55 with 1.25° latitude/longitude grid data: daily-averaged horizontal wind and equivalent potential temperature at 850 hPa and SLP for the domain shown in the box in Fig. 3.1a. These variables are important for intense precipitation in this region, because it is mainly caused by the Meiyu/Baiu rainband characterized by the strong meridional gradient of equivalent potential temperature and specific humidity (Ninomiya 1984; Ninomiya and Akiyama 1992; Sampe and Xie 2010; Tomita et al. 2011),

along with the low-level southwesterly along the western fringe of the North Pacific subtropical high that transports moisture from the tropics (Akiyama 1973; Kodama 1992; Ninomiya 1984; Ninomiya 2000; Ninomiya and Shibagaki 2007). Following Nguyen-Le et al. (2017), for the efficiency of learning processes in SOM, the CEOF analysis of these synoptic variables is performed in advance and 62 leading principal components, for which the explained variance is 99%, are input into the SOM program.

The CEOF analysis of these synoptic variables is performed in advance to reduce the size of input vector from 528 to 62, noting that the original size is 11 longitude grids times 12 latitude grids times 4 climatic variables of JRA-55. And then, 62 leading principal components are input into the SOM procedure. The results of the SOM analysis are generally sensitive to the number of output nodes. This study fixed it as 10×10 . The node number dependency is discussed later (Section 3.4b). A Gaussian neighborhood function is used with the learning rate set to 0.2. To relate the original SOM result to the typical synoptic patterns, we apply the *U*-matrix (Ultsch and Siemon 1990) and *K*-means methods for cluster analysis. Note that the number of cluster is fixed at 3 before conducting *K*-means, because synoptic patterns related to heavy rainfall over Kyushu were mainly categorized into three patterns even with more clusters permitted (not shown). As a consequence, we obtain three typical synoptic patterns related to heavy rainfall over Kyushu.

d. Definition of a rainfall event

Let us consider a time series of precipitation intensity at a particular grid point in Kyushu (Fig. 3.2). A single rainfall event is defined as the event in which hourly precipitation continuously exceeds 0.4 mm h^{-1} , the minimum unit of RA. The rainfall

duration is the period when the rainfall event happens. We also define the peak value (mm h^{-1}) as the maximum precipitation intensity (mm h^{-1}) in the event period.

3.3. Results

a. RAM simulations

Figures 3.3a,b show the precipitation intensity averaged in July and August (mm day^{-1}) for RA and DDS. Most of areas in the island seem to exceed 12 mm day^{-1} around mountain areas with the height over 200 m in RA (Figs. 3.1b, 3.3a), whereas the precipitation amount in DDS seems to exceed 8 mm day^{-1} around the part of northwest and along the southeast coast in Kyushu (Fig. 3.3b). The DDS then underestimates the observed precipitation amount in almost all areas in Kyushu island, particularly more than 50% underestimation over the part of the central area and almost all part of the northern area, except for an overestimation of $>10\%$ along the easternmost coast of Kyushu island (Fig. 3.3c). Figures 3.3d,e show histograms of hourly precipitation over Kyushu with the bin width of 1 mm h^{-1} and the first bin excluding zero precipitation. A histogram of hourly precipitation over Kyushu reveals that the model underestimates the rainfall with the intensity of $>10 \text{ mm h}^{-1}$ and fails to reproduce the very heavy rainfall with the intensity of $>50 \text{ mm h}^{-1}$. The RA and DDS precipitation intensity follow the log-normal distribution, but the RA precipitation intensity has a variance twice larger than that of the DDS precipitation intensity (Fig. 3.3d). In addition, the DDS has a large positive bias in the frequency of non-zero precipitation (Figs. 3.3d,e), which is generally called “drizzle problem” that GCM and RCM simulate too much non-zero precipitation (*e.g.* Maraun et al. 2010).

The discrepancy between RA and DDS is also obvious in the precipitation

duration averaged over the rainfall events, which is the total rainfall durations divided by the number of events. For DDS, two peaks of the average rainfall duration are found on the southeastern side of Kyushu with over 8 h and on the part of northwest around 131°E/33°N with over 8 h, whereas the average rainfall duration is less than 8 h over the rest of the region (Fig. 3.4a). In contrast, the RA-S provides an average rainfall duration ranging from 2 to 6 h and a small peak with over 4 h is found on the eastern side of Kyushu (Fig. 3.4b). The difference therefore shows a positive bias of rainfall duration over Kyushu, with its local maxima located on the eastern side and the northwest area in Kyushu (Fig. 3.4c). If we restrict rainfall events with their peak values over 30 mm h⁻¹, the average duration time is prolonged in DDS and RA-S (Figs. 3.4d,e) and the DDS shows the large positive bias with over 20 h in the southeastern Kyushu whereas the other areas show a relatively little bias (Fig. 3.4f).

b. Synoptic patterns related to heavy rainfall days

Table 1 shows the lists of heavy rainfall day in three clusters. We classified 53% of events as cluster C0, 27% as C1, and 20% as C2. Some consecutive heavy rainfall days across the midnight with dates falling into different clusters (marked date in Table 1), called transition in this paper, are excluded in our results for simplicity. We will discuss transition cases in Section 3.4a.

The SOM and *K*-means method produce three clusters for the synoptic patterns related to heavy rainfall days (Fig. 3.5). Cluster C0, containing 60 days, is characterized by high equivalent potential temperature air intruding into Kyushu via the low level jet (LLJ; Matsumoto 1972) and southwesterly along the western ridge of the North Pacific subtropical high. A sharp meridional gradient of equivalent potential temperature extends

from the Yellow River basin to northern Kyushu, which can be interpreted as the Meiyu–Baiu rainband (Fig. 3.5a; Ninomiya and Akiyama 1992; Sampe and Xie 2010). These characteristics are similar to the composited synoptic field with SOM in Ohba et al. (2015; See the cluster 5 in their Fig. 3), Nguyen-Le et al. (2017; See the clusters 1 and 2 in their Fig. 2) and Nishiyama et al. (2007; See the clusters 5, 6, and 8 in their Fig. 9). The composited pattern for daily precipitation in Kyushu (Fig. 3.5b) shows more than 50 mm day⁻¹ over western Kyushu related to the C0 cluster pattern. Cluster C1 suppresses the intensity of the LLJ, a westward extension of the North Pacific subtropical high and the intrusion of warm moist air toward Japan (Fig. 3.5c). The precipitation amount over Kyushu (Fig. 3.5d) is less prominent than cluster C0. Although the LLJ and southwesterly along the North Pacific subtropical high are suppressed, these characteristics of synoptic pattern are similar to the composite synoptic fields from SOM in Nguyen-Le et al. (2017; See the cluster 3 in their Fig. 2) and Nishiyama et al. (2007; See the cluster 2 in their Fig. 9). In contrast to clusters C0 and C1, cluster C2 shows strong cyclonic circulation over the East China Sea that transports warm, moist air to Kyushu (Fig. 3.5e). This typhoon pattern was also detected in Ohba et al (2015; See the cluster 6 in their Fig. 3). Collating the typhoon record with 22 dates categorized into C2, the cyclonic circulation is caused by 13 typhoon cases. The pattern brings rainfall of more than 70 mm day⁻¹ in the southerly wind area of the typhoon (Fig. 3.5f).

Using the date list for each cluster obtained from the SOM and K-means method from JRA-55 and RA (Table 1), synoptic charts and rainfall maps were also composited using DDS output (Fig. 3.6). Wind circulation and SLP are similar to the composite maps based on the reanalysis data (Figs. 3.5a,c,e), though DDS makes drier weather than JRA-55 in cluster C1. The spatial distributions in clusters C0 and C2 (Figs. 3.6b,f) are similar

to the distribution of reanalysis data (Figs. 3.5b,f), though DDS underestimates the precipitation intensity in almost all areas in Kyushu (Figs. 3.6b,d,f). Therefore, we conclude that the DDS reproduces a fundamental composite pattern classified with the SOM and *K*-means method.

c. Rainfall duration bias related to heavy rainfall days

The identification of rainfall event and rainfall duration in each cluster is restricted to dates falling into a particular cluster. Here we consider a time-series of hourly rainfall continuously lasting from 2300 UTC on July 9 to 0300 UTC on 10 July (Fig. 3.7). When both 9 July and 10 July fall into cluster C0, the rainfall event is once counted as C0 and its rainfall duration is 4 h (Fig. 3.7a). On the other hand, when only 10 July falls into cluster C0, the rainfall event is also once counted as cluster C0 but its rainfall duration is shortened to 3h (Fig. 3.7b).

Figure 3.8 shows the spatial distribution of average rainfall duration (h) in the three clusters. The average rainfall duration for clusters C0 and C1 ranges from 4 to 6 h in most areas of Kyushu (Figs. 3.8a,b), whereas the average rainfall duration for cluster C2 is more than 6 h in eastern Kyushu and less elsewhere (Fig. 3.8c). Compared with RA-S, the DDS almost reproduces the rainfall duration for clusters C0 and C1, although it overestimates the rainfall duration of C0 as 2 h longer than the observation in western Kyushu (Figs. 3.8d,e). However, DDS overestimates the rainfall duration of C2 in southern and east-coast areas in Kyushu (Fig. 3.8f) as 5 h longer than the observation. These results are quite robust because we sampled a sufficient number of rainfall events for clusters C0 and C1 (Figs. 3.9a,b,d,e) with more than 10 events. However, it should be cared that cluster C2 in DDS has less than 10 rainfall events in southern Kyushu (Fig.

3.9c).

The histograms of rainfall duration for RA-S and DDS show a log-normal distribution for all clusters (Fig. 3.10). The mean and standard deviation of cluster C2 are higher than those of the other clusters. The DDS has a positive bias of 1.3 h in cluster C0 and of 1.0 h in cluster C2 (Figs. 3.10a,c), in spite of little mean bias for cluster C1 (Fig. 3.10b). This result suggests that the duration bias depends on a synoptic weather pattern that brings heavy rainfall events. Rainfall duration biases among synoptic weather patterns are larger if rainfall is limited to cases with peak values exceeding 30 mm h^{-1} (Fig. 3.11). The mean and standard deviation of cluster C2 are higher than for other clusters in both RA-S and DDS (Fig. 3.11b). In cluster C2, the location of the entire distribution in DDS shifts to the right compared to the one in RA-S. The DDS has a positive bias of 26.2 h in cluster C2 (Fig. 3.11b) and a negative bias of 2.2 h in cluster C0 (Fig. 3.11a).

3.4. Discussion

a. Transition cases

The number of transition events are 4 cases between cluster C0 and C1, 3 cases between cluster C0 and C2, and 1 case between C1 and C2. Figure 3.12 shows the daily-mean SLP, horizontal wind and equivalent potential temperature at 850 hPa for the 4 transition events between cluster C0 and C1. Stationary LLJ due to the Baiu-front and southwesterly along the North Pacific subtropical high exists both cluster C0 and C1. Moreover, cluster C0 is also characterized the passage of meso- α -scale cyclone around Kyushu (Figs. 3.12c,f,i), which may transport more moisture to Kyushu compared to cluster C1 (Figs. 3.12b,d,e,g,h). Cluster C0 on 10 July 2009 (Fig. 3.12a) is characterized

by the confluence of the LLJ due to the Baiu-front and cyclonic circulation located around 132°E/20°N, which may transport more moisture compared to cluster C1 on 11 July 2009.

Three transition events between cluster C0 and C2 is characterized by strong cyclonic circulation due to the typhoon (Fig. 3.13). Although Figs. 3.13b,d,f are classified to cluster C0 with SOM, but all these dates are obviously a typhoon pattern located around the northwest sea of Kyushu. SOM classified this case into C0, in spite that the heavy rainfall days are much influenced by typhoon (Figs. 3.13b,d and f). This kind of classifications with SOM is also found in transition between C1 and C2 (Fig. 3.14). On 18 July 2012, a typhoon located around 125°E/33°N transported moisture into Kyushu (Fig. 3.14a) and it moved northward on 19 July 2012 (Fig. 3.14b). On 19 July 2012, the advection of moisture into Kyushu seemed to be influenced by both typhoon circulation and southwesterly along the western fringe of the North Pacific subtropical high (Fig. 3.14b). As described above, the SOM analysis did not always lead to the result consistent with synopticians' intuition, especially in a case where a typhoon resides at a different location from the position where a cluster points.

b. Sensitivity tests

We here check the node number dependency in SOM. Table 2 shows the mean differences of rainfall duration (DDS minus RA-S) in all rainfall events of the heavy rainfall days over Kyushu in different SOM experiments as the node number changes from 6×6 to 12×12 . Almost all the experiments objectively classify the synoptic patterns related to heavy rainfall, similar to patterns with a node number of 10×10 (not shown). However, SOM with a node number of 9×9 provided a different cluster set. Clusters C0 and C2 (Figs. 3.15a,e) in the 9×9 SOM are the same as the standard setting (Figs. 3.5a,e),

but the composite pattern for cluster C1 in the 9×9 SOM also shows a typhoon pattern that brings heavy rainfall to western Kyushu (Figs. 3.15c,d). The mean differences in rainfall duration in cluster C2 are higher than in the other clusters in almost all experiments, though the DDS has a negative bias of 3.2 h with a node number of 9×9 and 1.0 h with a node number of 8×8 . In cluster C2, large positive biases are also evident in rainfall events with a peak value over 30 mm h^{-1} , except experiments with a node number of 8×8 and 9×9 (not shown). Therefore, the node number dependency has little effect on the results in this paper.

We next discuss the area coverage dependency on the definition of heavy rainfall days. Table 3 shows the mean bias of rainfall duration in all rainfall events of the heavy rainfall days in different SOM experiments with area coverages ranging from 5% to 40%. The node number is fixed as 10×10 . All the sensitivity experiments objectively classify synoptic patterns compared to the standard setting (not shown). Rainfall duration biases are higher in cluster C2 than in other clusters for area coverages of 5%, 10% and 25%, whereas cluster C0 has higher positive biases than cluster C2 for area coverages of between 15, 20 and 30-40%. In contrast, for rainfall events where the peak value exceeds 30 mm h^{-1} , rainfall duration bias in cluster C2 have a large long-standing bias ranging from +6.4 to +26.2 h within the area coverage from 5% to 25%, whereas the cluster C0 has a negative duration bias ranging from -4.1 to -0.5 h (Table 4).

The sensitivity of threshold for heavy rainfall day is moreover remarked. Table 5 shows the mean difference of rainfall duration (DDS minus RA-S) in all rainfall events of heavy rainfall days among the different threshold (mm day^{-1}) for heavy rainfall days. Here the other settings are the same as the standard experiment. All the sensitivity experiments objectively classify synoptic patterns into strong monsoon, weak monsoon,

and typhoon (not shown). The experiment of threshold of 10 mm day^{-1} shows more positive bias compared to the standard experiment in clusters C1 and C2. On the other hand, the experiment with the threshold of 50 mm day^{-1} shows a negative bias of 0.4 h in cluster C1, and the positive bias in cluster C2 is smaller than the experiment of threshold of 10 and 30 mm day^{-1} . A positive bias in cluster C2 is also evident in rainfall events with a peak value over 30 mm h^{-1} (Table 6). The amount of positive duration bias is +4.9 h in the case of threshold of 10 mm day^{-1} (Table 6). The threshold of 30 mm h^{-1} is therefore one of the reasonable values to keep enough events for some statistics for every cluster.

c. Model biases

This study provided the precipitation bias information with the RAM results with 15-km horizontal resolution. Heavy rainfall in Kyushu is mainly attributed to orographic precipitation associated with the low-level wind. We speculate that the smoothed topography of RAM with a resolution of 15 km may weaken the convection, which could lead to a positive rainfall duration bias. Additionally, the rainfall intensity and duration in mesoscale-convective systems are controlled by the interaction between vertical wind shear and cold pool (Rotunno et al. 1988), and by locally low-level wind convergence by convective heating (Kato and Goda 2001), of which the spatial scale is the meso- β scale or smaller. The model resolution of 15 km that we used may be insufficient to reproduce these mesoscale environmental fields accurately. This was shown in the total precipitation amount in the DDS (Fig. 3.6) compared with the observation (Fig. 3.5). However, it is worthwhile noting that the typhoon in the DDS was well reproduced in terms of its position. Figure 3.16 shows the location of 22 typhoon centers associated with cluster C2 with the capital letters of JRA-55 and the small letters of DDS. Here the typhoon center

is defined as the minimum value of SLP. The average of the difference of center of typhoon between DDS and JRA-55 is 207.0 km. The minimum distance is 18.4 km (Label E/e) and the maximum distance is 665.7 km (Label A/a).

The frequency of rainfall events in the DDS is also a problem. We obtained 42,286 events in the RA output and 13,840 events in the DDS output (Figs. 3.3d,e). The causes of this difference are speculated that NHM with the 15-km resolution did not well reproduce meso-scale convective systems and then several rainfall events detected in RA are possibly counted as a single event in NHM because of the non-zero precipitation bias. This means that the rainfall duration bias could not perfectly corrected with conventional methods such as quantile mapping or shifting and scaling, because they are unable to correct the number of dry days.

The bias correction of rainfall amount and frequency is crucial for hydrological applications. Precipitation intensity and frequency is related to frequency of precipitation types including stratiform/convective precipitation and drizzle. It is necessary to examine the precipitation frequency and intensity, not only duration, in order to accurately evaluate the rainfall bias in the DDS with considering the precipitation characteristics (Dai 2006). While the shifting and scaling and quantile mapping are generally applied to the daily or monthly data (e.x. Bordoy and Burlando 2013; Lafon et al. 2013), no one proposed a reasonable way to correct the precipitation intensity with hourly timescales. Hence there is still an open question how to correct the precipitation intensity. On the other hand, as described in Introduction, the rainfall duration bias would also be another important problem when we estimate the timing and amount of direct runoff peak in a catchment. The shifting and scaling method and quantile mapping method could possibly lead to an imprecise impact assessment, even if the total precipitation amount is exactly corrected;

they work as if a stratiform-type rainfall event characterized by prolonged moderate rainfall changed to a long-standing convective-type rainfall event.

The spatial and time scale in stratiform and convective precipitation may contribute to the surface runoff or infiltration processes. For example, Toews et al. (2009) classified convective and stratiform precipitation based on daily precipitation data by focusing on the difference of spatial scales; and they suggested that stratiform precipitation has much more impact on groundwater recharge rather than convective precipitation. On the other hand, we have emphasized the difference of time scale between stratiform and convective precipitation. If one thought of precipitation events with the same precipitation amount, the duration time would be a key agent in evaluating the surface-runoff and infiltration processes. We will refer this matter to a future paper.

3.5. Conclusions

We have investigated the rainfall duration bias with a RAM over Kyushu, Japan, in July and August from 2006 to 2015. The results showed that the DDS provided a dry bias (Fig. 3.3) and a long-standing rainfall bias, especially over eastern Kyushu and in the part of northwest in Kyushu (Fig. 3.4c). The rainfall bias was emphasized for rainfall events with the strong rainfall peak (Fig. 3.4f). Using SOM and the *K*-means method, we objectively extracted three typical clusters of synoptic patterns related to heavy rainfall days: strong monsoon, weak monsoon, and typhoon (Fig. 3.5). The cluster analysis clarified that the model bias of rainfall duration depended on the synoptic patterns. The long-standing biases were in western Kyushu under the strong monsoon environment and in southern and east-coast Kyushu when a typhoon approaches from the south (Fig. 3.8). The typhoon bias was related to a strong rainfall peak in rainfall events (Fig. 3.11b).

A possible approach to correct the rainfall duration bias would be to scale rainfall durations uniformly for all rainfall events for the model output, so that the mean of rainfall durations for the model matches that for the observations. For example, for a positive duration bias, we could cut the rainfall days from an event and equally distribute the removed amount to the remaining rainfall. It is beyond the scope of this paper to propose a feasible method for bias correction of rainfall duration, however.

Tables

Table 3.1. List of heavy rainfall days for each cluster. Dates with mark #, *, and † show transition from or toward clusters C0, C1, and C2, respectively.

C0			C1		C2	
20060701	20090701	20130703	20080701	20140702#	20060817	20140730
20060702	20090710#	20130706	20080808	20140706	20060818	20140731
20060704	20090721	20130726	20080827	20140819		20140801
20060705	20090724	20130804	20080829	20140821	20070712	20140802*
20060706	20090725#	20130823		20140829	20070713	20140807
20060719		20130824	20090711#		20070714	20140808
20060720	20100702	20130825	20090726#	20150704	20070802	20140809
20060721	20100703	20130830	20090814	20150706		
20060722	20100711#	20130831		20150720	20090808	20150711*
20060723	20100728		20100708	20150721		20150824
20060831	20100811	20140703#	20100710#	20150722	20110717	
		20140709	20100712#	20150816	20110718	
20070701	20110704	20140712	20100713	20150829	20110805	
20070702	20110705	20140803*	20100714	20150830	20110806	
20070703	20110706	20140804		20150831		
20070705	20110814	20140805	20110820		20120716	
20070706	20110815		20110821		20120718 †	
20070707		20150702	20110822		20120801	
20070708	20120701	20150712*	20110823		20120822	
20070710	20120702	20150713			20120826	
	20120704	20150812	20120719 †		20120827*	
20080717	20120706		20120720			
20080816	20120711		20120722			
20080819	20120712		20120810			
20080822	20120713					
	20120714					
	20120813					
	20120828*					

Table 3.2. The mean difference (h) of rainfall duration (DDS minus RA-S) in all rainfall events of heavy rainfall days excluding transition days among different node numbers. Here the standard experiment in this study is the node number with 10×10 .

Node number	6×6	7×7	8×8	9×9	10×10	11×11	12×12
C0	+1.1	+1.1	+1.3	+1.0	+1.3	+1.4	+1.4
C1	+0.3	+0.4	-0.2	+3.2	0.0	0.0	+0.3
C2	+1.0	+0.9	-1.0	-3.2	+1.1	+1.0	+2.7

Table 3.3. The mean difference (h) of rainfall duration (DDS minus RA-S) in all rainfall events of heavy rainfall days excluding transition days among different area coverages with the node number of 10×10 . Here the standard experiment in this study is the area coverage with 20 %.

Area coverage (%)	5	10	15	20	25	30	35	40
C0	+1.7	+1.5	+1.5	+1.3	+1.0	+1.1	+1.0	+1.0
C1	+0.4	+0.7	+0.1	0.0	-0.3	-0.1	-0.1	-0.8
C2	+2.5	+1.8	+0.9	+1.1	+2.9	-1.0	+0.4	+0.4

Table 3.4. The mean difference (h) of rainfall duration (DDS minus RA-S) in the rainfall events excluding transition days of which peak value exceeds 30 mm h⁻¹ among different area coverages with the node number of 10×10. Hyphens in the table show the case that the number of rainfall events with a peak value over 30 mm/h is less than 10 events either DDS or RA-S. Here the standard experiment in this study is the area coverage with 20 %.

Area coverage (%)	5	10	15	20	25	30	35	40
C0	-0.43	-2.7	-0.5	-2.1	-4.1	-3.3	-	-
C1	-	-	-	-	-	-	-	-
C2	+6.4	+25.7	+26.2	+26.2	+22.5	-	-	-

Table 3.5. The mean difference (h) of rainfall duration (DDS minus RA-S) in all rainfall events of heavy rainfall days excluding transition days among the different threshold (mm day⁻¹) for heavy rainfall day. Here the standard experiment in this study is the threshold with 30 mm day⁻¹.

Threshold (mm day ⁻¹)	10	30	50
C0	+0.9	+1.3	+1.1
C1	+1.6	0.0	-0.4
C2	+2.6	+1.1	+0.4

Table 3.6. The mean difference (h) of rainfall duration (DDS minus RA-S) in the rainfall events excluding transition days of which peak value exceeds 30 mm h⁻¹ among different thresholds with the node number of 10×10. Hyphen in the table shows the case that the number of rainfall events with a peak value over 30 mm/h is less than 10 events either DDS or RA-S. Here the standard experiment in this study is the threshold with 30 mm day⁻¹.

Threshold (mm day ⁻¹)	10	30	50
C0	-	-2.1	-0.8
C1	-3.8	-	-
C2	+4.9	+26.2	-

Figures

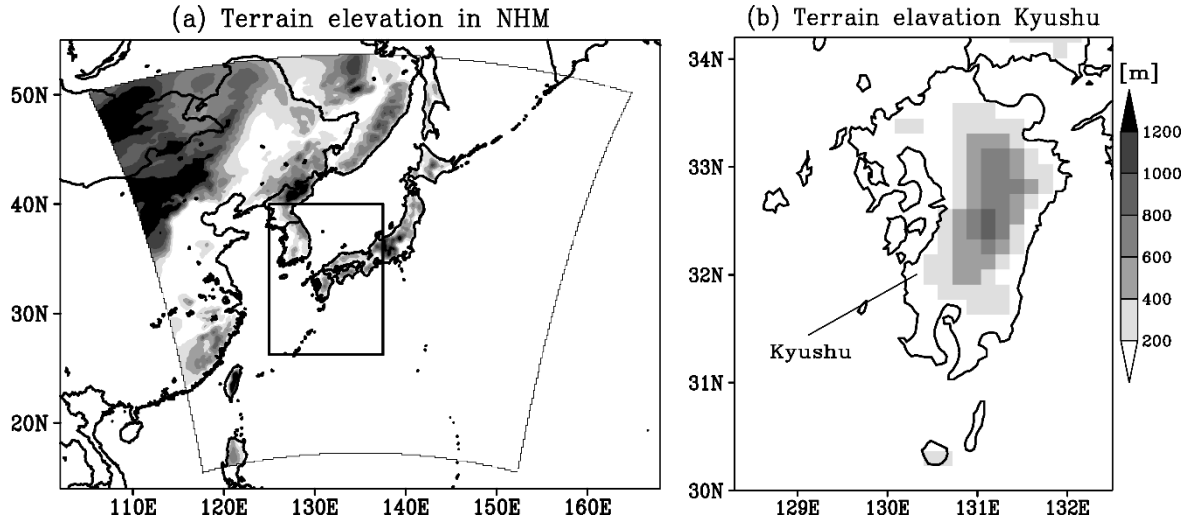


Figure 3.1. (a) Terrain elevation in the non-hydrostatic model (NHM) domain and (b) magnification over Kyushu. The shading scale is shown on the right. The inner solid box in (a) shows the domain for our self-organizing map (SOM).

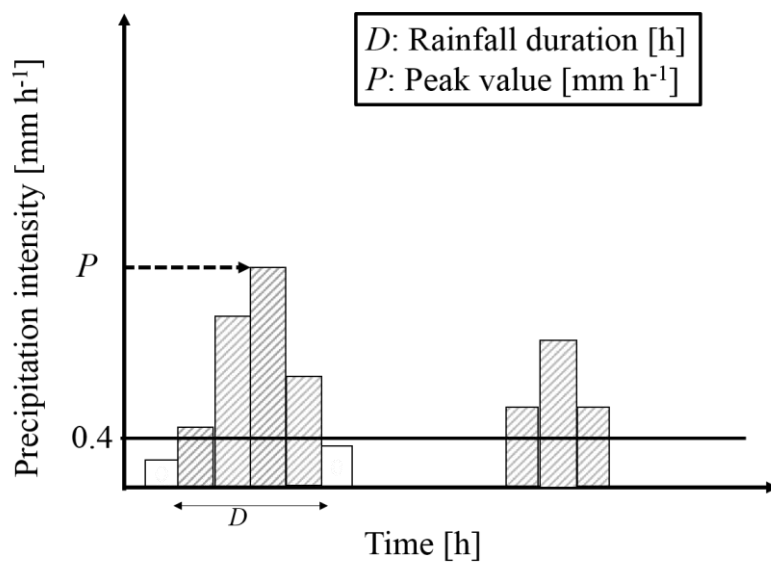


Figure 3.2. Schematic diagram for the definition of rainfall duration (D ; h) and peak value (P ; mm h⁻¹) of a particular grid point in Kyushu. The sequence of hatched bars is regarded as a single rainfall event.

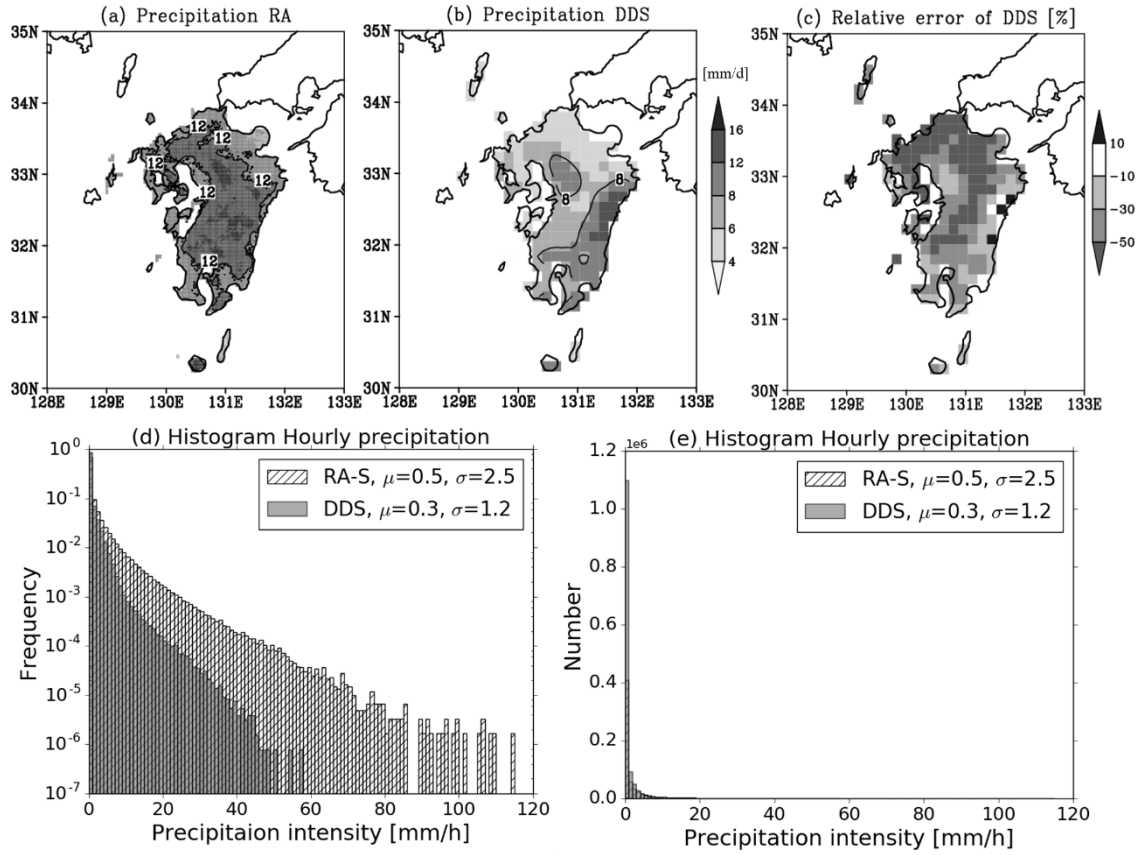


Figure 3.3. (a,b) July–August mean precipitation (mm day^{-1}) for (a) Radar/Rain gauge-Analyzed Precipitation (RA) and (b) dynamical downscaling (DDS) with the shading reference in the right. Contour shows (a) 12 mm day^{-1} in RA and (b) 8 mm day^{-1} in DDS. (c) Relative error of DDS (%) in the July-August mean precipitation with the shading reference on the right. (d) Histograms of hourly precipitation (mm h^{-1}) in RA-S (hatched bar) and DDS (gray bar) over Kyushu. The bin width is set to 1 mm h^{-1} , and mean μ and standard deviation σ are provided in the legend. (e) Same as (d), but y axis shows the number.

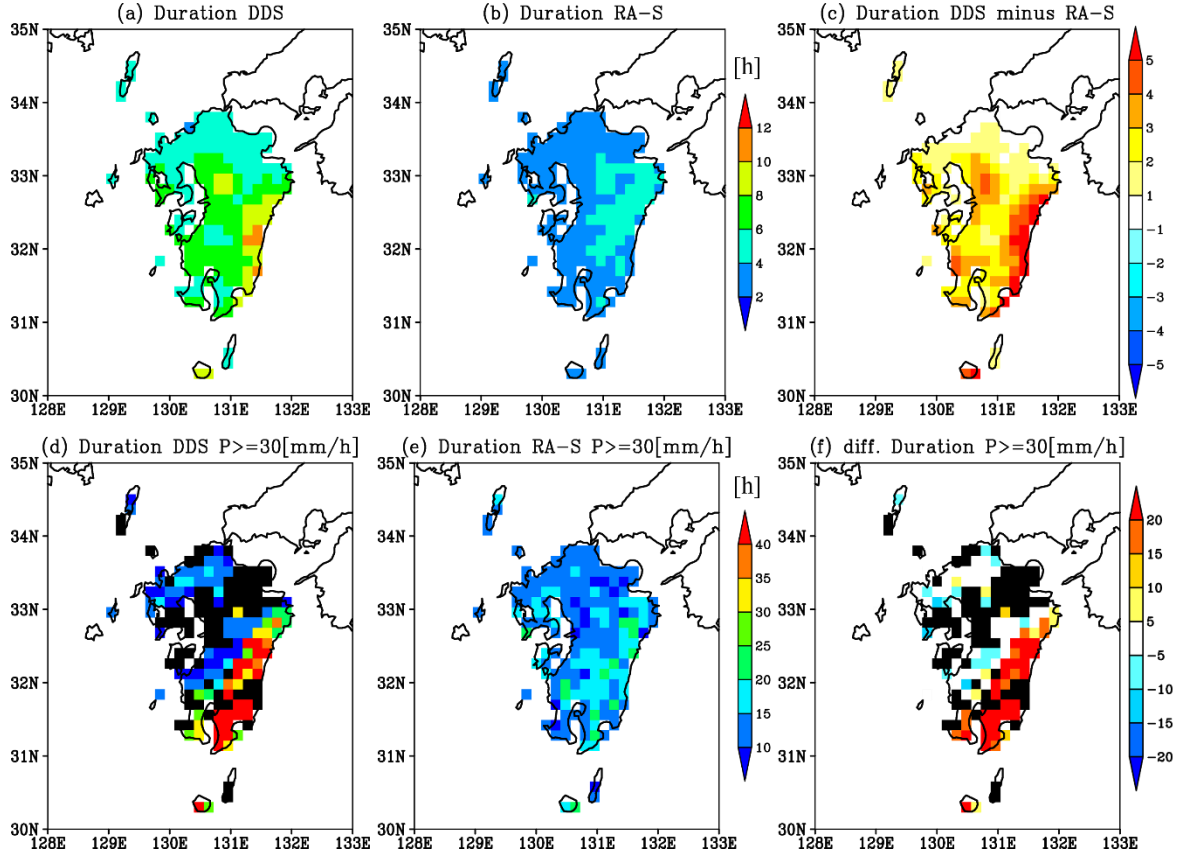


Figure 3.4. (a,b) Average rainfall duration (h) for (a) DDS and (b) RA-S for all rainfall events during July and August from 2006 to 2015. (c) Difference between DDS and RA-S for average rainfall duration (h). (d-f) Same as (a-c), but for rainfall events of which peak value exceeds 30 mm h⁻¹. Black shadings in (d) and (f) show no rainfall event with its peak value exceeding 30 mm h⁻¹.

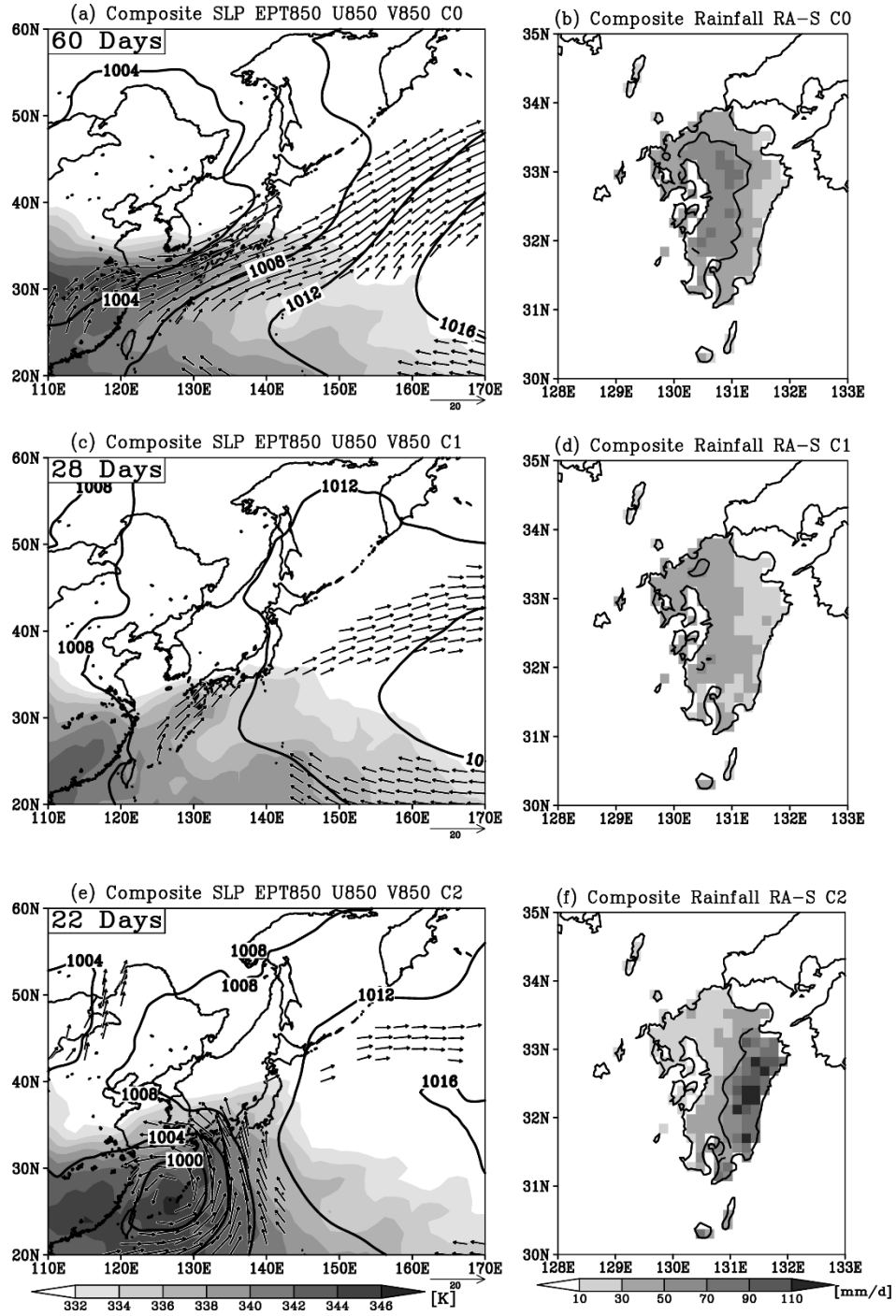


Figure 3.5. (a,c,e) Composites excluding transition days for clusters (a) C0, (c) C1, and (e) C2 of (contours) daily mean sea-level pressure (SLP), (shading) 850 hPa equivalent potential temperature, and (vectors) 850-hPa horizontal wind based on JRA-55 reanalysis data. Contour interval is 4 hPa; the shading reference and

the unit vector of 20 m s^{-1} are posed at the bottom of (e), and the vector $<5 \text{ m s}^{-1}$ is omitted. The number of heavy rainfall days is shown in the upper-left corner. (b,d,f) Composite for clusters (b) C0, (d) C1, and (f) C2 of (shading) RA-S precipitation in Kyushu island (mm day^{-1}) and (contour) RA precipitation of 50 mm day^{-1} .

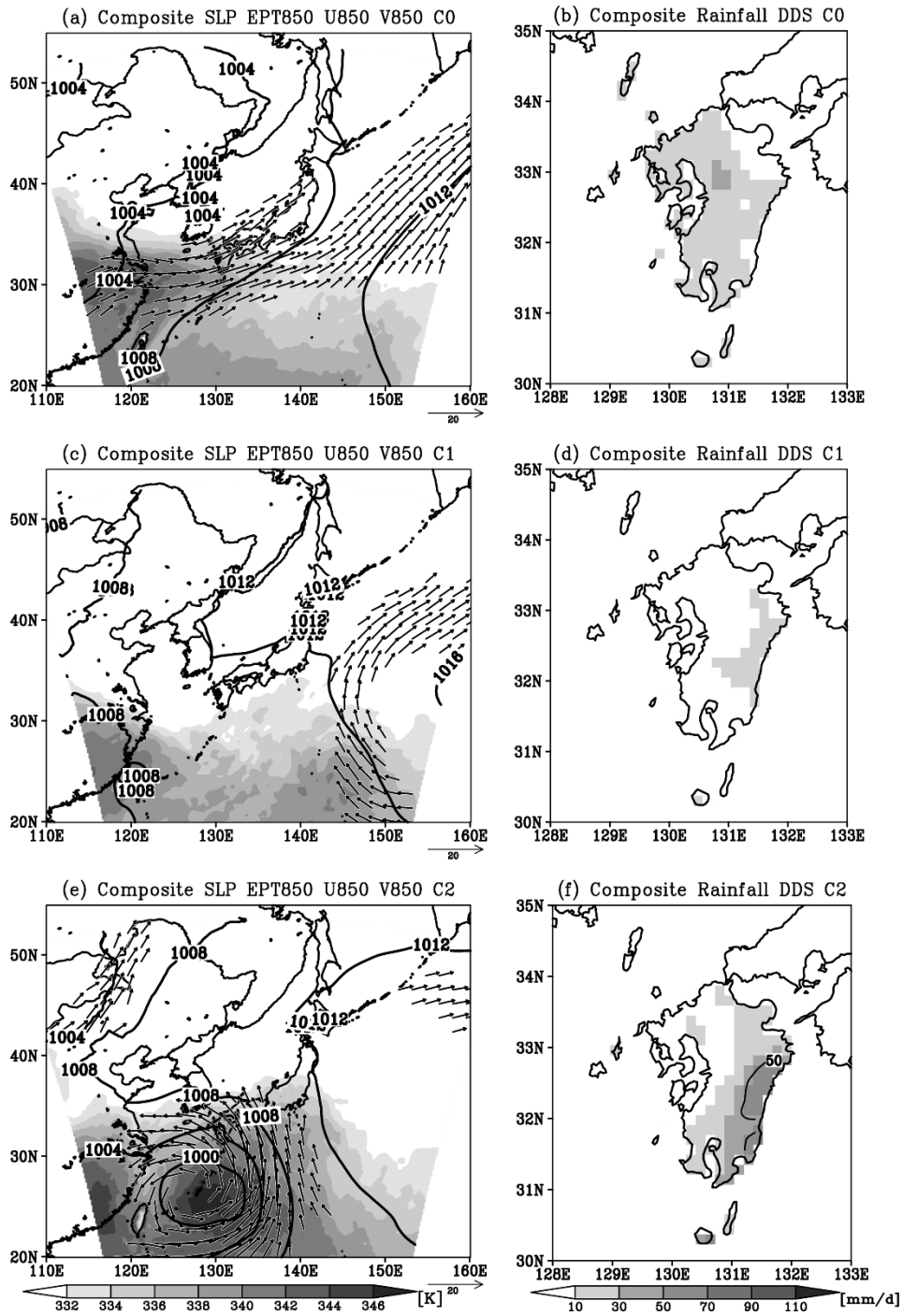


Figure 3.6. Same as Fig. 3.5, but for composites of DDS results for the dates classified with SOM based on JRA-55 and RA.

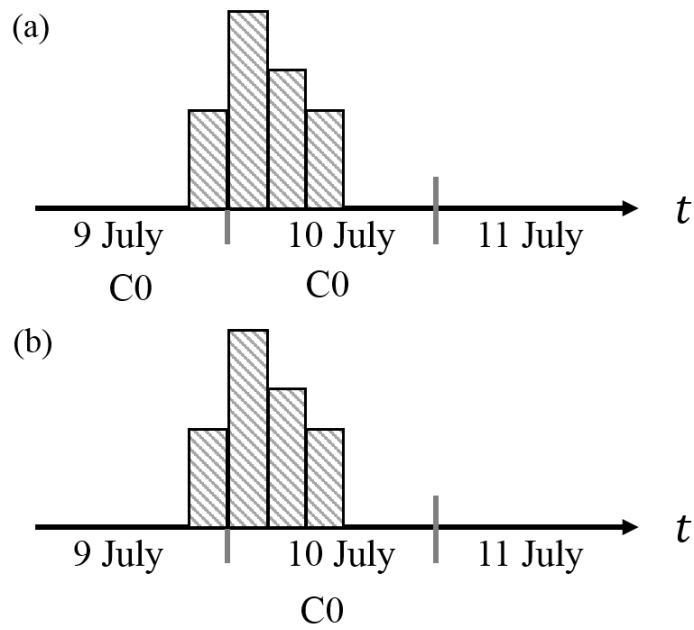


Figure 3.7. An example of a continuous rainfall across the midnight between 9 and 10 July with (a) both the dates fallen into the same cluster C0, and (b) one date fallen into cluster C0 but the other not.

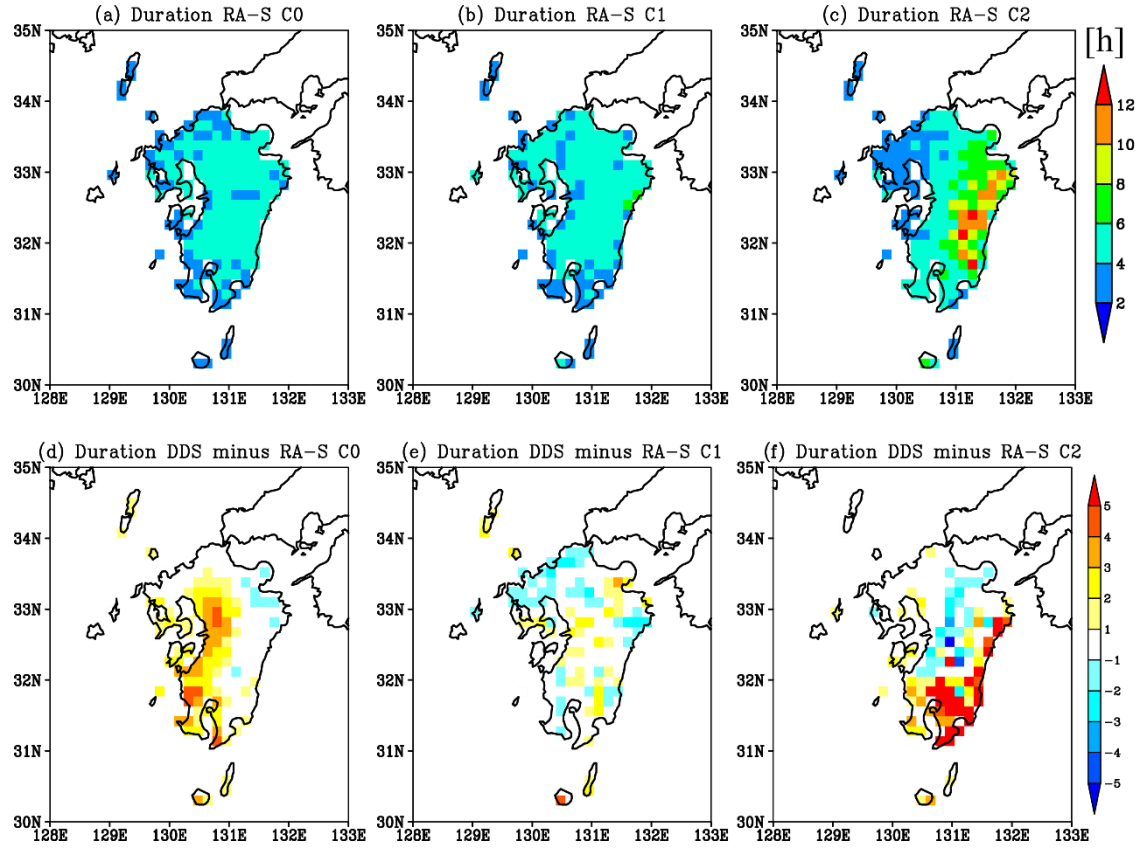


Figure 3.8. (a–c) Average rainfall duration (h) in the clusters (a) C0, (b) C1, and (c) C2 with the shading reference in the right. (d–f) Difference in average rainfall duration (h) between DDS and RA-S (DDS minus RA-S) in the clusters (d) C0, (e) C1, and (f) C2.

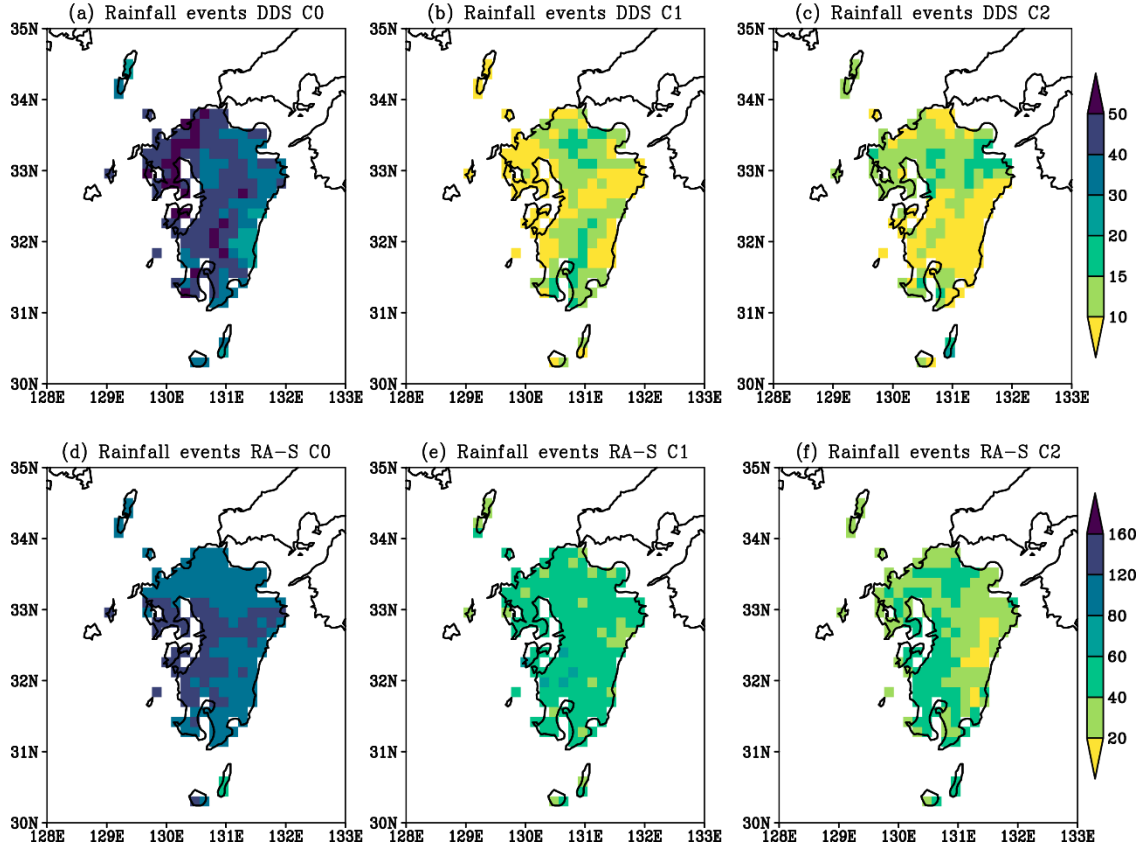


Figure 3.9. (a-c) The number of rainfall events for clusters (a) C0, (b) C1 and (c) C2 in DDS with the shading reference in the right. (d-f) Same as (a-c), but for RA-S.

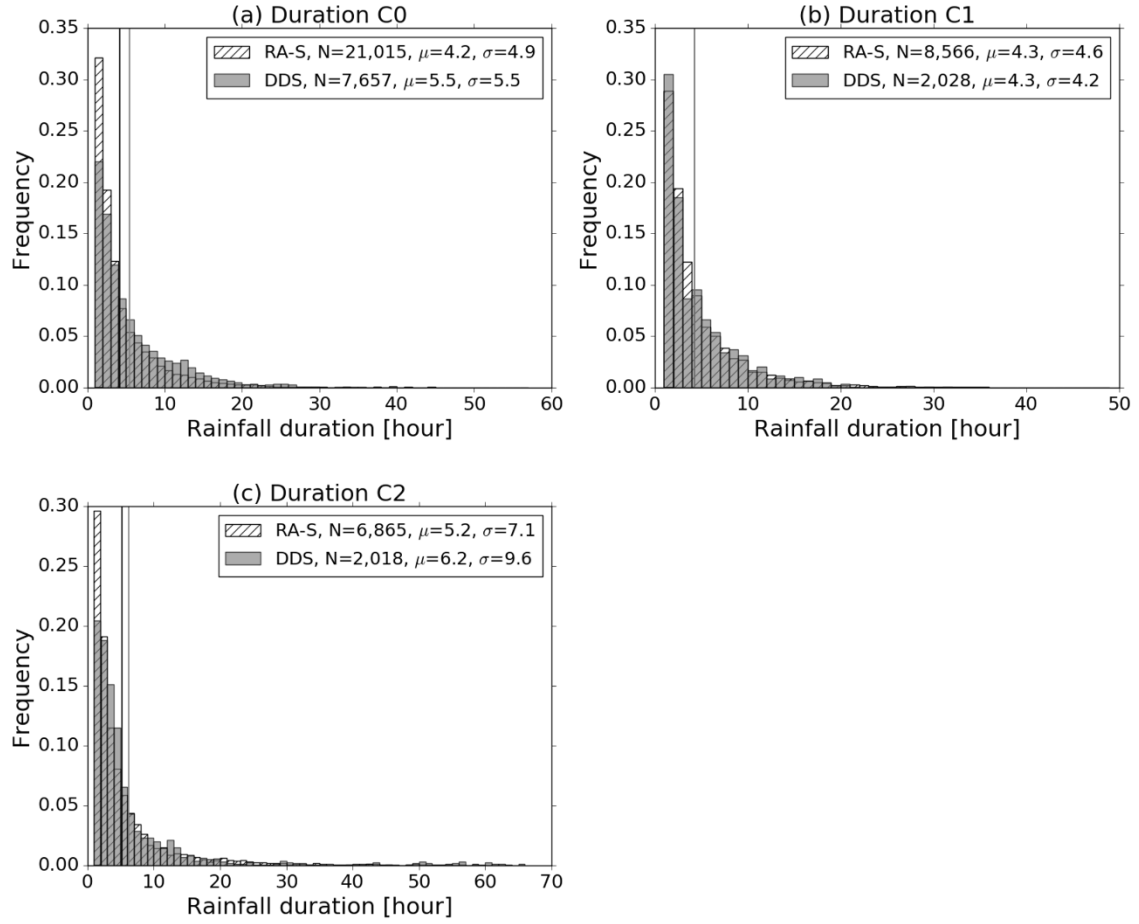


Figure 3.10. Histogram of rainfall duration in (hatched bar) RA-S and (gray bar) DDS for clusters (a) C0, (b) C1, and (c) C2. The bin width is set to 1 h, and the number, N , the mean, μ , and the standard deviation, σ , of samples are provided in the legend. The mean for RA-S and DDS is emphasized by black and gray vertical lines, respectively.

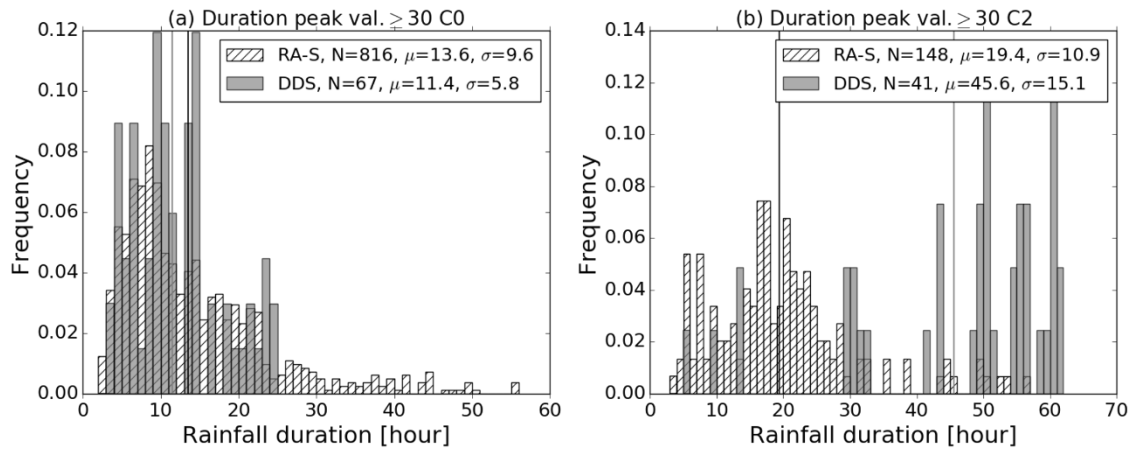


Figure 3.11. Same as Fig. 3.10, but for rainfall events of which peak value exceeds 30 mm h⁻¹.

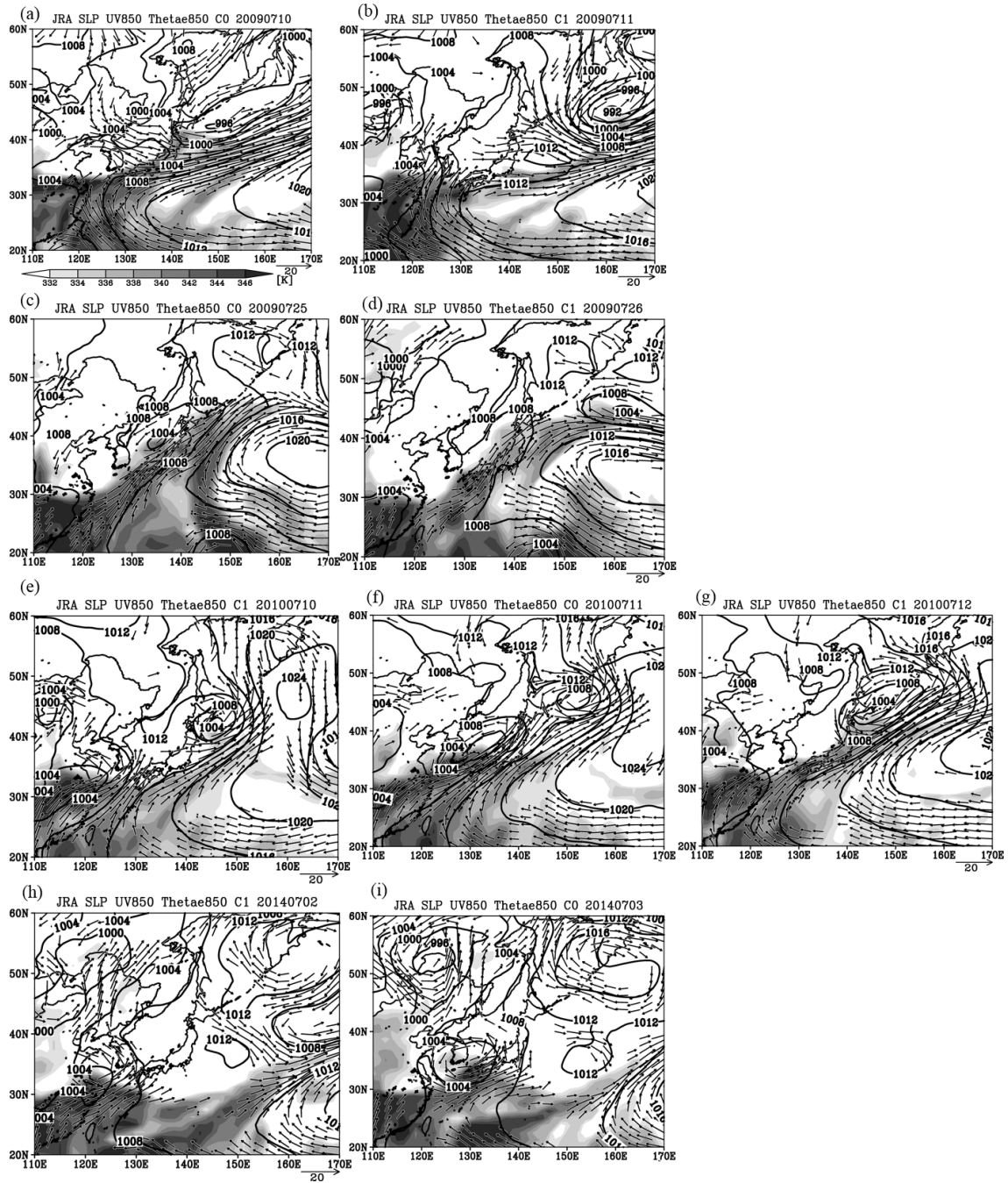


Figure 3.12. Daily mean sea-level pressure (SLP), (shading) 850-hPa equivalent potential temperature, and (vectors) 850-hPa horizontal wind during 4 transition events between cluster C0 and C1 based on JRA-55 reanalysis data. Contour interval is 4 hPa; the shading reference and the unit vector of 20 m s^{-1} are posed at the bottom of (a), and the vector $<5 \text{ m s}^{-1}$ is omitted.

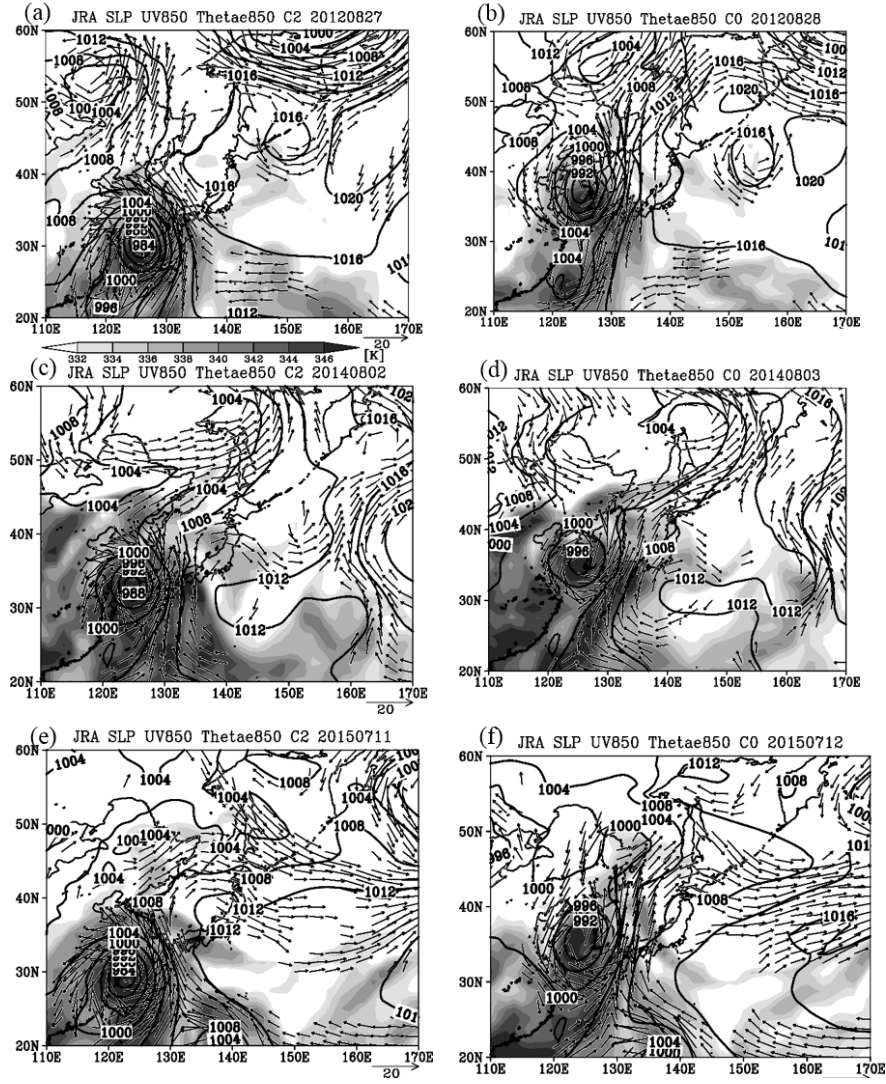


Figure 3.13. Same as Fig. 3.12, but for 3 transition events between cluster C0 and C2.

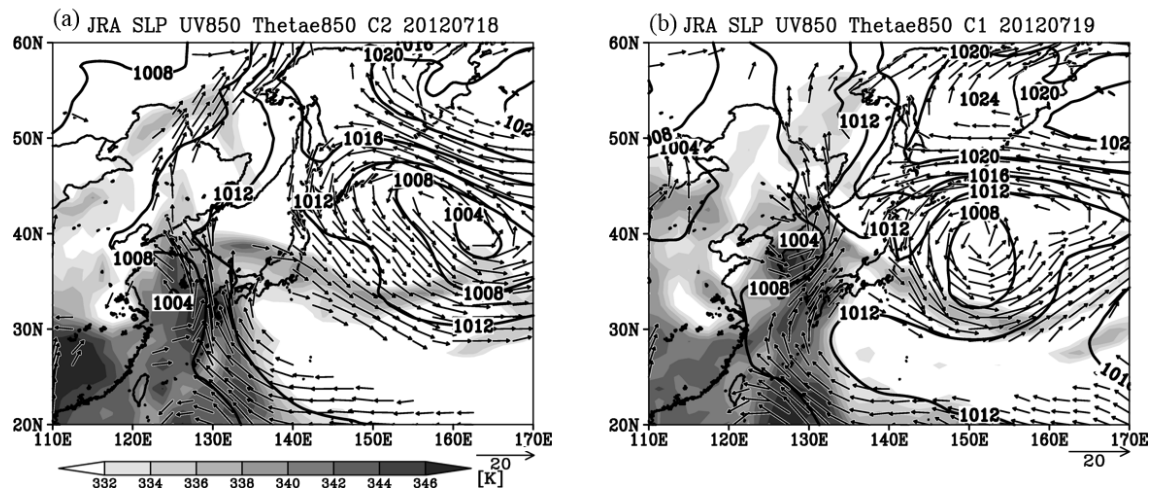


Figure 3.14. Same as Fig. 3.12, but for 1 transition event between cluster C1 and C2.

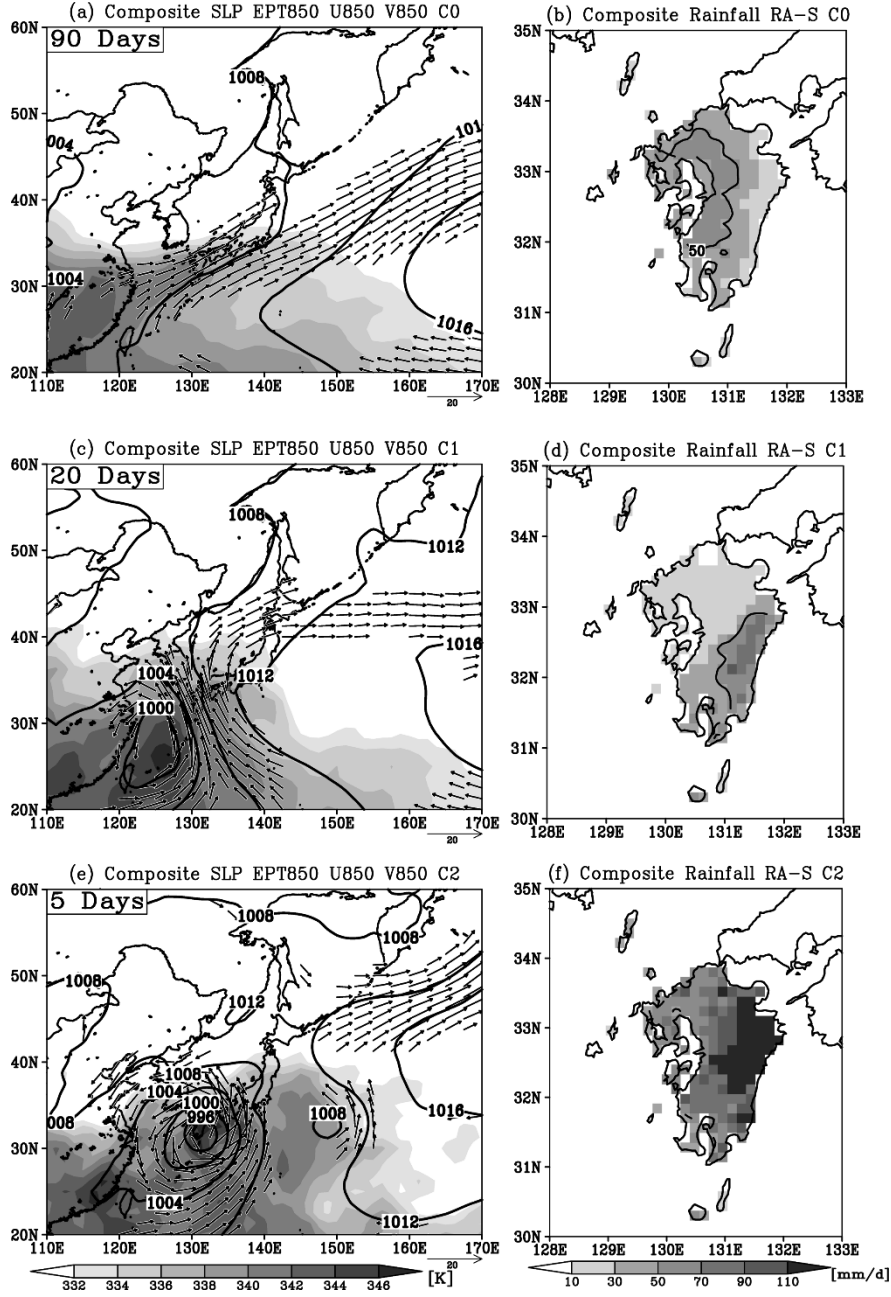


Figure 3.15. Same as Fig. 3.5, but for the node number of 9×9 for SOM.

Chapter 4. Possible hydrological effect of rainfall duration bias in dynamical downscaling

4.1 Introduction

Dynamical downscaling (DDS; Giorgi 1990), a powerful method to provide high-resolution meteorological data from the coarse-resolution data with a regional atmospheric model (RAM), generally suffers from the bias especially in precipitation owing to smoothed surface height and incomplete physical parameterizations on clouds, convection, and turbulence (Ehret et al. 2012; Wang et al. 2004). The bias in precipitation can be classified into the amount and the duration. The quantile mapping (Piani et al. 2010a,b), often used in climate change adaptation researches, can correct the probability distribution of rainfall intensity. However, it cannot correct the duration bias. Recently, Tamaki et al. (2018) suggested that the DDS tended to prolong heavy rainfall events in their target area, Kyushu, and the extent of this duration bias in the events was closely related to synoptic weather patterns such as a persistent Baiu rainband across the island and a passage of typhoon along the island.

If a hyetograph with a prolonged bias in rainfall duration input a hydrological model, the peak of surface runoff and river-flow amount would be considerably underestimated. This is because the hydrological response strongly depends on the temporal variation of the precipitation over the river catchment area, mostly attributed to mesoscale phenomena such as storm movement (Kim and Seo 2013; Sigaroodi and Chen 2016) and sporadic convective cores (Syed et al. 2003). For example, when the intense convective line moves parallel to the direction of the convective line itself (Doswell et al.

1996) under a back-building type convective system (Schumacher and Johnson 2005), an extreme flash flood very likely occurs due to the torrential rainfall in a short time. Hence the hydrological response to a hyetograph with the rainfall duration bias should be evaluated, and a caveat should be provided in a hydrological estimation based on DDS data particularly in climate change problems. However, little studies have focused on this problem, despite that the rainfall duration bias probably influences the risk evaluation on flash flood.

The purpose of this study is to evaluate a possible hydrological effect of rainfall duration bias as shown in Tamaki et al. (2018). Since a bias extent depends on synoptic weather patterns, we selected two typical heavy rainfall periods over Kyushu, Japan, in summer. One is the period during 11-15 July 2012 with a persistent Baiu rainband, characterized by the strong meridional gradient of equivalent potential temperature in the East China Sea along with the low-level jet (Fig. 4.3a). In the period, warm and humid air intrudes into Kyushu and cumulative rainfall exceeds 450 mm in western Kyushu (Figs. 4.3a,b). The other is the period during 12-16 July 2007 with a typhoon's strong cyclonic circulation over the East China Sea. In the period, the cumulative rainfall exceeds 300 mm in eastern Kyushu (Figs. 4.5a,b). These two periods are quite typical for heavy rainfall in Kyushu closely related to synoptic weather patterns [See Fig. 5 of Tamaki et al. (2018)]. To clarify the effect of rainfall duration bias to runoff, we develop a new method to artificially extend a rainfall duration time with keeping the total rainfall amount. We emphasize that the mean duration bias in heavy rainfall events related to a persistent Baiu rainband is an 8-hour extension and that related to a typhoon approach is a 16-hour extension, estimated with the DDS calculation in Tamaki et al. (2018). Sensitivity experiments are then conducted with a tank model forced by hyetographs with an 8-hour

extension and with a 16-hour extension.

4.2 Data and method

We used the site-observed hourly rainfall (mm h^{-1}) with rain gauge and the discharge ($\text{m}^3 \text{s}^{-1}$) data at eight dams over Kyushu (Fig. 4.1), with no more dams in their upstream. The dam data at Ryumon, Yabakei and Kyuragi were downloaded from Water Information System operated by Ministry of Land, Infrastructure, Transport, and Tourism (MLIT). The dam data at Shimouke, Houri, Urita, Ayaminami and Tashirobe were provided by Prefectural Land Development Department, Miyazaki Prefectural Government (a special courtesy of Mr. S. Hamada). The river catchment area including each dam ranges from 4.4 to 185.0 km^2 (Fig. 4.1). We will mainly show the results at Shimouke and Urita dams for simplicity. We also used 6-hourly JRA-55 reanalysis data (Kobayashi et al. 2015) for a synoptic field analysis, and the Radar/Rain Gauge-Analyzed Precipitation (RA; Nagata 2011) for a precipitation field analysis.

Figure 4.2 illustrates the procedure to artificially extend the rainfall duration time by using any timeseries of hourly rainfall at a site. We here define rainfall event as the period during which hourly rainfall continuously exceeds 0.1 mm h^{-1} , the minimum unit for the rain gauge. A heavy rainfall event is defined as the rainfall event with the total rainfall amount exceeding 10 mm and we used heavy rainfall events only. First, in an x -hour extension, a time stamp of rainfall data after the peak is offset by $+x/2$ hours and a time stamp before the peak is offset by $-x/2$ hours. Note that, if an event overlaps another in this extension process, the rainfall data in the overlapped period are replaced with an addition of shifted data from both events. Second, the rainfall data around the peak are compensated with a linear interpolation from peak to the shifted data. Finally,

an artificial hyetograph (R_p in Fig. 4.2) is obtained by uniformly scaling the processed data so as to keep the total rainfall amount during the event as original.

We used a four-tank model (Sugawara 1972, 1995) to estimate the runoff. The tanks are here designated as tank0, tank1, tank2, and tank3 from top to bottom. The tank0 has two runoff holes and the tank3 does not have an infiltration hole. The runoff component of tank0, ..., tank3 is physically regarded as surface/subsurface runoff, fast intermediate runoff, slow intermediate runoff, and base flow, respectively. This tank model has 4 parameters on initial water depths, 5 parameters on runoff, 4 parameters of outlet-hole heights, and 3 parameters on infiltration. They are optimized with the L-BFGS-B algorithm (Byrd et al. 1995) for each site during a heavy rainfall case (The optimized parameters in Table 4.1). We have checked that the results shown below do not change with a different parameter set realistically considered (Table 4.2 and Fig. 4.3). The tank model is forced by the observed control (CTR) hyetograph, the hyetograph with the rainfall duration extended by 8 hours (D8 hyetograph), and the hyetograph with the rainfall duration extended by 16 hours (D16 hyetograph) with the same optimized parameters in each heavy rainfall period.

4.3 Results

a. Event with the Baiu rainband and hydrology at Shimouke dam

The total rainfall during 11-15 July 2012 accompanied with the Baiu rainband across Kyushu is 530 mm at Shimouke dam (Figs. 4.4a, b). Figure 4.4c displays the observed runoff and the runoff simulated with the tank model forced by the CTR hyetograph at Shimouke dam during 11-15 July 2012. The CTR hyetograph shows three major peaks

around $t=30$, 60 and 80 and its hydrograph represents the rapid response with peaks of $250 \text{ m}^3 \text{ s}^{-1}$ around $t=30$, $500 \text{ m}^3 \text{ s}^{-1}$ around $t=60$, and $1,000 \text{ m}^3 \text{ s}^{-1}$ around $t=80$ (Fig. 4.4c). The tank model forced by this CTR hyetograph reproduced the observed hydrograph; the correlation coefficient between observation and simulation is 0.95. Similarly to the CTR hydrograph response, the water depth response has three major peaks of 150 mm around $t=30$, 200 mm around $t=60$, and 300 mm around $t=80$ (Fig. 4.4d).

The D8 hyetograph, given the typical DDS bias in Baiu rainband, represents that its sharp peaks are smoothed and the second and third rainfall event are connected by the rainfall duration bias (blue bars in Fig. 4.5c). The maximum rainfall intensity decreased by 60% compared with the CTR hyetograph around $t=80$ (Figs. 4.5b,c). A tank model forced by D8 hyetograph also shows three runoff peaks around $t=30$, 60 and 80 (Fig. 4.5a). The runoff amount at major peaks decreased by 34% compared with the CTR runoff peak around $t=80$ (Fig. 4.5a). The runoff amount just after the third major peak around $t=80-100$ increases following the rainfall duration extending in D8 hyetograph (Fig. 4.5a). Moreover, a valley between the second and third runoff peaks around $t=70$ found in CTR runoff become obscure in D8 and D16 runoffs (Fig. 4.5a). The surface/subsurface runoff contribution considerably decreases and the runoff from tank0 and tank1 less varies in time (Figs. 4.5b,c). Since, in the D8 run, the second and third heavy rainfall events of CTR hyetograph become overlapped around $t=70$ for an artificial extension (blue bars in Fig. 4.5b,c), the tank1's runoff slowly ends around $t = 65-70$ and it slowly restarts around $t=75-80$ (Figs. 4.5c). The water depth response to D8 hyetograph (Fig. 4.5d) also reduces the peak-to-peak difference of runoff around $t=50$ and 70. The timing of the water level rise is about 5h earlier in D8 run, owing to the smoothing of the

CTR hyetograph (blue bars in Figs. 4.5e,f). It is noted that the tank model results at Ryumon, Yabakei, and Kyuragi dams, where heavy rainfall events are observed accompanied with the Baiu rainband as well, are similar to the result at Shimouke dam shown here (Fig. 4.6).

b. Event with the typhoon approach and hydrology at Urita dam

The total rainfall during 12-16 July 2007 accompanied with a typhoon approaching to Kyushu is 483 mm at Urita dam (Figs. 4.7a, b). Figure 4.7c displays the observed runoff and the runoff simulated with the tank model forced by the CTR hyetograph at Urita dam during 12-16 July 2007. The CTR hyetograph shows two rainfall events with their major peaks around $t = 30$ and $t=55$ (Fig. 4.7c) and its hydrograph represents rapid response with two spike peaks with reaching $30 \text{ m}^3 \text{ s}^{-1}$ around $t=30$ and exceeding $20 \text{ m}^3 \text{ s}^{-1}$ around $t=55$ (Fig. 4.7c). The tank model forced by this CTR hyetograph sufficiently reproduced the observed hydrograph with their correlation coefficient of 0.95, though CTR hydrograph slightly underestimated the second runoff peak around $t=55$ (Fig. 4.7c). Similar to the CTR hydrograph response, the water depth in response to CTR hyetograph has two major peaks exceeding 200 mm around $t=30$ and 55 (Fig. 4.7d).

The D16 hyetograph, given the typical DDS bias in typhoon, represents that its sharp peaks are smoothed and the two rainfall events in CTR are connected by the rainfall duration bias (blue bar in Fig. 4.8b). The two major peaks of rainfall intensity in D16 hyetograph decreased by 65% around $t=30$ and 55 (blue bars in Figs. 4.8b,c), compared with the CTR hyetograph. A tank model forced by D16 hyetograph shows two major runoff peaks around $t=30$ and $t=50$ (Fig. 4.8a). The D16 runoff amount at their peaks is limited to about a half at the first peak and limited to 60% at the second peak compared

with the CTR runoff (Fig. 4.8a). The rising timing before the peaks becomes earlier and their runoff amount increases with D8 and D16 hyetographs (Fig. 4.8a), owing to the smoothing of the hyetograph (blue bars in Figs. 4.8b,c). The surface/subsurface runoff contribution considerably decreases and the runoff from tank0, and both tank0 and tank1 less vary in time (Figs. 4.8b,c). In the response of water depth, the rising timing just before the first and second peaks around $t=20$ and 50 is about 5h earlier in the D8 run and 10h earlier in the D16 run (Fig. 4.8d). This early timing of the water level rise is also accounted for the smoothing the CTR hyetograph (Figs. 4.8e,f). It is noted that the tank model results at Houri, Tashirobae, and Ayaminami dams, where heavy rainfall events are observed accompanied with the typhoon approaching as well, are similar to the result at Urita dam shown here (Fig. 4.9).

4.4 Discussion

Our results shown here provide a caveat when one applies the DDS result for studies on climate change adaptation. Nakakita and Osakada (2018) and Osakada and Nakakita (2018) showed that the frequency of occurrence of heavy rainfall related to Baiu rainband around Kyushu will significantly increase in future climate, on the basis of the DDS data with 5-km mesh and a large ensemble climate prediction dataset (d4PDF; Mizuta et al. 2017). In addition, the heavy rainfall related to Baiu rainband is spatio-temporally localized in future climate (Nakakita and Osakada 2018), and this concentration trend of heavy rainfall events is also found in northern Japan (Hoshino et al. 2018; Yamada et al. 2018). Therefore, the rainfall duration bias besides the rainfall amount bias must be considered for an accurate evaluation of runoff and flood risk in future climate.

As we referred in the introduction, however, a quantile mapping does not correct

the rainfall duration bias. Our original method for making pseudo-hyetograph might be applied the bias correction for rainfall duration. We will report this problem elsewhere.

4.5 Conclusions

We have investigated the response of runoff and water depth to the rainfall duration bias found in the dynamical downscaling over Kyushu, Japan. We selected two heavy rainfall periods related to typical synoptic pattern, Baiu rainband and typhoon. The results showed that a spike peak of runoff was suppressed by a prolonged weak rainfall as typically found in downscaling outputs. The rising timing of runoff and water depth in the tank model became earlier, in response to a smoothed hyetograph. The decrease in surface and subsurface runoff was pronounced in the heavy rainfall events accompanied with a persistent Baiu rainband, compared with the typhoon case. Our results suggest that the rainfall duration bias of DDS is a non-negligible factor for predicting river runoff and flood risk in climate change adaptation.

Tables

		shimouke-dam	ryumon-dam	yabakei-dam	kyuragi-dam	hour-dam	urita-dam	ayaminami-dam	tashioba-dam
Tank0	IS	8.78	6.15	0.01	8.96	4.53	4.91	0.01	0.01
	b	0.42	0.32	0.1	0.5	0.1	0.1	0.5	0.29
	a1	0.2	0.1	0.16	0.19	0.32	0.18	0.1	0.5
	a2	0.1	0.1	0.13	0.1	0.1	0.18	0.1	0.1
	Z1	50	50	50	50	50	45.74	50	48.21
	Z2	20	0.92	20	20	20	16.81	19.62	20
Tank1	IS	11.64	0.13	0.01	0.98	21.91	46.77	0.01	52.11
	b	0.14	0.01	0.052	0.2	0.01	0.01	0.016	0.026
	a	0.18	0.05	0.2	0.072	0.2	0.2	0.11	0.11
	Z	13.69	50	10.39	17.6	49.1	45.37	50	50
Tank2	IS	18.25	4.81	50.09	21.41	50.1	70.08	40.76	63.9
	b	0.02	0.003	0.039	0.04	0.003	0.003	0.003	0.003
	a	0.04	0.04	0.04	0.019	0.037	0.02	0.04	0.04
	Z	14.64	50	50	45.49	13.22	8.04	0	12.17
Tank3	IS	71.92	76.21	51.05	0.01	88.06	36.75	100	99.86
	a	0.003	0.003	0.003	0.0023	0.003	0.003	0.003	0.003

Table 4.1. Optimized parameters of initial water depth (IS; mm), infiltration coefficient (symbolized as b), runoff coefficient (a), and hole heights (Z1 and Z2; mm) for eight dams.

shimouke-dam												
Tank0	IS	8.784	24.049	0.010	18.986	23.157	7.657	6.303	23.438	11.344	19.904	30.531
	b	0.417	0.372	0.277	0.389	0.352	0.295	0.418	0.416	0.266	0.154	0.434
	a1	0.197	0.196	0.150	0.193	0.190	0.145	0.197	0.196	0.156	0.100	0.148
	a2	0.100	0.100	0.100	0.100	0.100	0.100	0.100	0.100	0.100	0.100	0.100
	Z1	50.000	50.000	50.000	50.000	50.000	43.754	50.000	50.000	50.000	50.000	37.675
	Z2	20.000	12.586	19.993	18.673	14.246	7.088	20.000	20.000	13.084	17.415	19.324
Tank1	IS	11.644	23.152	1.455	10.433	34.967	77.223	13.893	0.010	43.070	43.039	7.282
	b	0.140	0.083	0.050	0.109	0.045	0.041	0.141	0.142	0.026	0.018	0.099
	a	0.176	0.163	0.113	0.178	0.151	0.103	0.176	0.175	0.110	0.083	0.173
	Z	13.689	28.027	0.000	21.163	44.207	40.626	13.475	13.432	40.188	43.843	24.292
	IS	18.252	38.714	68.798	50.548	84.620	29.832	11.325	0.504	83.095	75.431	4.181
Tank2	b	0.019	0.009	0.040	0.010	0.003	0.003	0.016	0.020	0.040	0.040	0.020
	a	0.040	0.040	0.002	0.040	0.014	0.013	0.040	0.040	0.002	0.002	0.040
	Z	14.640	42.981	50.000	40.974	44.268	12.527	3.641	0.000	50.000	31.497	18.432
	IS	71.921	14.064	82.593	56.424	89.042	42.301	14.666	25.109	83.620	41.380	90.404
Tank3	a	0.003	0.001	0.003	0.001	0.001	0.001	0.002	0.003	0.003	0.003	0.003
urita-dam												
Tank0	IS	4.905	0.012	12.274	13.388	31.446	3.669	20.096	17.929	24.836	0.012	19.114
	b	0.100	0.100	0.100	0.100	0.100	0.100	0.100	0.100	0.100	0.100	0.100
	a1	0.179	0.185	0.184	0.175	0.193	0.189	0.100	0.202	0.184	0.209	0.100
	a2	0.184	0.173	0.181	0.182	0.135	0.170	0.256	0.127	0.175	0.120	0.246
	Z1	45.745	40.878	46.625	45.574	37.693	43.384	43.871	35.466	46.018	31.494	45.236
	Z2	16.808	11.757	18.082	16.485	18.509	15.432	14.394	13.463	20.000	5.211	19.114
Tank1	IS	46.772	41.809	46.762	33.970	9.772	27.340	72.897	44.890	37.058	41.196	77.809
	b	0.010	0.010	0.010	0.010	0.010	0.010	0.200	0.010	0.010	0.010	0.054
	a	0.200	0.200	0.200	0.200	0.200	0.200	0.010	0.200	0.200	0.200	0.084
	Z	45.373	29.787	42.653	24.311	16.028	23.921	50.000	50.000	49.735	32.392	10.118
Tank2	IS	70.088	5.133	40.295	7.344	26.663	93.988	93.139	50.512	47.372	11.884	28.912
	b	0.003	0.040	0.003	0.040	0.003	0.003	0.003	0.003	0.003	0.003	0.003
	a	0.021	0.040	0.040	0.040	0.040	0.011	0.021	0.040	0.027	0.040	0.040
	Z	8.046	40.257	30.607	29.265	20.749	0.000	13.932	26.138	0.000	7.263	49.750
Tank3	IS	36.755	66.390	69.956	34.961	44.144	57.550	86.064	34.971	19.332	69.750	63.239
	a	0.003	0.003	0.003	0.003	0.003	0.003	0.001	0.003	0.003	0.003	0.003

Table 4.2. Eleven sets of optimized parameters used in the sensitivity test for Shimouke and Urita dams. The maximum and minimum values for each parameter are bolded and the standard parameter set in this study is hatched.

Figures

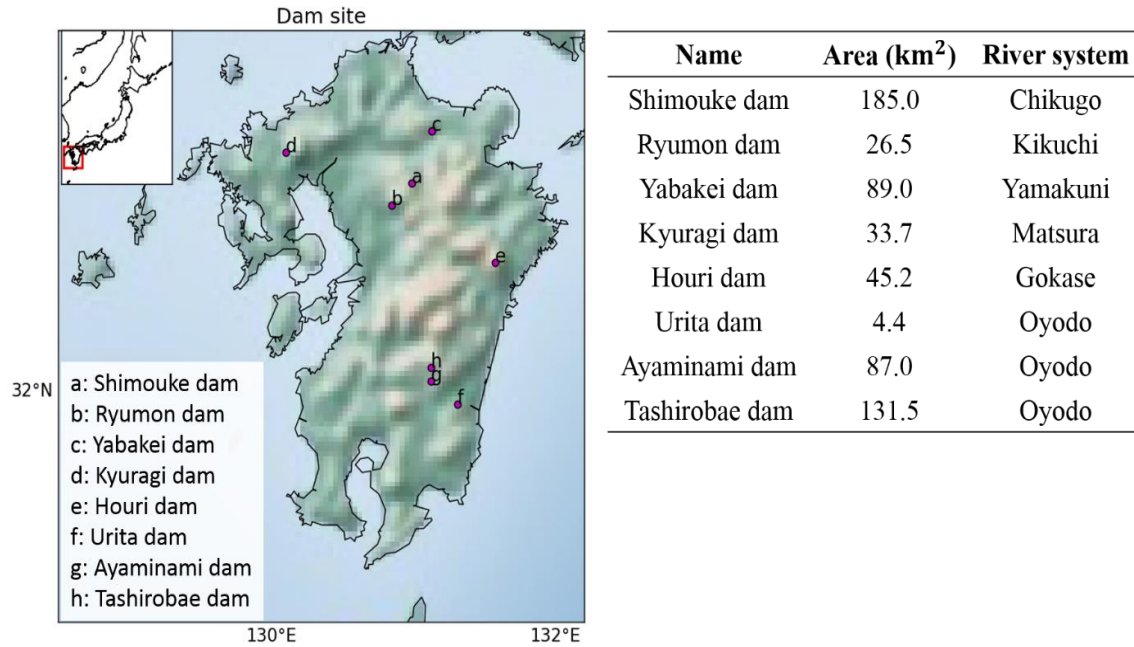


Figure 4.1. Geographic distribution of dam sites in Kyushu island, zooming a red solid box in a Japanese map shown in the inset. The catchment areas (km²) and river systems are shown in the right.

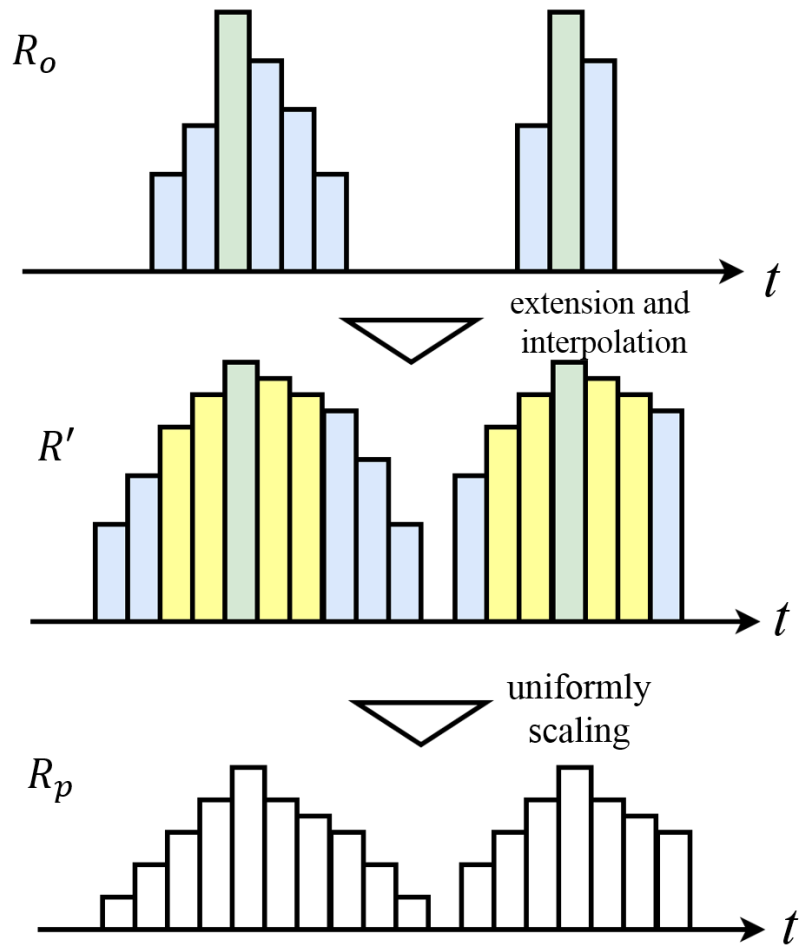


Figure 4.2. Illustration for an explanation of the procedure to artificially extend a rainfall duration by 4 hours. R_o denotes the original rainfall intensity (mm h^{-1}) at a site, and R' and R_p respectively denote the intermediate and resultant data.

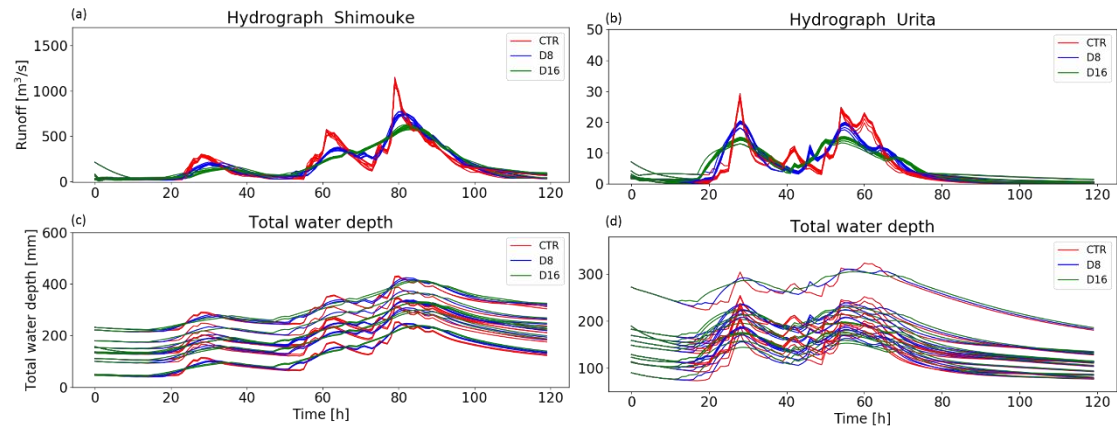


Figure 4.3. (a,b) Runoff responses ($\text{m}^3 \text{s}^{-1}$) to (red) CTR, (blue) D8, and (green) D16 hydrographs at (a) Shimouke dam during 11-15 July 2012 and (b) Urita dam during 12-16 July 2007 with eleven different parameter sets shown in Table 4.2. (c,d) Same as (a,b), but for results of water-depth responses (mm).

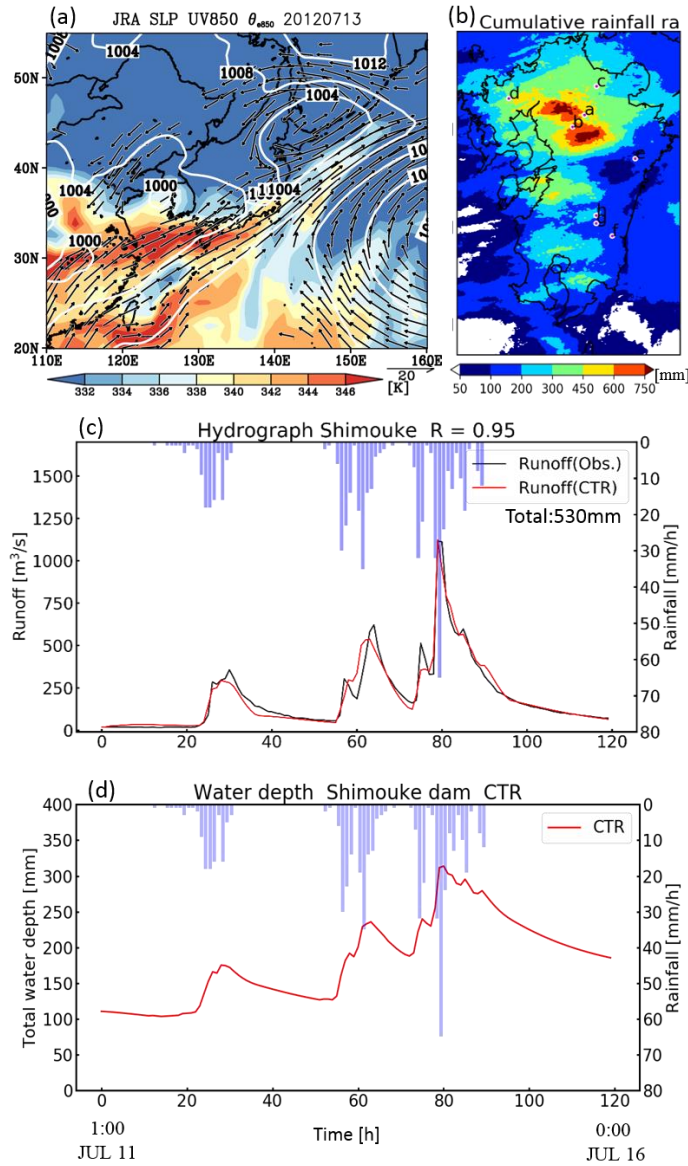


Figure 4.4. (a) Daily mean sea level pressure (SLP; contour interval is 4 hPa), 850-hPa equivalent potential temperature (shading as bottom reference), and 850-hPa horizontal wind (reference vector in bottom right corner and vector $< 5 \text{ m s}^{-1}$ omitted) during 11-15 July 2012. (b) Five-day cumulative rainfall (mm) at the dates based on Radar/AMeDAS analysis with the shading as bottom reference. (c) (Blue bar) hyetograph (mm/h) and (black line) hydrograph ($\text{m}^3 \text{s}^{-1}$) on the basis of observation at Shimouke dam. Hydrograph

of the tank model result with the CTR hyetograph is shown with red line. (d) (Blue bar) hyetograph (mm/h) and (black line) water depth ($\text{m}^3 \text{s}^{-1}$) on the basis of observation at Shimouke dam. Time series of water depth of the tank model result with the CTR hyetograph is shown with red line.

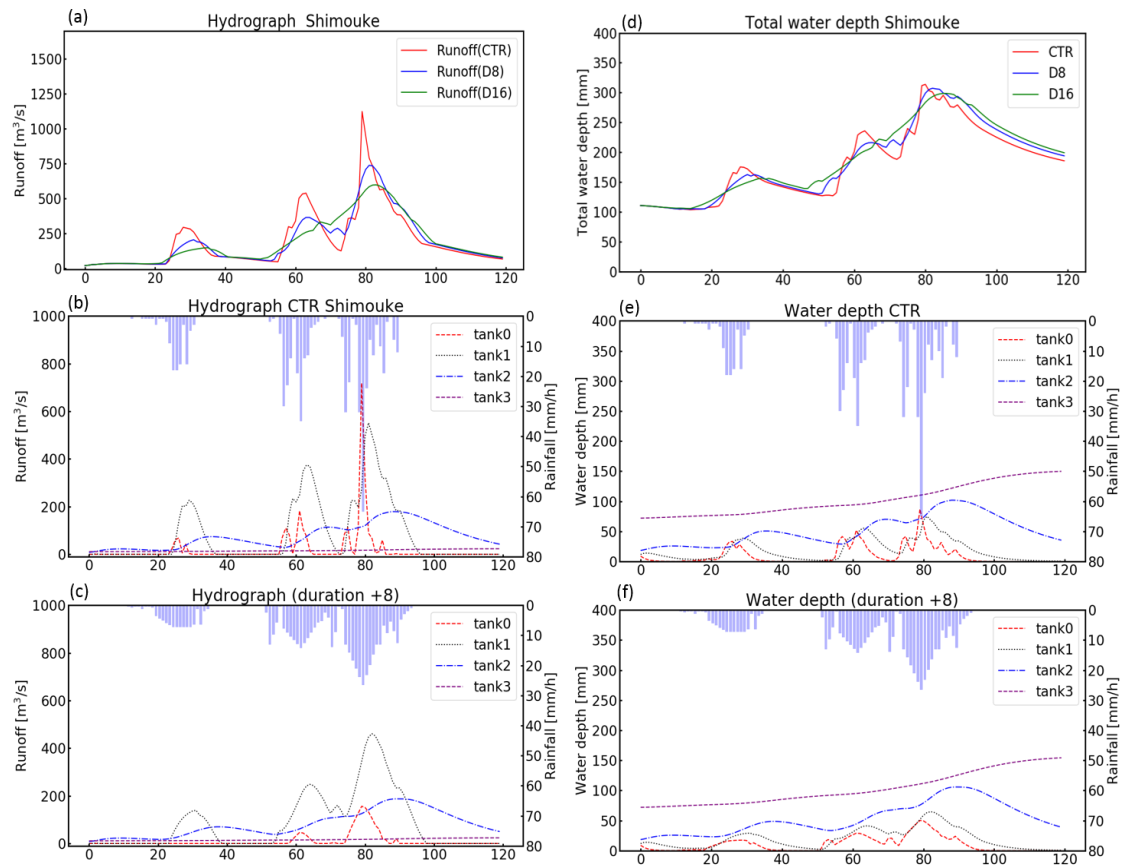


Figure 4.5. (a) Runoff response ($\text{m}^3 \text{s}^{-1}$) to (red) CTR, (blue) D8, and (green) D16 hyetographs at Shimouke dam during 11-15 July 2012. (b,c) Runoff components ($\text{m}^3 \text{s}^{-1}$) of (red) tank0, (black) tank1, (blue) tank2, and (purple) tank3 for (b) the CTR hyetograph and (c) the D16 hyetograph at Shimouke dam. (d) The water-depth response (mm) to (red) CTR (blue) D8, and (green) D16 hyetographs at Shimouke dam during 11-15 July 2012. (e) Water depth components of runoff from each tank for the CTR hyetograph at Shimouke dam. (f) Water depth components of runoff from each tank for the D8 hyetograph at Shimouke dam.

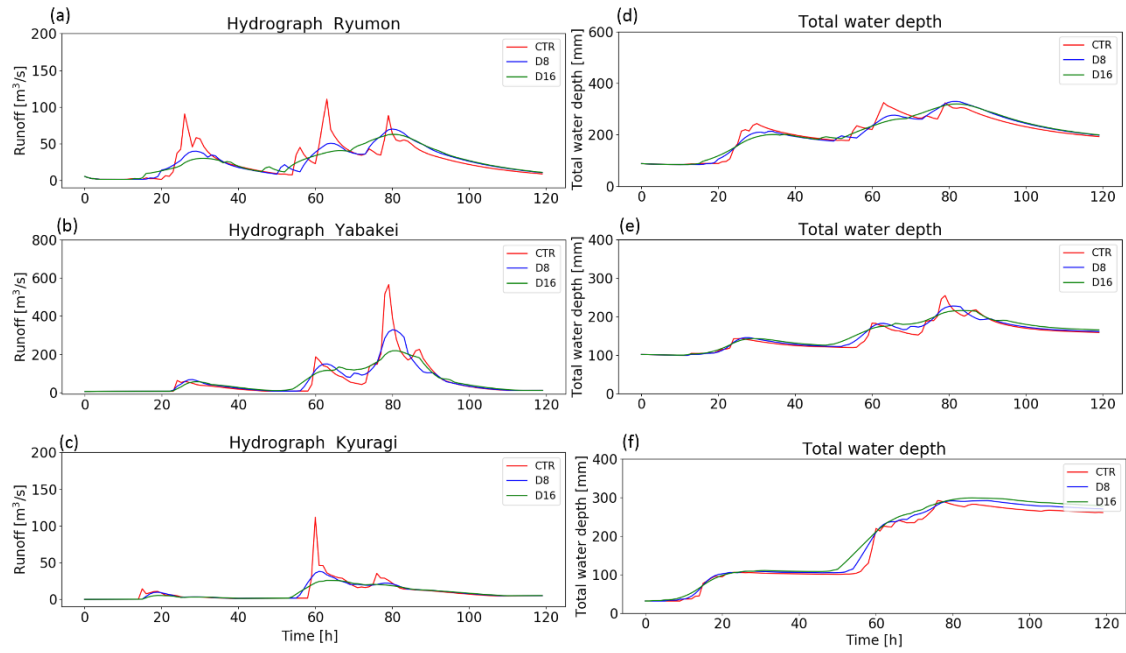


Figure 4.6. (a-c) Runoff response ($\text{m}^3 \text{s}^{-1}$) to (red) CTR, (blue) D8, and (green) D16 hyetographs at (a) Ryumon (b) Yabakei and (c) Kyuragi during 11-15 July 2012. (d-f) Same as (a-c), but for water-depth response (mm).

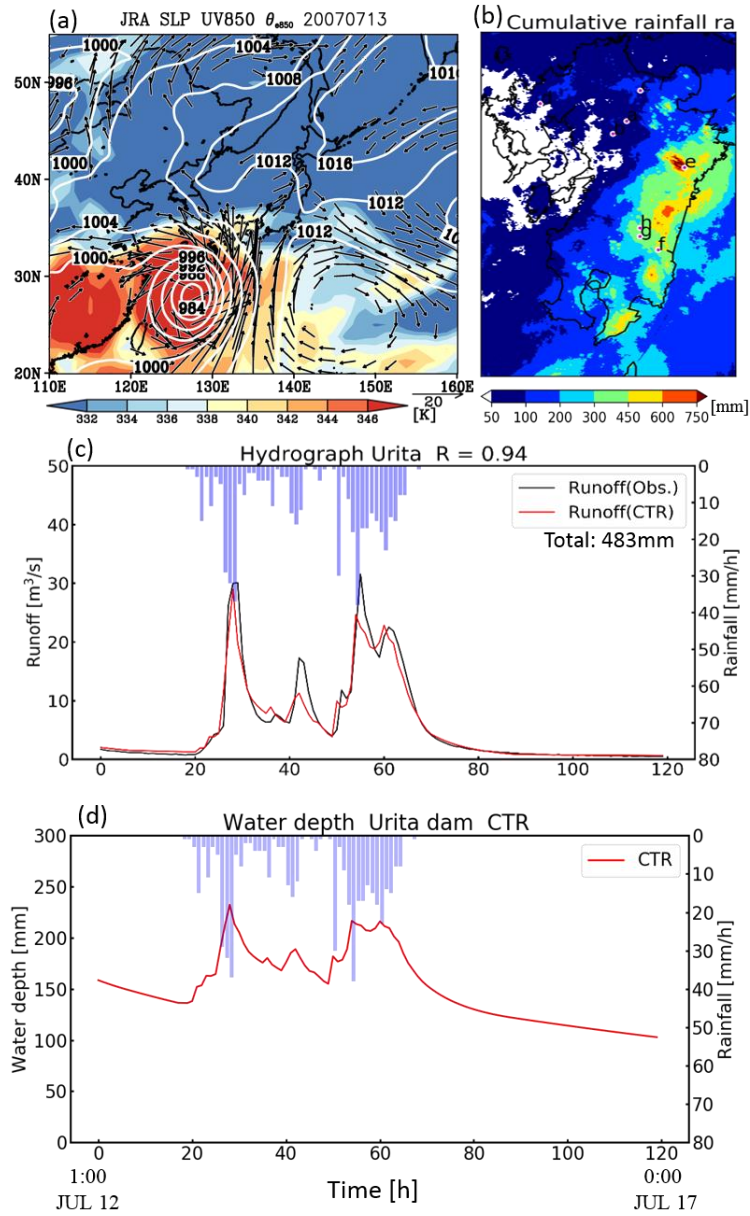


Figure 4.7. (a) Daily mean sea level pressure (SLP; contour interval is 4 hPa), 850-hPa equivalent potential temperature (shading as bottom reference), and 850-hPa horizontal wind (reference vector in bottom right corner and vector $< 5 \text{ m s}^{-1}$ omitted) during 12-16 July 2007. (b) Five-day cumulative rainfall (mm) at the dates based on Radar/AMeDAS analysis with the shading as bottom reference. (c) (Blue bar) hyetograph (mm/h) and

(black line) hydrograph ($\text{m}^3 \text{s}^{-1}$) on the basis of observation at Urita dam. Hydrograph of the tank model result with the CTR hyetograph is shown with red line. (d) (Blue bar) hyetograph (mm/h) and (black line) water depth ($\text{m}^3 \text{s}^{-1}$) on the basis of observation at Urita dam. Time series of water depth of the tank model result with the CTR hyetograph is shown with red line.

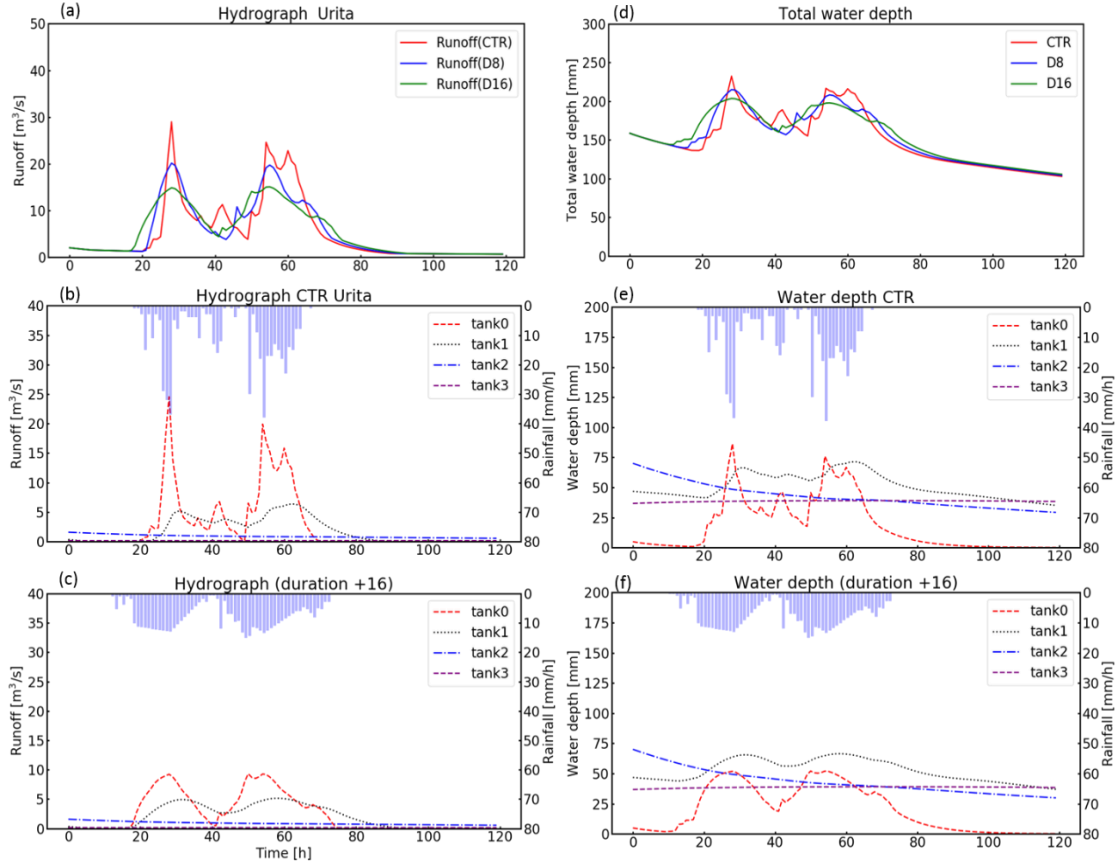


Figure 4.8. (a) Runoff response ($\text{m}^3 \text{s}^{-1}$) to (red) CTR, (blue) D8, and (green) D16 hyetographs at Urita dam during 12-16 July 2007. (b,c) Runoff components ($\text{m}^3 \text{s}^{-1}$) of (red) tank0, (black) tank1, (blue) tank2, and (purple) tank3 for (b) the CTR hyetograph and (c) the D16 hyetograph at Urita dam. (d) The water-depth response (mm) to (red) CTR (blue) D8, and (green) D16 hyetographs at Urita dam during 12-16 July 2007. (e) Water depth components of runoff from each tank for the CTR hyetograph at Urita dam. (f) Water depth components of runoff from each tank for the D8 hyetograph at Urita dam.

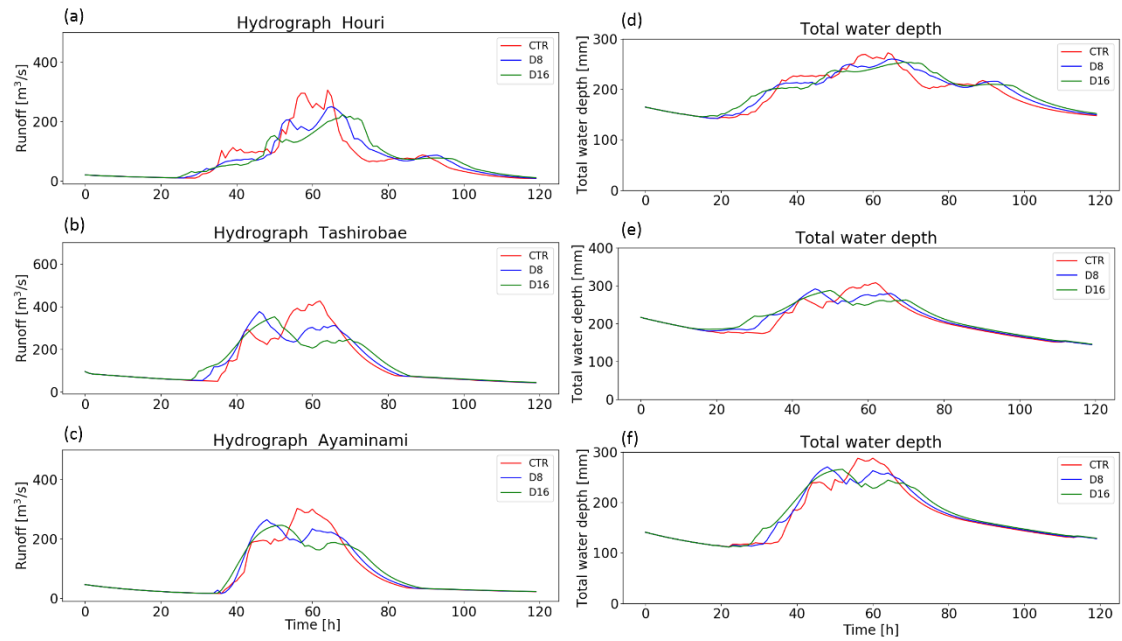


Figure 4.9. (a-c) Runoff response ($\text{m}^3 \text{s}^{-1}$) to (red) CTR, (blue) D8, and (green) D16 hyetographs at (a) Houri (b) Tashirobae and (c) Ayaminami during 12-16 July 2007. (d-f) Same as (a-c), but for water-depth response (mm).

Chapter 5. General summary

We applied the SmDS to summertime precipitation over Hokkaido. We selected the 4 years when the fluctuation of moisture flux convergence in the synoptic scale strongly influenced the fluctuation of local rainfall pattern. The SmDS estimation showed a good consistency to the full DDS in both mean and 99-percentile value of rainfall. We also established the error estimation theory both mean and 99-percentile value that the SmDS estimates. The theory showed that the estimation error of mean decrease where the synoptic field variability is strongly related to the local climate variability.

We also evaluate the rainfall duration bias in summertime in Kyushu, Japan. The results showed that the rainfall duration bias in DDS is related to its synoptic pattern. The peak runoff amount decreased and the timing of water level rise became faster as the rainfall duration bias increased. The contribution of surface/sub-surface runoff decreased as the rainfall duration bias increased and this trend is prominent in the Baiu rainband pattern.

Our research addressed the two challenges of the DDS, the huge computational cost and the evaluation of rainfall duration bias. The research of SmDS theoretically showed the scope of application of the SmDS. The theory showed that the SmDS is applicable to any regions or seasons where the synoptic field variability is strongly related to the local climate variability. The research of rainfall duration bias also pointed out the necessity of considering the rainfall duration bias and its synoptic pattern of the DDS in the climate change adaptation study on river runoff and flood.

Acknowledgments

This doctoral thesis was supervised by Prof. Masaru Inatsu. I really appreciate him for strongly supporting my research. I also thank Prof. S. Minobe, Dr. Y. N. Sasaki, Dr. H. Na, and Dr. C. H. O'Reilly, for giving us insightful comments in the laboratory seminar. We would like to thank Dr. T. J. Yamada, Dr. T. Sato and Prof. M. Nakatsugawa for giving me insightful comments during the meeting of climate change adaptation over Hokkaido. Dr. I. Takayabu, Dr. H. Kawase and Dr. Y. Imada gave many advices to my research at the seminar in the Meteorological Research Institute. I thank Dr. Y. Kitano, Dr. T. Hoshino and Dr. D. Nguyen-Le for giving me helpful advice in advancing my research. I also than Mr. S. Hamada for providing the observation data at dams in Kyushu.

Finally, I appreciate our lab's seniors, colleagues, and juniors. I also thank my parents for supporting me.

References

- Akiyama, T., 1973: The large-scale aspects of the characteristic features of the baiu front with special emphasis on the relation among the ageostrophic low-level jet stream, moist tongue, convective warming, convergence zone within baiu front and heavy rainfall. *Papers in Meteorology and Geophysics*, **24**, 157-188.
- Bartholy, J., and R. Pongrácz, 2007: Regional analysis of extreme temperature and precipitation indices for the Carpathian Basin from 1946 to 2001. *Global and Planetary Change*, **57**, 83-95.
- Berg, P., H. Feldmann, and H.-J. Panitz, 2012: Bias correction of high resolution regional climate model data. *J. Hydrol.*, **448**, 80-92.
- Bordoy, R., and P. Burlando, 2013: Bias correction of regional climate model simulations in a region of complex orography. *J. Appl. Meteor. Climatol.*, **52**, 82-101.
- Byrd, R. H., P. Lu, J. Nocedal, and C. Zhu, 1995: A limited memory algorithm for bound constrained optimization. *SIAM Journal on Scientific Computing*, **16**, 1190-1208.
- Christensen, J. H., F. Boberg, O. B. Christensen, and P. Lucas - Picher, 2008: On the need for bias correction of regional climate change projections of temperature and precipitation. *Geophys. Res. Lett.*, **35**, doi: 10.1029/2008GL035694.
- Collins, W. D., and Coauthors, 2006: The community climate system model version 3 (CCSM3). *J. Climate*, **19**, 2122-2143.
- Dai, A., 2006: Precipitation characteristics in eighteen coupled climate models. *J. Climate*, **19**, 4605-4630.
- DeGaetano, A. T., 2009: Time-dependent changes in extreme-precipitation return-period amounts in the continental United States. *J. Appl. Meteor. Climatol.*, **48**, 2086-2099.
- Donat, M., G. Leckebusch, S. Wild, and U. Ulbrich, 2011: Future changes in European

- winter storm losses and extreme wind speeds inferred from GCM and RCM multi-model simulations. *Nat. Hazards Earth Syst. Sci.*, **11**, 1351-1370.
- Donat, M. G., A. L. Lowry, L. V. Alexander, P. A. Ogorman, and N. Maher, 2016: More extreme precipitation in the world's dry and wet regions. *Nature Clim. Change*, **6**, 508-513.
- Doswell, C. A., H. E. Brooks, and R. A. Maddox, 1996: Flash flood forecasting: an ingredients-based methodology. *Weather Forecast.*, **11**, 560-581.
- Ehret, U., E. Zehe, V. Wulfmeyer, K. Warrach-Sagi, and J. Liebert, 2012: HESS opinions" Should we apply bias correction to global and regional climate model data?". *Hydrology and Earth System Sciences*, **16**, 3391-3404.
- Evans, J. P., F. Ji, G. Abramowitz, and M. Ekström, 2013: Optimally choosing small ensemble members to produce robust climate simulations. *Environ. Res. Lett.*, **8**, 044050.
- Fowler, H., S. Blenkinsop, and C. Tebaldi, 2007: Linking climate change modelling to impacts studies: recent advances in downscaling techniques for hydrological modelling. *Int. J. Climatol.*, **27**, 1547-1578.
- Frei, C., J. H. Christensen, M. Déqué, D. Jacob, R. G. Jones, and P. L. Vidale, 2003: Daily precipitation statistics in regional climate models: Evaluation and intercomparison for the European Alps. *J. Geophys. Res.*, **108**, 4124.
- Frey-Buness, F., D. Heimann, and R. Sausen, 1995: A statistical-dynamical downscaling procedure for global climate simulations. *Theor. Appl. Climatol.*, **50**, 117-131.
- Fuentes, U., and D. Heimann, 2000: An improved statistical-dynamical downscaling scheme and its application to the Alpine precipitation climatology. *Theor. Appl. Climatol.*, **65**, 119-135.

- Fujibe, F., N. Yamazaki, and K. Kobayashi, 2006: Long-term changes of heavy precipitation and dry weather in Japan (1901-2004). *J. Meteor. Soc. Japan*, **84**, 1033-1046.
- Fujibe, F., K. Saito, D. S. Wratt, and S. G. Bradley, 1999: A numerical study on the diurnal variation of low-level wind in the lee of a two-dimensional mountain. *J. Meteor. Soc. Japan*, **77**, 827-843.
- Giorgi, F., 1990: Simulation of regional climate using a limited area model nested in a general circulation model. *J. Climate*, **3**, 941-963.
- Hasumi, H., and S. Emori, Eds, 2004: K-1 coupled GCM (MIROC) description. *Center for Climate System Research, The University of Tokyo*, 34pp.
- Hay, L., and Coauthors, 2002: Use of regional climate model output for hydrologic simulations. *J. Hydrometeor.*, **3**, 571-590.
- Hoshino, T., T. Yamada J., M. Inatsu, T. Sato, H. Kawase, and S. Sugimoto, 2018: Analysis of spatiotemporal characteristics of heavy rainfall under historical and warmer climate conditions using a large-ensemble dataset(d4PDF). *J. Soc. Civ. Eng., Ser. B1 (Hydraul. Eng.)*, **74**, I_13-I_18, 2018 (in japanese).
- Iida, Y., K. i. Okamoto, T. Ushio, and R. Oki, 2006: Simulation of sampling error of average rainfall rates in space and time by five satellites using radar - AMeDAS composites. *Geophys. Res. Lett.*, **33**, L01816, doi: 01810.01029/02005GL024910.
- Ikawa, M., and K. Saito, 1991: Description of a non-hydrostatic model developed at the Forecast Research Department of the MRI. MRI Tech. Rep. 28, 238 pp.
- Imada, Y., M. Kimoto, and S. Kanae, 2012: Seasonal prediction by statistical downscaling using singular value decomposition analysis - predictability of autumn precipitation over Indochina. *J. Soc. Civ. Eng., Ser. B1 (Hydraul. Eng.)*, **68**, I_1369-I_1374 (in

- japanese).
- Inatsu., M., and Coauthors, 2014: Multi-GCM by multi-RAM experiments for dynamical downscaling focusing on summertime climate in Hokkaido. *Atmos. Sci. Lett.*, revised.
- Ines, A. V., and J. W. Hansen, 2006: Bias correction of daily GCM rainfall for crop simulation studies. *Agri. Fore. Meteor.*, **138**, 44-53.
- Jakob Themeßl, M., A. Gobiet, and A. Leuprecht, 2011: Empirical - statistical downscaling and error correction of daily precipitation from regional climate models. *Int. J. Climatol.*, **31**, 1530-1544.
- Kain, J. S., and J. M. Fritsch, 1993: Convective parameterization for mesoscale models: the Kain-Fritsch scheme. *The Representation of Cumulus Convection in Numerical Models*, K. A. Emanuel, and D. J. Raymond, Eds., American Meteorological Society, 165-170.
- Kato, T., and H. Goda, 2001: Formation and maintenance processes of a stationary band-shaped heavy rainfall observed in Niigata on 4 August 1998. *J. Meteor. Soc. Japan*, **79**, 899-924.
- Kendon, E. J., R. G. Jones, E. Kjellström, and J. M. Murphy, 2010: Using and designing GCM-RCM ensemble regional climate projections. *J. Climate*, **23**, 6485-6503.
- Kim, C., and D.-H. Kim, 2018: Effect of rainfall spatial distribution and duration on minimum spatial resolution of rainfall data for accurate surface runoff prediction. *Journal of Hydro-environment Research*, **20**, 1-8.
- Kim, D. H., and Y. Seo, 2013: Hydrodynamic analysis of storm movement effects on runoff hydrographs and loop - rating curves of a V - shaped watershed. *Water Resources Research*, **49**, 6613-6623.
- Kobayashi, S., and Coauthors, 2015: The JRA-55 reanalysis: General specifications and

- basic characteristics. *J. Meteor. Soc. Japan*, **93**, 5-48.
- Kodama, Y., 1992: Large-scale common features of subtropical precipitation zones (the baiu frontal zone, the SPCZ, and the SACZ) Part I: Characteristics of subtropical frontal zones. *J. Meteor. Soc. Japan*, **70**, 813-836.
- Kohonen, T., 1982: Self-organized formation of topologically correct feature maps. *Biological Cybernetics*, **43**, 59-69.
- Kumagai, Y., 2004a: Improvement of the land surface processes in JMANHM. *CAS/JSC WGNE Res. Activ. Atmos. Oceanic Modelling*, **34**, 0419-0420.
- , 2004b: Implementation of a non-local like PBL scheme in JMANHM. *CAS/JSC WGNE Res. Activ. Atmos. Oceanic Modelling*, **34**, 0417-0418.
- Kuno, R., and M. Inatsu, 2014: Development of sampling downscaling: a case for wintertime precipitation in Hokkaido. *Climate Dyn.*, **43**, 375-387.
- Lall, U., B. Rajagopalan, and D. G. Tarboton, 1996: A nonparametric wet/dry spell model for resampling daily precipitation. *Water resources research*, **32**, 2803-2823.
- Leander, R., and T. A. Buishand, 2007: Resampling of regional climate model output for the simulation of extreme river flows. *J. Hydrol.*, **332**, 487-496.
- Leung, L. R., Y. Qian, X. Bian, W. M. Washington, J. Han, and J. O. Roads, 2004: Mid-century ensemble regional climate change scenarios for the western United States. *Clim. Change*, **62**, 75-113.
- Li, J., A. Sharma, J. Evans, and F. Johnson, 2018: Addressing the mischaracterization of extreme rainfall in regional climate model simulations—A synoptic pattern based bias correction approach. *J. Hydrol.*, doi:<http://dx.doi.org/10.1016/j.jhydrol.2016.1004.1070>.
- Maraun, D., 2012: Nonstationarities of regional climate model biases in European

- seasonal mean temperature and precipitation sums. *Geophys. Res. Lett.*, **39**, doi:10.1029/2012GL051210.
- , 2013: Bias correction, quantile mapping, and downscaling: revisiting the inflation issue. *J. Climate*, **26**, 2137-2143.
- Maraun, D., T. Osborn, and N. Gillett, 2008: United Kingdom daily precipitation intensity: improved early data, error estimates and an update from 2000 to 2006. *Int. J. Climatol.*, **28**, 833-842.
- Maraun, D., and Coauthors, 2010: Precipitation downscaling under climate change: Recent developments to bridge the gap between dynamical models and the end user. *Reviews of Geophysics*, **48**, RG3003. doi:10.1029/2009RG000314.
- Matsumoto, S., 1972: Unbalanced low-level jet and solenoidal circulation associated with. *J. Meteor. Soc. Japan*, **50**, 194-203.
- Mizuta, R., and Coauthors, 2017: Over 5,000 years of ensemble future climate simulations by 60-km global and 20-km regional atmospheric models. *Bull. Amer. Meteor. Soc.*, **98**, 1383-1398.
- Nagata, K., 2011: Quantitative precipitation estimation and quantitative precipitation forecasting by the Japan meteorological agency. *RSMC Tokyo–Typhoon Center Technical Review*, **13**, 37-50.
- Nakakita, E., and Y. Osakada, 2018: Multiscale analysis on the future change of heavy rainfall in baiu season using regional climate models and d4PDF. *DPRI Annuals*, **No. 61 B**, 507-532 (in japanese).
- Nguyen-Le, D., T. J. Yamada, and D. Tran-Anh, 2017: Classification and forecast of heavy rainfall in northern Kyushu during Baiu season using weather pattern recognition. *Atmos. Sci. Lett.*, **18**, 324-329.

- Ninomiya, K., 1984: Characteristics of Baiu front as a predominant subtropical front in the summer northern hemisphere. *J. Meteor. Soc. Japan*, **62**, 880-894.
- Ninomiya, K., 2000: Large- and meso- α -scale characteristics of Meiyu/Baiu front associated with intense rainfalls in 1-10 July 1991. *J. Meteor. Soc. Japan*, **78**, 141-157.
- Ninomiya, K., and T. Akiyama, 1992: Multi-scale features of Baiu, the summer monsoon over Japan and the East Asia. *J. Meteor. Soc. Japan*, **70**, 467-495.
- Ninomiya, K., and Y. Shibagaki, 2007: Multi-scale features of the Meiyu-Baiu Front and associated precipitation systems. *J. Meteor. Soc. Japan*, **85B**, 103-122.
- Nishiyama, K., S. Endo, K. Jinno, C. B. Uvo, J. Olsson, and R. Berndtsson, 2007: Identification of typical synoptic patterns causing heavy rainfall in the rainy season in Japan by a Self-Organizing Map. *Atmos. Res.*, **83**, 185-200.
- Nyeko-Ogiramoi, P., P. Willems, G. Ngirane-Katashaya, and V. Ntegeka, 2012: Nonparametric statistical downscaling of precipitation from global climate models. *Climate Models. InTech Europe, University Campus STeP Ri. Slavka Krautzeka, Croatia*, 109-136.
- Ogden, F. L., and P. Y. Julien, 1993: Runoff sensitivity to temporal and spatial rainfall variability at runoff plane and small basin scales. *Water Resources Research*, **29**, 2589-2597.
- Ohba, M., S. Kadokura, D. Nohara, and Y. Toyoda, 2016: Rainfall downscaling of weekly ensemble forecasts using self-organising maps. *Tellus A*, **68**, doi:10.3402/tellusa.v3468.29293.
- Ohba, M., S. Kadokura, Y. Yoshida, D. Nohara, and Y. Toyoda, 2015: Anomalous weather patterns in relation to heavy precipitation events in Japan during the Baiu season. *J. Hydrometeor.*, **16**, 688-701.

- Oki, R., and A. Sumi, 1994: Sampling simulation of TRMM rainfall estimation using Radar AMeDAS composites. *J. Appl. Meteor.*, **33**, 1597-1608.
- Onogi, K., and Coauthors, 2007: The JRA-25 reanalysis. *J. Meteor. Soc. Japan*, **85**, 369-432.
- Osakada, Y., and E. Nakakita, 2018: Future change of occurrence frequency of baiu heavy rainfall and its linked atmospheric patterns by multiscale analysis. *Sola*, **14**, 79-85.
- Pennell, C., and T. Reichler, 2011: On the effective number of climate models. *J. Climate*, **24**, 2358-2367.
- Piani, C., J. Haerter, and E. Coppola, 2010a: Statistical bias correction for daily precipitation in regional climate models over Europe. *Theor. Appl. Climatol.*, **99**, 187-192.
- Piani, C., G. Weedon, M. Best, S. Gomes, P. Viterbo, S. Hagemann, and J. Haerter, 2010b: Statistical bias correction of global simulated daily precipitation and temperature for the application of hydrological models. *J. Hydrol.*, **395**, 199-215.
- Pierce, D. W., T. P. Barnett, B. D. Santer, and P. J. Gleckler, 2009: Selecting global climate models for regional climate change studies. *Proc. Natl. Acad. Sci. U. S. A.*, **106**, 8441-8446.
- Pinto, J. O., A. J. Monaghan, L. Delle Monache, E. Vanvyve, and D. L. Rife, 2014: Regional assessment of sampling techniques for more efficient dynamical climate downscaling. *J. Climate*, **27**, 1524-1538.
- Plummer, D. A., and Coauthors, 2006: Climate and climate change over North America as simulated by the Canadian RCM. *J. Climate*, **19**, 3112-3132.
- Prudhomme, C., N. Reynard, and S. Crooks, 2002: Downscaling of global climate models for flood frequency analysis: where are we now? *Hydro. Processes*, **16**, 1137-1150.

- Pryor, S., J. Howe, and K. Kunkel, 2009: How spatially coherent and statistically robust are temporal changes in extreme precipitation in the contiguous USA? *Int. J. Climatol.*, **29**, 31-45.
- Rajeevan, M., J. Bhate, and A. K. Jaswal, 2008: Analysis of variability and trends of extreme rainfall events over India using 104 years of gridded daily rainfall data. *Geophys. Res. Lett.*, **35**, L18707, doi:10.1029/2008GL035143.
- Roeckner, E., and Coauthors, 2003: The atmospheric general circulation model ECHAM5. *Part I: Model description. Max Planck Institute for Meteorology Rep.*, **349**, 127pp.
- Rotunno, R., J. B. Klemp, and M. L. Weisman, 1988: A theory for strong, long-lived squall lines. *J. Atmos. Sci.*, **45**, 463-485.
- Saito, K., and J.-i. Ishida, 2005: Implementation of the targeted moisture diffusion to JMA-NHM. *CAS/JSC WGNE Res. Activ. Atmos. Oceanic Modelling*, **35**, 517-518.
- Saito, K., and Coauthors, 2006: The operational JMA nonhydrostatic mesoscale model. *Mon. Wea. Rev.*, **134**, 1266-1298.
- Sampe, T., and S.-P. Xie, 2010: Large-scale dynamics of the Meiyu-Baiu rainband: environmental forcing by the westerly jet. *J. Climate*, **23**, 113-134.
- Sato, T., and F. Kimura, 2005: Impact of diabatic heating over the Tibetan Plateau on subsidence over northeast Asian arid region. *Geophys. Res. Lett.*, **32**, doi:10.1029/2004GL022089, 022005.
- Schumacher, R. S., and R. H. Johnson, 2005: Organization and Environmental Properties of Extreme-Rain-Producing Mesoscale Convective Systems. *Mon. Wea. Rev.*, **133**, 961-976.
- Shabalova, M., W. Van Deursen, and T. Buishand, 2003: Assessing future discharge of the river Rhine using regional climate model integrations and a hydrological model.

- Climate Research*, **23**, 233-246.
- Sigaroodi, S. K., and Q. Chen, 2016: Effects and consideration of storm movement in rainfall–runoff modelling at the basin scale. *Hydrology and Earth System Sciences*, **20**, 5063-5071.
- Sugawara, M., 1972: A Method for Runoff Analysis. *Kyoritsu Shuppan Press, in japanese*.
- , 1995: Tank model. *Computer models of watershed hydrology*, V.P. Singh, ed., *Water Resources Publications, Chapter 6*.
- Syed, K. H., D. C. Goodrich, D. E. Myers, and S. Sorooshian, 2003: Spatial characteristics of thunderstorm rainfall fields and their relation to runoff. *J. Hydrol.*, **271**, 1-21.
- Tamaki, Y., M. Inatsu, R. Kuno, and N. Nakano, 2016: Sampling downscaling in summertime precipitation over hokkaido. *J. Meteor. Soc. Japan*, **94A**, 17-29.
- Tamaki, Y., M. Inatsu, D. Nguyen-Le, and T. J. Yamada, 2018: Heavy rainfall duration bias in dynamical downscaling and its related synoptic patterns in summertime asian monsoon. *J. Appl. Meteor. Climatol.*, **57**, 1477-1496.
- Tomita, T., T. Yamaura, and T. Hashimoto, 2011: Interannual variability of the Baiu season near Japan evaluated from the equivalent potential temperature. *J. Meteor. Soc. Japan*, **89**, 517-537.
- Ulsch, A., and H. P. Siemon, 1990: Kohonen's self organizing feature maps for exploratory data analysis. *Proc. INNC'90, Int. Neural Network Conf.*, Kluwer, 305-308.
- von Storch, H., 1995: Inconsistencies at the interface of climate impact studies and global climate research. *Meteorol. Z.*, **4**, 72-80.
- Wang, Y. Q., L. R. Leung, J. L. McGregor, D. K. Lee, W. C. Wang, Y. H. Ding, and F. Kimura, 2004: Regional climate modeling: Progress, challenges, and prospects. *J. Meteor. Soc. Japan*, **82**, 1599-1628.

- Wilby, R., S. Charles, E. Zorita, B. Timbal, P. Whetton, and L. Mearns, 2004: Guidelines for use of climate scenarios developed from statistical downscaling methods. *Supporting material of the Intergovernmental Panel on Climate Change*, 27pp.
- Yamada, T. J., and Coauthors, 2018: The influence of climate change on flood risk in Hokkaido. *Advances in river engineering*, **24**, 391-396 (in japanese).
- Yamada., T. J., M. A. Farukh., T. Fukushima., M. Inatsu., T. Sato., Y. N. Pokhrel., and T. Oki., 2014: Extreme precipitation intensity in future climates associated with the Clausius-Clapeyron-like relationship. *Hydrol. Res. Lett.*, **8**, 108-113.
- Yatagai, A., K. Kamiguchi, O. Arakawa, A. Hamada, N. Yasutomi, and A. Kito, 2012: APHRODITE: Constructing a long-term daily gridded precipitation dataset for Asia based on a dense network of rain gauges. *Bull. Amer. Meteor. Soc.*, **93**, 1401-1415.
- Zolina, O., C. Simmer, K. Belyaev, A. Kapala, and S. Gulev, 2009: Improving estimates of heavy and extreme precipitation using daily records from European rain gauges. *J. Hydrometeor.*, **10**, 701-716.